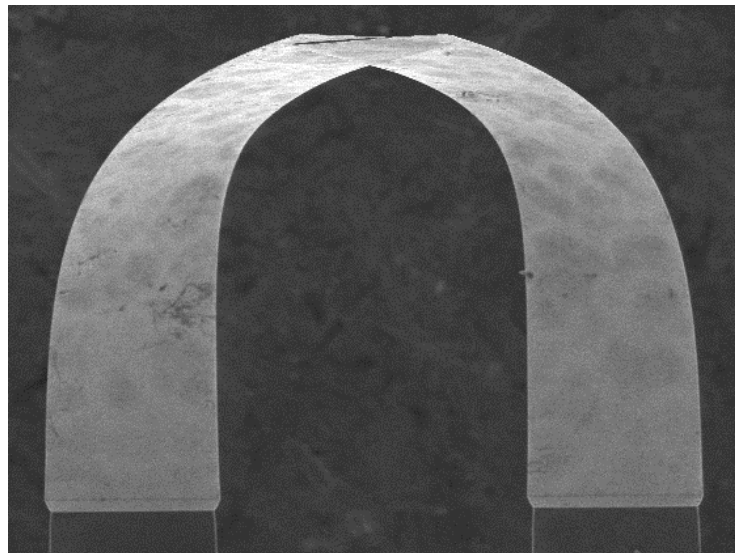UNIVERSIDAD AUTÓNOMA DE MADRID

Facultad de Ciencias
Departamento de Física Aplicada

HUMIDITY EFFECTS AT THE ORGANIC/POROUS SILICON SENSOR INTERFACE

T E S I S
D O C T O R A L

Chloé Rodriguez

UNIVERSIDAD AUTÓNOMA DE MADRID

Facultad de Ciencias
Departamento de Física Aplicada

HUMIDITY EFFECTS AT THE ORGANIC/POROUS SILICON SENSOR INTERFACE

T E S I S
D O C T O R A L

Memoria presentada por: Chloé Rodriguez
Para optar al grado de: DOCTOR

Directores: Miguel Manso Silván
Alexander Bittner

Madrid, Noviembre 2017

Humidity effects at the organic/porous silicon sensor interface

Chloé Rodriguez

PhD Thesis – Universidad Autónoma de Madrid

Cover: SEM image of two hanging porous silicon cantilevers

AGRADECIMIENTOS

Esta tesis resume tres años y medio de trabajo durante los cuales pude contar con la ayuda de mucha gente.

En primer lugar me gustaría agradecer a mi director de tesis, Miguel. Gracias por enseñarme tanto, por ayudarme y siempre pendiente. Creo que no podía haber tenido mejor jefe, ya que nadie me habría podido motivar más que él, dándome libertad y apoyo cada vez que lo necesitaba. Todavía nos queda un gofre pendiente en Grecia!

Doy también las gracias a Vicente, que para mí ha sido como un director más, estando siempre disponible para ayudarme, incluso con mis preguntas "tontas".

Gracias también a mi codirector de tesis Alex, por la ayuda aunque sea a distancia y la acogida durante mis estancias en San Sebastián.

A todos los doctorandos y compañeros del departamento con quién he pasado muy buenos momentos: Oswaldo, Rehab, Dani, Edu, Darío, Arancha, Carlos, Rosalía, Bea, Esther, Leonor. En especial a Sergio y Paola quienes han sido mis compañeros hasta el final y quienes me han ayudado mucho!

A todo el personal del SIdI por ser tan simpático y acogedor. En especial a las personas con las que más he tratado y que siempre han sido muy amables conmigo: Luís y Pascual de infrarrojo, María Jesús de RMN, y por supuesto a Isi del SEM, que siempre me ha salvado encontrándome huecos donde no los había (a cambio de meriendas).

Una mención MUY especial es para Luis, que nunca me quedará claro si realmente es técnico de laboratorio o electricista, inventor, restaurador, divulgador….Más seriamente, no tendría bastantes páginas para agradecerle toda su ayuda y enseñanza, ya que gran parte de este trabajo no habría sido posible sin él.

A ma famille et à Antonio

CONTENTS

LIST OF ACRONYMS

APTS: (3-Aminopropyl)triethoxysilane

BSE: Backscattered electrons

CP: Cross polarization

CPE: Constant phase element

DRE: Digital Rectal Examination

ESEM: Environmental scanning electron microscopy

FBS: Fetal bovine serum

FIB: Focused ion beam

FTIR: Fourier-transformed infrared

GNP: Gold nanoparticle

GPTMS: (3-Glycidyloxypropyl)trimethoxysilane

HIM: Helium ion microscopy

MAS: Magic angle spinning

NCI: National Cancer Institute

NMR: Nuclear magnetic resonance

PEG: Polyethylene glycol

PFDS: 1H,1H,2H,2H-Perfluorododecyltriethoxysilane

PSA: Prostate specific antigen

PSD: Position sensing detector

PSi: Porous silicon

PSips: Porous silicon in form of particles

PTA: Phosphotungstic acid

PV: Photovoltaic

RH: Relative humidity

SAED: Selected Area Electron Diffraction

SAM: Self-assembled monolayer

SEM: Scanning electron microscopy

Si: Silicon

STEM: Scanning transmission electron microscopy

ssNMR: Solid-state nuclear magnetic resonance

TEM: Transmission electron microscopy

TMS: Tetramethylsilane

USD: United States dollar

UV: Ultraviolet

WCA: Water contact angle

wetSTEM: Wet scanning transmission electron microscopy

XPS: X-ray photoelectron spectroscopy

ABSTRACT

In the field of biosensors for cancer detection, nanomaterials are a very promising candidate since they can enhance the performances in terms of sensitivity and detection limits. In particular, porous silicon (PSi) is a versatile matrix with large adsorption surface and tailorable surface reactivity, which allows processing a diversity of biofunctional structures. Indeed, the biomedical applications of PSi often require a surface capping with organic functionalities. In this thesis we report the visible light-induced modification of PSi by self-assembled silane monolayers for its application as biosensing platform. Versatile hydrophilic/hydrophobic surfaces were obtained and characterized by different and complementary analytical techniques. In particular, a dynamic in-situ study of wetting of functionalized PSi was conducted by obtaining adsorption isotherms from wet scanning transmission electron microscopy (wetSTEM) images.

On the other hand, we demonstrated the significance of PSi combined with gold nanoparticles (GNPs) for biosensing by developing two new dual sensing platforms providing both plasmonic and nanomechanical or electrical transduction for the specific detection of prostate specific antigen (PSA). Indeed, we transferred the fabrication of PSi to nanomechanical and impedimetric platforms and a sandwich bioassay in which the secondary antibody was tethered to GNPs was performed. In both cases, the GNPs act as an optoplasmonic label. Moreover, they are also able to contribute to the mass of the nanomechanical device and to the conductivity of the impedimetric one, magnifying therefore the sensitivity of the detection.

PRESENTACIÓN

En el campo de biosensores para la detección de cáncer, los nanomateriales son candidatos prometedores para la mejora de su funcionamiento en términos de sensibilidad y límites de detección. En particular, el silicio poroso (PSi) es una matriz versátil con alta superficie de adsorción y una reactividad de superficie adaptable, que permite el tratamiento de una diversidad de estructuras biofuncionales. En efecto, las aplicaciones biomédicas del PSi requieren a menudo un recubrimiento de superficie con grupos funcionales orgánicos. En esta tesis, presentamos la modificación inducida por luz visible del PSi con monocapas de silanos ensamblados para su aplicación como plataforma sensora. Se han obtenido Superficies versátiles hidrofílicas/hidrofóficas y se han caracterizado mediante técnicas analíticas complementarias. En particular, un estudio dinámico in-situ de la mojabilidad del PSi funcionalizado se llevó a cabo con la obtención de isotermas de adsorción a partir de imágenes de wetSTEM.

Por otro lado, demostramos la importancia del PSi combinado con nanopartículas de oro (GNPs) para el biosensado, desarrollando dos nuevas plataformas basadas en doble detección proporcionando una transducción tanto plasmónica como nanomécanica o eléctrica para la detección específica del antígeno prostático específico (PSA). En efecto, transferimos la fabricación del PSi a plataformas nanomecánicas e impedimétricas y realizamos un ensayo en sándwich en el cual el segundo anticuerpo está atado a las GNPs. En ambos casos, las GNPs actúan como una etiqueta optoplasmónica. Además, son también capaces de contribuir a la masa del dispositivo nanomecánico y a la conductividad de la plataforma impedimétrica, incrementando por lo tanto la sensibilidad de la detección.

CHAPTER 1

INTRODUCTION

1.1 BIOSENSING TECHNOLOGY TRENDS IN CANCER DIAGNOSTICS

Biosensing technology is a rapidly advancing field that benefits from the possibility to exploit the main distinguishing property of biological reactions, which is specificity, in combination with functional advanced materials. It has the potential to provide fast, accurate results and cost effectiveness and caters for modern day diagnostics, personalized medicine and point of care multi-specialty hospitals and laboratories [1]. Biosensors are basically composed of a biological element which is a biologically derived material that interacts with the analyte under study, and a sensing element which converts the recognition event into a measurable signal (optical, electrical, electrochemical, etc) [2]. There is a vast number of applications for biosensors ranging from medical monitoring for the detection of tumors, pathogens, etc to food biosecurity with the detection of food contamination for example [2]. In 2012, the global market for biosensors was estimated to 8.5 billion USD and is projected to double by 2018 due to a rise of the demand from an aging population requiring controlled self-diagnostics.

In particular, the use of biosensors in cancer detection and monitoring holds vast potential [3]. Cancer is the second largest disease throughout the world with an increasing share of deaths over the past few years [4], and can take over 200 distinct forms, including lung and prostate among the most common. For early cancer detection, accurate pretreatment staging and monitoring disease progression, the biomarkers are one of the most valuable tools. They are defined by the National Cancer Institute (NCI) in the United States as "a biological molecule found in blood, other body fluids, or tissues that is a sign of a normal or abnormal process or of

a condition or disease", and can be of various molecular origins, including DNA, RNA, or protein [5]. A partial list of tumor biomarkers is presented in **Table 1.1**.

Table 1.1 Biomarkers used for cancer detection.

TYPE OF CANCER	BIOMARKER
Breast	BRCAI, BRCA2, CA 15-3, CA 125, CA 27.29, CEA, NY-NR-I, ING-I, HER2/NEU, ER/PR
Colon	CEA, EGF, p53
Esophageal	SCC
Liver	AFP, CEA
Lung	CEA, CA 19-9, SCC, NSE, NY-ESO-I
Melanoma	Tyrosinase, NY-ESO-I
Ovarian	CA 125, HCG, p53, CEA, CA 549, CASA, CA 19-9, CA 15-3, MCA, MOV-I, TAG72
Prostate	PSA

Among the different forms of cancer, prostate cancer is the most common in males and the second leading cause of cancer related death. Prostate specific antigen (PSA) is a protein biomarker of prostate cancer produced by the cells of prostate gland [6,7]. Studies have shown that above-normal PSA levels (above approximately 4.0 ng/mL, depending on the countries and on the age of the population) correlate directly with prostate cancer. Nowadays, there are only two approved prostate cancer screening methods: Digital Rectal Examination (DRE) and PSA blood test. However, the first one is not quantitative and additional procedures are necessary if the test indicates an abnormality. Clinicians are consequently increasingly turning to blood-based diagnostic tests, which have led to important improvements in early detection and reduced prostate cancer-related mortality. Several techniques such as micro-fluidic chips [8], nanoparticle sensors [9], piezo-electric crystals [10,11], etc, can be therefore applied owing to their rapid detection and improved sensitivity compared with the standard PSA blood test.

However, many cancers, including prostate cancer, are diagnosed only after they have metastasized throughout the body. The application of nanotechnology to biosensor development allows improving the chances of detecting cancer earlier and therefore improving patient survival rates [12]. Moreover, that implies smaller sensors, which translates into better detection of cancer markers and more powerful and specific signal enhancements, reduced cost, and high throughput detection. For example, the sensitivity of the biosensors (that is, how much a change of concentration affects the transduction signal) can be increased using different types of nanoparticles, such as metallic nanoparticles [13-15], quantum dots [12] or magnetic nanoparticles [13]. In particular, owing to their unique properties, gold nanoparticles (GNPs) are often used as carriers for signal amplification in biosensors. In particular, due to their biocompatibility, their optical and electronic properties, and their remarkable versatility in biomedical applications, they are mostly used as signal transducers for biosensor applications [14,16]. The majority of GNPs-based assays exploit their ability to quench fluorescence [17] or their surface plasmon absorption (collective oscillations of the conduction electrons) [18,19]. Indeed, the GNPs exhibit localized plasmon resonances in the visible range of the electromagnetic spectrum, a very intense phenomenon since the absorption and scattering cross-sections of GNPs are many times their geometric size. Additionally, recent developments on nanomaterials-based biosensors use dual transducing elements. These allow discriminating traces of biomarkers in complex mixtures of blood proteins and to minimize painful false positives and false negatives in patient diagnosis. Consequently, dual sensors enhance also selectivity (ability of a sensor to measure a concentration of a substance in presence of other interfering substances) [20,21].

1.2 LIFETIME AND STABILITY OF BIOSENSORS

The lifetime and stability of the optoelectronic devices are a real challenge irrespective of the considered application. In particular, high humidity environment is an important degradation factor which can affect their performance and reliability by changing their optical and/or electrical properties. For example, relative humidity (RH, ratio of the partial pressure of water vapor to the equilibrium vapor pressure of water at a given temperature) is considered as an important degradation factor for photovoltaic (PV) modules by causing hydrolysis of polymeric components or corrosion of glass and metallic components such as grids. Indeed, moisture condensation in PV modules accelerates the corrosion process and leads to a reduction in the power generation produced by the cell. Air humidity is also an important factor strongly affecting the biosensor performances in dry environment. S. Kachel et al.[22] studied the impact of absorbed water on active layers commonly found in single use biosensors. This type of biosensors is commonly used by diabetics to test their blood glucose values daily. To produce test strips, an enzyme is generally immobilized in a water-borne mixture of polymers which is coated on a polymer substrate and dried. However, when the films are stored at high RH, water is absorbed and causes the degradation of the film. Humidity can also introduce noise in experimental measurements, confusing data and thus leading to unconvincing bio-detection results [23]. It constitutes therefore a limiting factor of the performance of a biosensor affecting both the physical transduction and the biological interface.

1.3 POROUS SILICON AND BIOSENSING TECHNOLOGY

Porous silicon (PSi) was discovered in 1956 by Uhlir during some experiments of electropolishing, but was just reported as a technical note [24]. Since then, PSi was ignored by scientific community until 1990 when its visible luminescence was discovered by Canham [25]. PSi can be described as a matrix of silicon quantum dots immersed in an amorphous Si/silica

network and whose internal surface area can reach until 500 m^2/cm^3 [26] (a surface area a million times greater than that of a planar surface). There are two chemical ways to produce PSi: electrochemical anodization and stain etching, apart from more recent laser based routes [27]. Through different mechanisms, chemical techniques allow dissolving Si atoms from the wafer to form porous structures with large diversity of pores [28-30]. In this work we will use both techniques, depending on the envisaged application. **Figure 1.1** shows the SEM images of the different types of PSi obtained by both techniques. Using electrochemical etching, we are able to obtain either spongy-type or columnar mesoporous silicon (pore diameter between 2 and 50 nm). The morphology of the PSi formed by vapor phase stain etching is different from that obtained by electrochemical etching. Indeed, we observe a dual macro and nano superposed structure. The nanostructure is however similar to that of the conventional anodically etched spongy-type PSi.
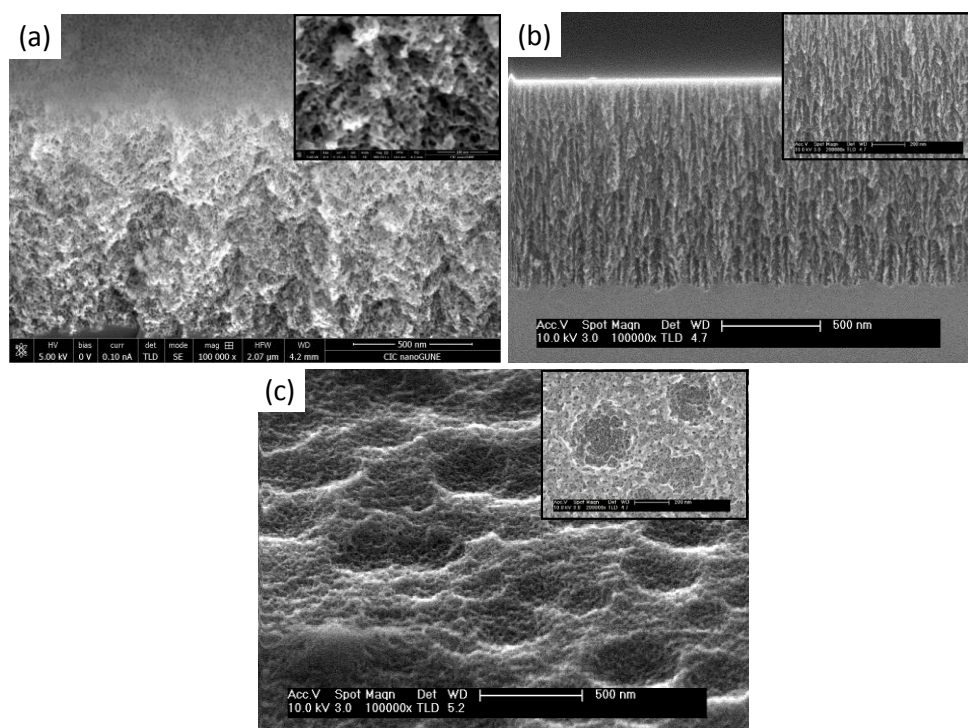

Figure 1.1 SEM images of the (a) sponge-like and (b) columnar PSi cross-section obtained by electrochemical etching of Si, and of the (c) surface of PSi (30º tilted view) obtained by vapor phase stain etching with insets of higher magnification.

19

This complex and varied morphology of PSi converts it into a very promising material for the development of several applications in different scientific fields, from optoelectronics to biomedicine [30]. In particular, PSi is an excellent biomaterial owing to its biocompatibility, biodegradability and bioresorbability and finds a lot of applications in biosensors. It has a controlled surface reactivity, which opens new opportunities to tune the material [30], and its large surface to volume ratio allows increasing the number of biomolecules able to bind the surface and consequently enhances its sensitivity as biosensor. Depending on the specific envisaged application, the pore structure and porosity of PSi can be adapted [30]. Although both micro- (pore diameter less than 2 nm) and mesopores can be used to achieve high porosity, mesoporous structures are generally preferred because they exhibit better mechanical stability in comparison to the microporous ones [31]. Furthermore, the pores present an open structure and are accessible to biomolecules such as enzymes, which enables the biocatalytic functionalization of PSi [32].

1.3.1   COMPOSITE PSi-Si NANOMECHANICAL BIOSENSORS

Among the different types of biosensors, the mechanical ones are of growing interest. In particular, nanomechanical devices allow a label-free and simultaneous detection of several targets and provide high sensitivity and fast responses, which is necessary for the observation of biological processes. Moreover, the nanoscale of the mechanical sensors guarantees a low reagent and sample consumption and an excellent mass resolution [33]. Displacements in nanomechanical biosensors range from angstroms to hundreds of nanometers. To measure these displacements, the optical lever is the most widely used method owing to its simplicity, extreme sensitivity and its capability to be easily implemented in vacuum, air and liquids [34].

Among the nanomechanical biosensing systems, microcantilevers are the simplest and most widely used. The resulting mechanical response to their interaction with a biological analyte is

either a deformation or a resonance frequency shift. Indeed, they can be used in two main operation modes: the static mode, in which changes in the cantilever bending are detected (as induced by compressive or tensile stress), and the dynamic mode in which resonance frequency shifting occurs as a consequence to the added mass of the analyte on the sensor surface (**Figure 1.2**) [34]. In many cases the changes of resonance frequency can also be influenced by changes in the mechanical stiffness of the adsorbate-beam system.
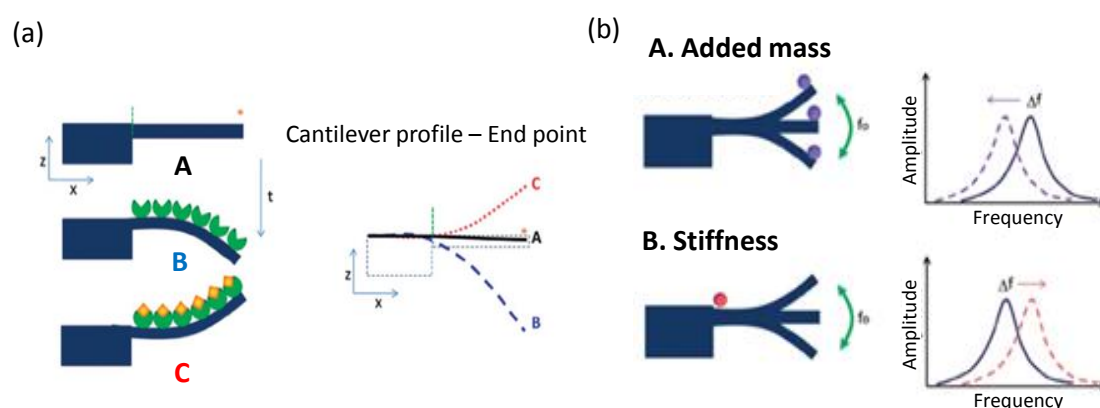
Figure 1.2 Main operation modes of nanomechanical biosensors: (a) static mode in equilibrium (A) and under tensile (B) or compressive (C) stress, and (b) dynamic mode frequency shift induced by mass (A) and stiffness (B) variations. Reprinted with permission from [34].

The miniaturization of cantilevers, however, leads to the decrease of the sensing area. Owing to its huge fractal surface area within a small volume, PSi constitutes an excellent candidate to increase the sensing area. The formation of PSi layer on the surface of crystalline Si cantilevers has been shown to enhance the sensitivity in biosensing applications [35-38]. The processed PSi introduces negligible bending of the cantilevers and provides an excellent biocompatible material for immobilization of a wide variety of chemical and biological materials, resulting in enhanced sensitivity. By forming PSi on crystalline Si cantilevers, the advantages of both forms of Si are combined. The crystalline Si provides excellent elastic and

mechanical properties while PSi provides large adsorption surfaces and constitutes an excellent biofunctional material [35].

1.3.2 PSi IMPEDANCE BIOSENSORS

Impedance spectroscopy based detection is gaining significant interest as a label-free technique for sensitive measurements of different targets thanks to its high sensitivity and selectivity, miniaturization potential, simplicity and affordability [39-41]. A typical impedance biosensor comprises a sensing element consisting of a conducting surface onto which capture molecules are immobilized to induce the specific binding and recognition of the target biomolecule. The electrical impedance at the interface is then measured in alternating current steady-state conditions over a range of frequencies of interest. In particular, impedance biosensors using interdigitated electrodes have been extensively employed for label free and rapid detection of a wide variety of biomolecules [42-44]. However, they suffer from limited sensitivity and risk of loss of specificity. To improve the performances, PSi is a good material to replace the conventional substrates in novel chemical sensors and biosensors [45] owing to its high specific surface area together with the control of the physico-chemical behavior of its nanostructured surface. In particular, the electrical behavior of PSi is in general extremely sensitive to its surface properties and composition, and is highly sensitive to the presence or absence of biomolecules on its surface [46].

1.3.3 HUMIDITY EFFECTS ON THE PROPERTIES OF PSi

Humidity adsorption measurements are of primary importance to yield information about the wetting and the hydrophobic or hydrophilic properties of porous materials. Water vapor in porous media, and, in particular, condensation/evaporation from PSi in response to variations in ambient conditions is of interest in many technological applications such as drying, catalytic

reactions, and also in optoelectronics and biomedicine [47]. It is of main importance from the point of view of the protection of PSi based devices. Indeed, high environmental humidity can affect their performance and reliability by changing their optical and/or electrical properties as briefly reviewed in **Table 1.2**. The conductance and capacity increase with the RH while the reflectivity and photoluminescence decrease with the RH.

Table 1.2 Effect of relative humidity (RH) on the basic electrical and optical properties of PSi.

PSi PROPERTIES	TECHNIQUE	BEHAVIOR WITH INCREASING RH	REFERENCE
Electrical properties	Conductance	Increases	Mares et al. [48]
	Impedance	Stable	Kovacs et al. [49]
	Capacity	Increases	Rittersma et al. [50]
Optical properties	Reflectivity	Decreases	Xifré Pérez et al. [51]
	Photoluminescence	Decreases	Oswald et al. Mandal et al. [52,53]

1.4 SELF-ASSEMBLED MONOLAYERS

Many biomedical applications of PSi require the surface of the material to be modified to be able to interface with the biological system in a controlled way [54]. Indeed, surface modification of PSi is of great importance since the modification not only provides stability to the material in biological environment but can also be used to impart an application-dependent functionality. A large number of strategies for modifying PSi, including polymers, oxidation, and a variety of different self-assembled (mono)layer (SAMs) systems have been used [55-58]. In particular, surface modification with activated or self-assembled silanes layers allows providing specific functionalities and molecular selectivity [59]. In general, self-assembling

molecules can be divided into three key components: the head group, which exhibits some selective interaction with the surface (it works for specific substrates or families of substrates), the linker chains (in general an alkyl or derivatized alkyl group), which are brought close to each other through van der Waals interaction, and finally the terminal functional groups. SAMs are formed as a result of spontaneous self-organization of functionalized, long-chain organic molecules onto the surfaces of substrates into stable and well-defined structures with a molecular-level control (**Figure 1.3**) [60].
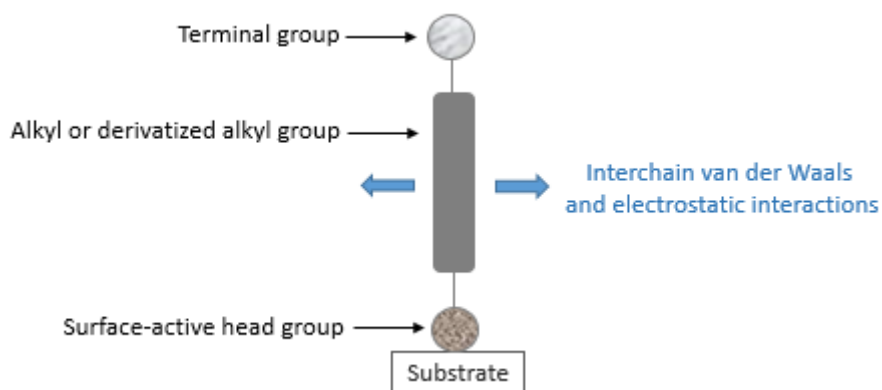
Figure 1.3 Schematic of a typical monomer for the production of self-assembled monolayer on a surface and the associated interactions.

Surface modification with SAMs not only provides specific functionalities and biomolecular selectivity but also allows controlling the degradation processes induced by the high humidity environments. Indeed, organosilanes have attracted significant attention thanks to their capability to tailor surface properties, wetting or biocompatibility in homogeneous or micro-patterned areas [61]. By capping with different terminal groups, the surface can be engineered to attract or repel water. The success of SAM-based sensor applications depends on the stability of the underlying SAM as a function of aging and on environmental conditions such as humidity and temperature. Relevantly, the wetting characteristics of organic surfaces are relevant to a wide range of biochemical, environmental, and technological phenomena such

as molecular recognition and binding processes in biology [62]. In this field for example, the wetting characteristics of SAMs are the main factor affecting the protein adsorption on a biomaterial, which in turn is directly responsible for biocompatibility, biofouling, and all other interface-dependent properties. This is why, understanding the wetting ability of biomaterial surfaces at the microscopic scale is of primary importance to design new biomaterials with a better ability to support the attachment, growth, and function of biomolecules and/or cells [63].

1.5 THESIS MOTIVATION AND OBJECTIVES

This Thesis aims at using the high surface sensitivity of PSi as biosensing platform upon modification by silane layers that should control locally hydrophilic/hydrophobic interactions. Amongst materials being used as biosensors, we focused on PSi because it has gained popularity in recent years and became a promising candidate for their fabrication. However, the lifetime and stability of the PSi based devices are a real challenge. This is why we were led to study the effects of humidity at the interface of PSi and try to tailor its wetting behavior. This approach is not only important from the point of view of device protection but also from the point of view of the development of the biosensors since the wetting characteristics of the surface are the main factor affecting the protein adsorption on a biomaterial.

Therefore, the first objective of this thesis was to functionalize PSi with different organosilanes attaining versatile hydrophilic/hydrophobic surfaces and to apply surface and interface characterization techniques to describe the induced modifications. In particular, a study of the RH on the modified PSi was planned in the research center NANOGUNE in San Sebastián (Spain) using wet scanning transmission electron microscopy (wetSTEM). On the other hand, the second objective was to apply surface immobilization techniques to biologically activate the surface for detection of specific proteomic species. This process of formation of biorecognition interfaces aimed in particular at describing new dual sensing platforms based on

PSi and GNPs. Indeed, we aim at developing two different PSi-based biosensors for the detection of PSA by transferring the fabrication of PSi to nanomechanical and impedimetric platforms and through a sandwich bioassay in which the secondary antibody is tethered to GNPs.

On the one hand, we propose the study of composite PSi-Si cantilevers providing both plasmonic and nanomechanical transduction. Additionally, we propose the design of PSi-based impedimetric devices with Ni/Cr interdigitated electrodes. In the former case, the GNP introduces a mass detection enhancement, while it behaves as an electrical label on the latter case. In both cases, the contribution of the GNPs to the dual detection scheme stems from their optoplasmonic behavior. For this part of the work a collaboration was set out in the framework of the project THINFACE with the industrial partner MECWINS.

CHAPTER 2

EXPERIMENTAL METHODS

2.1 SYNTHESIS TECHNIQUES

2.1.1   PSi FORMATION

Electrochemical etching

PSi is most often formed by electrochemical etching of Si in a HF-based electrolyte [26]. In this technique, the Si wafer acts as the anode and an appropriately shaped platinum (Pt) wire is used as cathode and counter electrode. The system is connected to a power supply, which regulates the current/voltage on the Si crystal. Since HF is extremely corrosive, Teflon beakers are commonly used as reactors. A scheme of the electrochemical cell used in this thesis is shown in **Figure 2.1**.
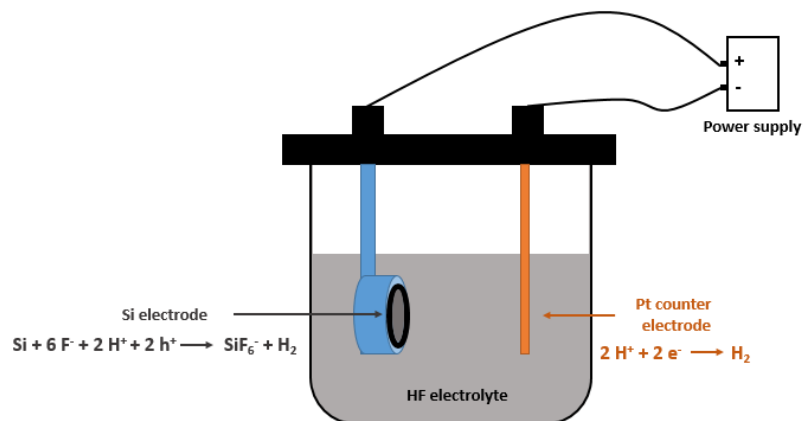

Figure 2.1 Schematic of a two electrodes electrochemical cell used in the processing of PSi.

The Si sample is placed on a stainless steel base and sealed through an O-ring. In this set-up, only the front side of the Si sample is exposed to the electrolyte. Since the Si surface is hydrophobic, the electrolyte increases its wettability and removes any bubbles formed during etching.

In an electrochemical reaction, the cathode supplies electrons to the solution while the anode removes them from the solution. In the case of PSi formation, the reaction occurring at the Si electrode is the oxidation of the Si itself while at the Pt electrode protons are reduced to hydrogen gas, as shown in **Figure 2.1** [64]. The formation of PSi involves reactions of Si–Si, Si–H, Si–O, and Si–F bonds at the surface of the Si crystal. During the electrochemical etching, the exposed Si surface becomes H-terminated. **Figure 2.2** shows the sequence of reactions involving electron and hole (h^+) exchange and the hydride and fluoride coverage taking place at the surface during Si electrode dissolution in HF [65]. The dissolution reaction begins at the defects of the Si surface. This latter, saturated by hydrogen, is in inert state as long as no holes are present. However, if a hole reaches the surface, a F^- ion attacks a Si-H bond and the Si-H bond is replaced by a Si-F bond (1). Due to the polarizing influence of the bonded F, another F^- ion can attack another Si-H bond and form Si-F bond with the generation of a H_2 molecule and injection of an electron into the substrate (2). The inner Si-Si bonds are weakened and are consequently attacked by HF, H or O (3). The resultant product H_2SiF_6 decomposes into SiF_6^{2-} and H^+, which can dissolve in the electrolyte (4). When a Si atom is removed by this reaction, an atomic size dip is formed. This changes the electric field distribution in such a way that the holes are preferentially collected at the pore tips and dissolution further takes place at the pore tips.
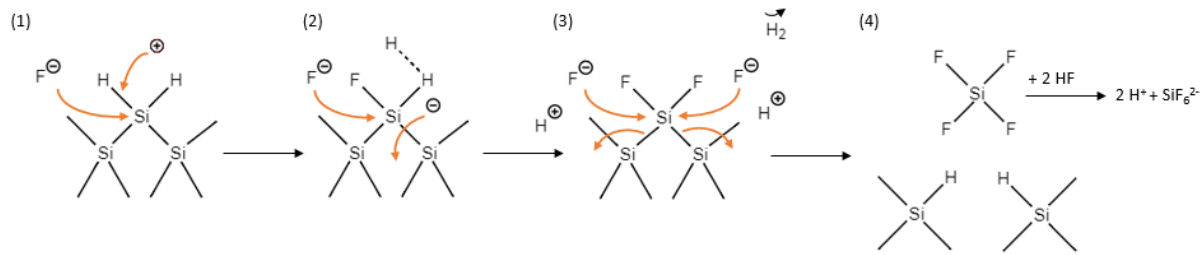
Figure 2.2 Sequence of electrochemical reactions (1)-(4) taking place during PSi formation.

The electrochemical process is mainly controlled by the current/voltage, by the solution composition and the properties of the Si wafer (type, resistivity, dopant), as illustrated in **Table 2.1**. Indeed, all the properties of PSi, such as porosity, thickness, pore diameter and microstructure, depend on the Si wafer properties and on the anodization conditions [66].

Table 2.1 Main effects of anodization parameters on PSi formation. Adapted from [64].

AN INCREASE OF…YIELDS	POROSITY	ETCHING RATE	CRITICAL CURRENT
HF concentration	Decreasing	Decreasing	Decreasing
Current density	Increasing	Increasing	-
Anodization time	Increasing	Almost constant	-
Temperature	-	-	Increasing
Wafer doping (p-type)	Decreasing	Increasing	Increasing
Wafer doping (n-type)	Increasing	Increasing	-

Vapor phase stain etching

Electrochemical etching is the most widespread method to generate PSi because it allows an excellent control of all the properties of the porous layer (porosity, thickness, pore diameter, etc). However, in the case of microcantilevers, due to their small size, fragility and the absence of metallic contact, the electrochemical route is hard to carry out. Stain etching does not require any technical equipment, such as current source, and constitutes a good

alternative to form thin PSi films [29]. Moreover, it provides good reproducibility and homogeneity. As for the electrochemical etching, the thickness and the micro-crystal size can be adjusted varying the experimental conditions of the process (type and concentration of the acids, temperature and exposure time). This method can be operated in vapor or liquid phase. In particular, the vapor phase stain etching consists of exposing Si substrates to acid vapors issued in general from a mixture of HNO_3 (65%) and HF (40%), as illustrated in **Figure 2.3**. To start the process and initiate the formation of brown NO_x vapors, a piece of sacrificial Si is added to the solution and the chip, which is stuck on a Teflon lid is exposed to the vapors once they reach a steady-state.
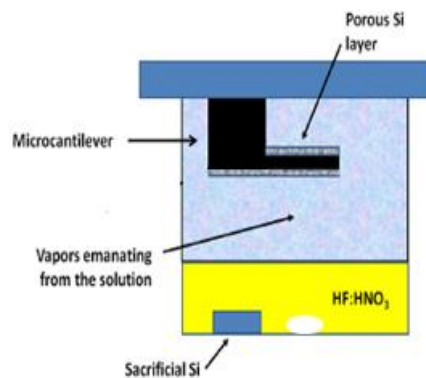
Figure 2.3 Vapor phase stain-etching formation of PSi on Si microcantilevers.

The main reaction of the acid mixture with sacrificial Si in the solution is the following:

$$Si + 4\ HNO_3 + 4\ HF \longrightarrow SiF_4 + 4\ NO_2 + 4\ H_2O \quad \textbf{Eq. 2.1}$$

Since the boiling temperature of nitrogen dioxide (NO_2) is very low (21°C), it evaporates intensively after the addition of the sacrificial Si, and is easily identified due to its brown color. The vapors serve as a carrier gas for other solution components and provide etching of the Si sample with the reaction mixture for the formation of the porous layer.

30

2.1.2 SAMs FORMATION

Silanization and hydrosilylation are the two most popular strategies to modify PSi with monolayers (very often submonolayers) and allow further incorporation of multiple components into an interface. In particular, assembly has been previously proposed by visible light activated hydrosilylation (reaction between hydrogen-terminated silicon and molecules containing double bonds) [67,68]. However, organosilane SAMs are preferred due to their fast and easy preparation, stability, and applicability to a wide range of substrates. Moreover, surface modification with organosilane assemblies allows diversifying the chemical functionalities and provides biomolecular selectivity [59]. An organosilane is a silane containing at least one carbon-silicon bond (Si-C) and can be represented as **R-Si-X$_3$**, where **R** is a non-hydrolyzable organic moiety and **X** a hydrolyzable group such as an alkoxygroup (methoxy, ethoxy, etc). The organosilane monolayers on PSi are formed by placing the PSi substrate in a solution of the corresponding molecules. The adhesion of functional molecules to the surface and the formation of SAMs are spontaneous processes due to the favorable interaction of the surfactant molecules with themselves and the surface. Relevantly, the assembly of organosilanes on PSi surfaces requires a previous oxidation that has been traditionally promoted by thermal process or peroxidation [69]. Recent reports have demonstrated that oxidation of PSi can be catalyzed upon exposure to visible light, leading to an increase of free electrons density at the PSi interface, which can, for instance, efficiently reduce metal ions [70]. A covalent bond is formed upon reaction between the silane head group Si-X$_3$ and surface hydroxyl groups. Further, crosslinking between silane molecules through lateral Si-O-Si bonds between head groups also occurs in this system. The resulting covalent linkages between the SAMs and the surface and the crosslinks between the molecules yield silane-based SAMs [71]. Among the different self-assembling molecules, aminosilanes such as (3-aminopropyl)triethoxysilane (APTS) stand as the most prominent ones for surface

biofunctionalization [72]. On the other hand, epoxy groups in (3-Glycidyloxypropyl)trimethoxysilane (GPTMS) are able to react with different nucleophilic groups providing strong linkages not drastically altering protein function [73], which is exploited to develop protocols for enzyme immobilization. Meanwhile, functionalization through perfluorosilanes such as 1H,1H,2H,2H-perfluorododecyltriethoxysilane (PFDS) provides hydrophobic and oleophobic properties, which induce antifouling ability, at least for proteins with few hydrophobic domains, reducing the tendency for protein molecules to adsorb, which is often problematic in microfluidic devices [74].

2.2 CHARACTERIZATION TECHNIQUES

2.2.1 TRANSMISSION ELECTRON MICROSCOPY

Transmission electron microscopy (TEM) operates on the same basic principles as the light microscope but uses electrons instead of light [75]. The technique is used to view thin specimens such as tissue sections, molecules, etc. To make a TEM analysis, samples need to be sliced thin enough for electrons to pass through, a property known as electron transparency. The arrangement of basic components in a TEM is illustrated in **Figure 2.4**. A fixed high voltage (hundreds of keVs) electron beam emitted by a cathode and formed by magnetic lenses is transmitted through the sample. After passing through it, the electrons form an image through the action of the objective lens and an objective aperture in the back focal plane of the lens. The image is corrected by an objective stigmator and enlarged by an image-forming system, which consists of a series of intermediate and projector lenses and alignment units. Thus, a highly magnified image becomes visible on the viewing screen. The electron beam that has been partially transmitted through the very thin sample carries information about the structure of the specimen.
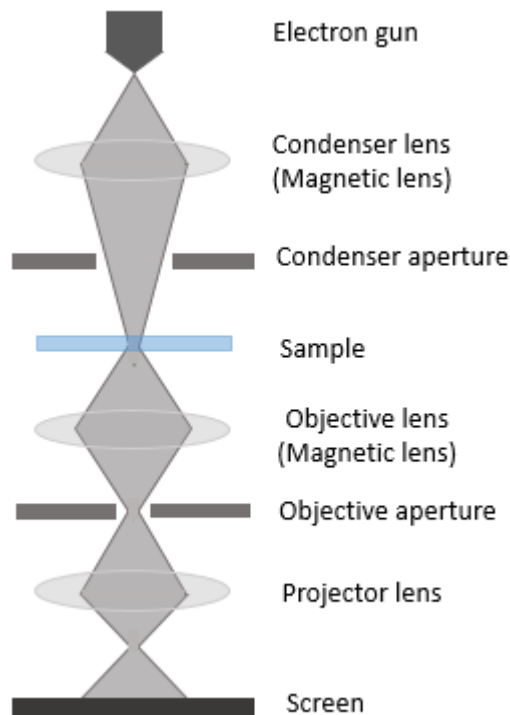
Figure 2.4 Basic components of a TEM.

This technique, used in a particular mode called Selected Area Electron Diffraction (SAED), allows the identification of crystalline structures and phases in single nanocrystals. One of the most important advantages of TEM is that it reaches extremely high magnifications, even to resolve single atoms. This is due to the very short De Broglie wavelengths of the accelerated electrons, which are comparable to the interatomic distance in a crystal. However, TEM usually requires a careful sample preparation, especially in the case of thick samples that need several steps to reduce its cross section [76].

2.2.2 SCANNING ELECTRON MICROSCOPY

Scanning electron microscopy (SEM) is a method for high-resolution imaging of surfaces [77]. It works by scanning a high energy electron beam across the sample and collecting the electrons emitted from its surface. When the electron beam hits the surface of the sample, it penetrates the sample to a depth of a few microns, depending on the accelerating

voltage and the density of the sample. Two categories of electrons are emitted to dissipate the primary excitation: low energy secondary electrons (E < 50 eV), produced by inelastic collisions in the incident beam electrons with the sample, and backscattered electrons (E > 50 eV) that arise from elastic collisions in the sample. The signals that derive from electron-sample interactions reveal information about the sample, including external morphology and chemical composition. A fundamental requirement of conventional SEM is the need for high vacuum conditions (10^{-5}–10^{-7} torr) throughout the system in order to prevent scattering of the primary electron beam. Electrons are produced at the top of the column, accelerated down and passed through a combination of lenses and apertures. The so produced focused beam impinges the surface of the sample mounted on a stage in the chamber area (**Figure 2.5**). The scattered electrons are captured by the different detectors and converted into images.

Electron gun

Condenser lens
(Magnetic lens)

Scan coils

Objective lens
(Magnetic lens)

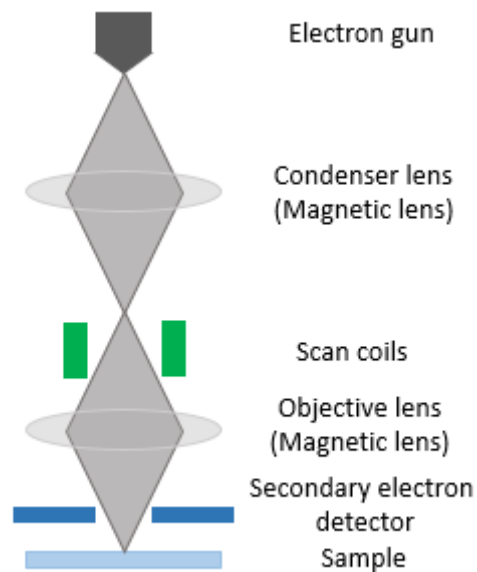Secondary electron
detector
Sample

Figure 2.5 Schematic of a SEM.

A significant advantage of using SEM compared to TEM is that the former can image the surfaces of bulk samples with a large depth of focus. However, in the case of non-conductive samples, a preparation generally consisting of the coating with metal or carbon is necessary in

order to avoid charging and increasing electron emission. An additional limitation is that only surface features are easily accessible.

2.2.3 WET SCANNING TRANSMISSION ELECTRON MICROSCOPY

In SEM, samples must be in a solid dry state. However, many biological specimens need to be maintained in liquid phase or contain volatile substances that evaporate under high vacuum. The environmental SEM (ESEM) is a good alternative for the observation of these samples. It differs from conventional SEM in two aspects. First, instead of the sample being held under a high vacuum, a gaseous environment is maintained around the sample whilst imaging is carried out. This is achieved by the use of differential pumping down the column, so that there is a series of different pressure zones, with increasing pressures as the sample chamber is reached (**Figure 2.6**). Moreover, a cascade amplification process occurs within the chamber, where the gas molecules are ionized by the electrons emitted from the sample. This helps amplifying the signal collected by a gaseous secondary electron detector. Each ionizing collision gives rise to a daughter electron, which is accelerated towards the positively charged detector, and further collisions can occur towards the detector. The positive ions drift back towards the sample surface and serve to compensate charge build-up at the surface of insulators. In consequence, insulators do not need to be coated with a metallic layer before imaging to prevent charging artefacts and consequent loss of image quality. This is the second major difference between conventional SEM and ESEM.
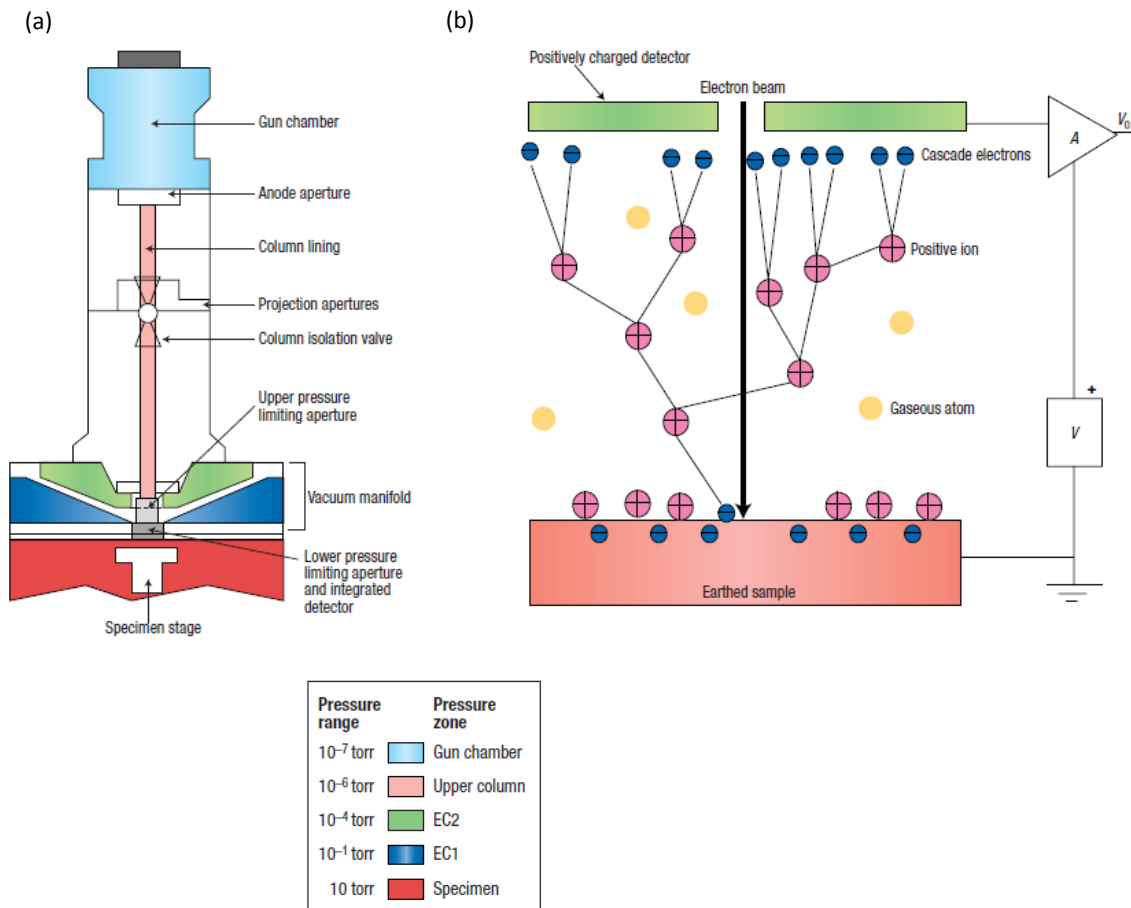
(a)

(b)

Positively charged detector

Electron beam

Gun chamber

Anode aperture

Column lining

Projection apertures

Column isolation valve

Upper pressure limiting aperture

Vacuum manifold

Lower pressure limiting aperture and integrated detector

Specimen stage

Cascade electrons

Positive ion

Gaseous atom

Earthed sample

A V_0

V

Pressure range	Pressure zone
10^{-7} torr	Gun chamber
10^{-6} torr	Upper column
10^{-4} torr	EC2
10^{-1} torr	EC1
10 torr	Specimen

Figure 2.6 Schematic of ESEM. (a) The different pressure zones in ESEM. (b) The cascade amplification process. Reprinted with permission from [78].

This versatile microscope can be operated at three principal levels: high vacuum, low vacuum and ESEM modes. High vacuum mode is basically the same as in conventional SEM and is used for the observation of dry, electrically conducting samples. Low vacuum mode involves a small partial pressure of gas in the specimen chamber (around 0.1–2.5 torr) and is used to study dry, electrically insulating specimens without a conductive coating. Finally, ESEM mode involves the specific use of water vapor in the specimen chamber and operates at higher pressures (around 2.5–10 torr) [79]. In order to prevent evaporation from, and condensation on the sample, an optimized pump down sequence is used. The signal is then collected by a detector usually used for the collection of backscattered electrons (BSE). The efficiency of signal amplification varies as function of gas pressure, detector type and gas type (nitrous oxide,

carbon dioxide, helium, nitrogen, water vapor, etc). In fact, each gas exhibits different amplification properties, but water vapor has been found to be the most efficient imaging gas so far tested, amplifying the signal arriving at the detector by a factor of up to 10^3. Besides, this microscope can be used in transmission mode (STEM-in-SEM). It is distinguished from conventional TEM by focusing the electron beam into a narrow spot, which is scanned over the sample. The electrons passing through the sample are then directly collected by a solid-state detector. The STEM is considered as a low dose technique. Indeed, the voltages available are low (20–30 kV) in comparison with the typical TEM operating energies, but inducing an improved contrast. Moreover, thanks to SEM characteristics, high angles can be used in a dark-field mode, with increased sensitivity for heavy atoms [80].

From the point of view of performance, STEM-in-SEM enables imaging with high resolution. As there is no projection lens, the electrons are not required to pass through it after crossing the sample. Chromatic aberrations are consequently avoided and the resolution is improved. Moreover, as the samples investigated are thin (in order to obtain important transmission signal) in comparison with those obtained in SEM, the interaction volume is small. For this reason, in STEM mode, the resolution is only limited by the spatial broadening of the electron beam at the exit surface of the sample, whereas structures at the entrance surface are resolved with a resolution of approximately same as the diameter of the electron beam. This is called the "top-bottom effect" [81].

The ESEM can also use the environmental mode (wetSTEM). The experimental set-up is composed of a TEM copper grid placed on the head of a TEM sample holder, which is fixed on a round cylindrical SEM mount, and positioned on a Peltier stage (**Figure 2.7**) [82]. The thin sample or a droplet of liquid containing particles or floating objects is placed on the grid and the incident electron beam passes through it.
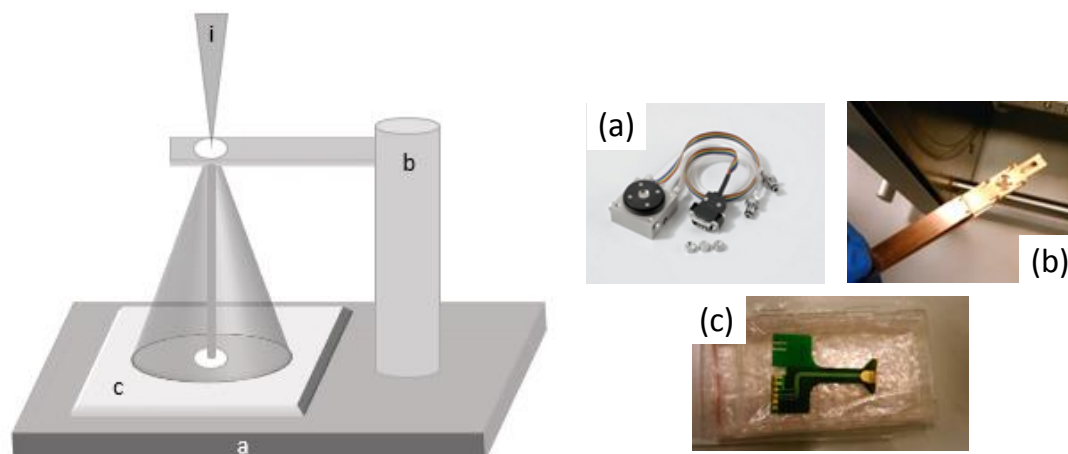
Figure 2.7 Schematic of the wetSTEM device. (a) Peltier stage, (b) SEM mount supporting

the droplet on a TEM grid, (c) solid-state detector, (i) convergent incident beam. Reprinted

with permission from [82].

The sample environment can be controlled by adjusting the chamber pressure and the sample

temperature through the Peltier stage. Selection of these parameters requires consideration of

the phase diagram (or saturated vapor pressure curve) for pure water, as depicted in **Figure 2.8**.

This makes possible to image wet samples. Indeed, specimens can be maintained in a liquid

state by holding an atmosphere corresponding to its equilibrium state. For instance, a water

pressure of 5.3 Torr is required at a sample temperature of 2°C, so that objects remain in a water

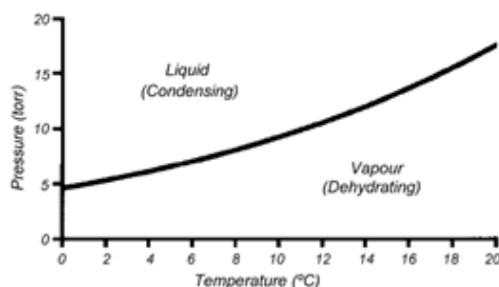layer with constant thickness (**Figure 2.8**).

Figure 2.8 Saturated vapor pressure curve for water. Reprinted with permission from [81].

Alternatively, pressures and temperatures can be chosen for non-equilibrium conditions, so that dynamic experiments involving evaporation or condensation of water can be carried out. This is especially relevant for the study of the effects of humidity on the samples. Due to its high resolution, the wetSTEM is particularly adapted to image nano-objects in a water layer, as illustrated in **Figure 2.9**. These examples demonstrate that metallic, inorganic and organic nano-objects in water observed in wetSTEM present improved resolution and contrast.
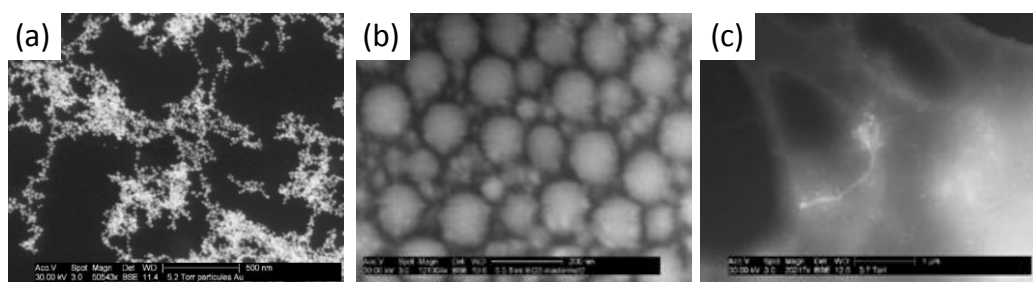

Figure 2.9 (a) Colloidal solution of Au nanoparticles imaged at 30 kV in wet mode with the annular dark-field STEM detector. Scale bar length: 200 nm [81]. (b) Colloidal solution of silica particles imaged at 30 kV in wet mode in annular dark-field conditions. Particles size ranges from 20 to 100 nm.[82] (c) Carbon nanotubes dispersed in water [81]. Reprinted with permission from [81] and [82].

Generally, biological specimens are difficult to see in conventional TEM because of their low contrast. Staining (i.e. heavy atom addition) can be a solution to increase contrast, although it is difficult to say whether the observed image features are artefacts or not. WetSTEM imaging constitutes a good way to circumvent the need for staining. It is for this reason and because specimens can be imaged without dehydration or coating that wetSTEM is of special relevance for biological applications. However, as yet it is not known whether living cells can be viewed but not killed by the electron beam.

ESEM proved to be a powerful imaging technique developed thanks to general progress in electron microscopy. In particular, STEM-in-SEM provides good advantages over conventional

TEM and allows straightforward transmission observations of wet samples with good resolution when performed in environmental conditions. Indeed, since no sample preparation is required previously, the samples can be imaged in their native state. Moreover, thanks to large collection angles and low operating voltages the contrast is enhanced, which is especially interesting for low atomic number materials. Nevertheless, in environmental mode (ESEM and wetSTEM modes) the resolution is limited by the mechanical vibrations caused by the cooling flow of the Peltier stage and by the vacuum system. Moreover, the presence of water makes the imaging sequence more delicate by inducing beam damage effects.

2.2.4   HELIUM ION MICROSCOPY

Helium ion microscopy (HIM) is a type of microscope that uses helium ions for surface imaging and analysis [83]. Its functionality is similar to a SEM, but it uses a focused beam of helium ions instead of electrons. Since helium ions can be focused into a smaller probe size and provide a much smaller interaction volume at the sample surface compared to electrons, the HIM generates higher resolution images with better material contrast and improved depth of focus. The HIM offers some advantages over traditional SEM technology. SEM's typically produce one secondary electron for each incoming electron. The helium ion beam, by contrast, produces from 3-9 secondary electrons, depending on the substrate material, for each incoming helium ion. This creates a better signal with higher contrast between different materials. Three of the fundamental challenges in the SEM imaging of soft materials are: the limited imaging resolution at high magnification, charging caused by the insulating properties of most biological samples and the loss of subtle surface features by heavy metal coating. These challenges have been overcome with the development of the HIM, which boasts advances in charge reduction, minimized sample damage, high surface contrast without the need for metal coating, increased

depth of field, and 5 Å imaging resolution, all of which are of relevance for studies of mesoporous structures.

2.2.5   WATER CONTACT ANGLE MEASUREMENTS

The water contact angle (WCA) is a technique that indicates the degree of wetting when a solid and a liquid interact [84]. In a simplified conventional view, small contact angles ($\leq 90º$) correspond to hydrophilic surfaces while high contact angles ($\geq 90º$) correspond to hydrophobic surfaces. The contact angle is defined as the angle formed by the intersection of the liquid-solid interface and the liquid-vapor interface. The well-known Young equation [85] describes the balance at the three-phase contact of solid, liquid and vapor.

$$\gamma_{sv} = \gamma_{sl} + \gamma_{lv} \cos\theta_Y \qquad \textbf{Eq. 2.2}$$

The interfacial tensions, γ_{sv}, γ_{sl} and γ_{lv} (at the solid-vapor, solid-liquid and liquid-vapor interface, respectively) form the equilibrium contact angle of wetting, often referred to as the Young contact angle θ_Y. However, the Young equation assumes that the surface is chemically homogenous and topographically smooth which is not the case for real surfaces. Indeed, these latter exhibit a range of contact angles between the advancing and receding ones (contact angles formed by expanding and contracting the liquid in dynamic measurements, respectively) instead of having one equilibrium contact angle. In **Figure 2.10** (c), the droplet on real surfaces is presented.
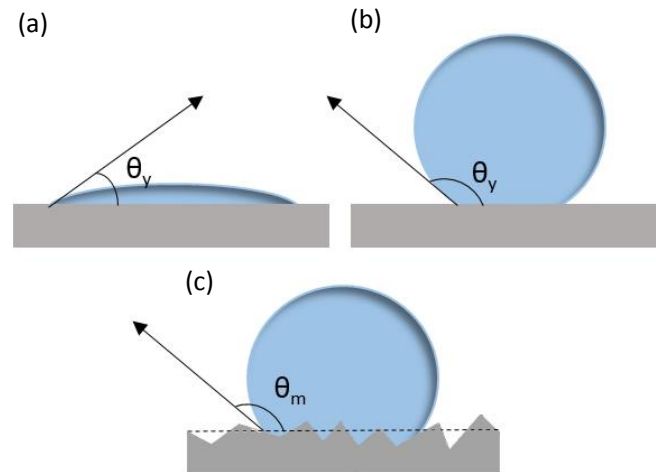
Figure 2.10 Young contact angles on ideal surfaces: (a) hydrophilic surface and (b)

hydrophobic surface. (c) Apparent or measured contact angle on rough (Wenzel) surface.

On rough and heterogeneous surfaces, the thermodynamic equilibrium contact angles are called

Wenzel [86] and Cassie-Baxter [87] angles respectively, and are not equivalent to Young's

contact angle. The relationship between roughness and wettability was defined already in 1936

by Wenzel, who stated that adding surface roughness enhances the wettability caused by the

chemistry of the surface. For example, if the surface is chemically hydrophobic, it will become

even more hydrophobic when surface roughness is added. Wenzel statement can be described

with **Eq. 2.3**.

$$\cos\theta_m = r \cos\theta_Y \qquad \textbf{Eq. 2.3}$$

where θ_m is the contact angle measured on a real rough surface, θ_Y is the Young contact angle

(model planar surface of identical surface chemistry) and r is the roughness ratio which is

defined as the ratio between the actual and projected solid surface area (r = 1 for a smooth

surface and > 1 for a rough one). Wenzel equation assumes that the liquid penetrates into the

roughness grooves. In cases where the liquid does not penetrate into the grooves (low surface

free energy surfaces), the Cassie-Baxter equation is used, and the apparent contact angle is

given by **Eq. 2.4**.

$$\cos\theta_m = x_1 \,(\cos\theta_Y + 1)\text{-}1 \qquad \textbf{Eq. 2.4}$$

where x_1 is the fraction of solid surface area wet by the liquid.

2.2.6   X-RAY PHOTOELECTRON SPECTROSCOPY

X-ray photoelectron spectroscopy (XPS), also known as electron spectroscopy for

chemical analysis (ESCA) [88,89], is one of the most powerful and common chemical analysis

techniques that not only allows identifying elements but also providing information regarding

chemical environments, oxidation states, and morphology. It enables qualitative elemental

identification for the entire periodic table, excepting H and He. This technique has been applied

to study many material types of a wide range of fields such as semiconductor processing or

biomedical engineering and consists of irradiating a sample surface with photons of

characteristic energy (usually Al or Mg K_α radiation). These photons directly interact with core

electrons of the sample atoms and a photoelectron from the ionized states created is emitted.

The binding energy of this photoelectron is characteristic of the orbital from which this latter

originates. The measured photoelectron spectrum is therefore a direct indication of the binding

energies of the different atomic electron levels. The kinetic energies of the ejected

photoelectrons, E_K, are measured by an electron spectrometer whose work function is ϕ.

Invoking conservation of energy, the following relationship is obtained:

$$E_B = h\nu - E_K - \phi \qquad \textbf{Eq. 2.5}$$

Where $h\nu$ is the photon energy and E_B the binding energy of the electron.

The photoelectrons are collected by electron optics and directed into an electron energy

analyzer, where they are sorted by energy (**Figure 2.11**). The number of electrons per energy

interval is then transduced to a current. The photocurrent is subsequently converted and processed into a spectrum by suitable signal processing. The data are then presented as a graph of intensity (usually expressed as counts or counts/s) versus electron energy - the X-ray induced photoelectron spectrum. The experiment is typically conducted under ultrahigh vacuum (UHV) conditions.
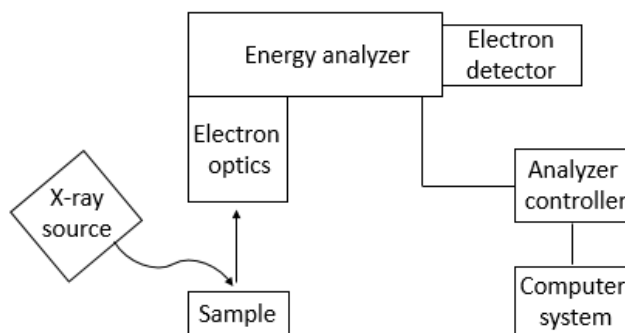

Figure 2.11 Schematic design of an X-ray photoelectron spectrometer.

2.2.7 FOURIER-TRANSFORMED INFRARED SPECTROSCOPY

Fourier-transformed infrared (FTIR) spectroscopy is a technique based on the vibrations of the atoms of a molecule [90]. When a sample interacts with IR photons, the beam produces vibrations and/or rotations on the molecule, causing a net change in its dipolar moment. For a vibration to give rise to the absorption of IR radiation, it must cause a change in the dipole moment of the molecule. The larger this change, the more intense will be the absorption band. The energy at which any peak in an absorption spectrum appears corresponds to the frequency of a vibration of a part of a sample molecule. Typical molecular vibrations are shown in **Figure 2.12**.
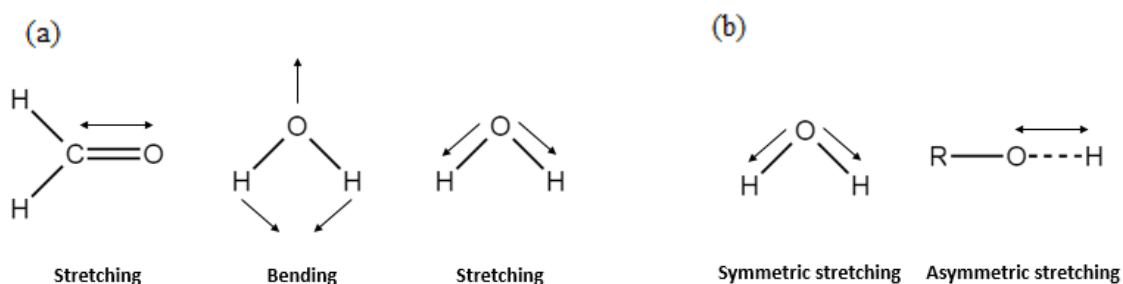
Figure 2.12 (a) Stretching and bending vibrations, (b) symmetric and asymmetric stretching vibration.

In particular, FTIR is based on the idea of the interference of radiation between two beams to yield an interferogram. The latter is a signal produced as a function of the change of pathlength between the two beams. The two domains of distance and frequency are interconvertible by the mathematical method of Fourier-transformation. The basic components of an FTIR spectrometer are shown schematically in **Figure 2.13**. The radiation emerging from the source passes through an interferometer to the sample before reaching a detector. Upon amplification of the signal, in which high-frequency contributions have been eliminated by a filter, the data are converted to digital form by an analog-to-digital converter and transferred to the computer for Fourier-transformation.
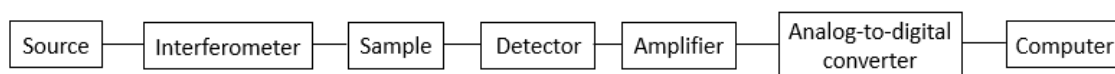
Figure 2.13 Basic components of a FTIR spectrometer.

FTIR instruments have several significant advantages over older dispersive instruments. Since FTIR spectrometry does not require the use of a slit or other restricting device, the total source output can pass through the sample continuously. This results in a gain in energy at the detector, hence translating to higher signals an improved signal-to-noise ratio. Another strength of FTIR

spectrometry is its speed. The mirror has the ability to move short distances quite rapidly, and this makes possible to obtain spectra on a millisecond timescale. The most straightforward IR method is the transmission spectroscopy. This technique is based upon the absorption of IR radiation at specific wavelengths as it passes through a sample. It is possible to analyze samples in the liquid, solid or gaseous forms when using this approach. Reflectance techniques such as attenuated total reflectance, specular reflectance or diffuse reflectance, may also be used for samples that are difficult to analyze by the conventional transmittance methods.

2.2.8   SOLID-STATE MAGNETIC NUCLEAR RESONANCE

Nuclear magnetic resonance (NMR) is a powerful tool used for structural determination and provides valuable information about molecular and supramolecular structures, packing arrangements, as well as molecular dynamics [91]. This is a non-destructive nor invasive, selective and quantitative technique consisting of immersing a sample with NMR active nuclei in a static external magnetic field and exposing them to a second oscillating magnetic field. **Table 2.2** presents the NMR properties for the isotopes of chemical elements commonly used for NMR experiments.

Table 2.2 NMR properties for selective isotopes.

NUCLEUS	SPIN (I)	NATURAL ABUNDANCE (%)	γ (10^6 RAD/T-SEC)	RESONANCE FREQUENCY (MHz/T)	SENSITIVITY (REL. H^1)
^1H	½	99.985	267.513	500.013	1
^2H	1	0.015	41.065	76.759	9.65E-03
^{13}C	½	1.10	67.263	125.720	1.59E-02
^{14}N	1	99.634	19.331	36.136	1.01E-03
^{15}N	½	0.366	-27.116	-50.687	1.04E-05
^{17}O	5/2	0.048	-36.264	-67.786	2.91E-02
^{19}F	½	100.0	251.66	470.382	0.834
^{29}Si	½	4.67	-53.190	99.325	7.84E-03

NMR spectroscopy has been used in a wide range of applications such as in the characterization of biomolecules, food products, bone, metals, etc. In particular, solid state NMR (ssNMR) constitutes the method of choice for the characterization of insoluble biological and synthetic chemical compounds since it does not require solubility and can be applied to proteins and complexes with molecular weights that exceed 100 kD, contrary to NMR in liquid state. In liquid, due to the fast motion of molecules, the distinct nuclear spin interactions (chemical shift anisotropy, dipolar and quadrupolar interactions) are averaged to zero and narrow resonance lines are obtained. These interactions are however operative in solids because of the small mobility of the molecules and lead consequently to a line broadening, hiding the essential information of analytical character. In order to remove this broadening and obtain high resolution, several methods have been developed. This can be achieved by spinning the sample around an axis inclined at the so-called "magic" angle (MAS) of 54.74º relative to the static magnetic field. If the spinning is fast enough, the line broadening is minimized. Indeed, at spinning rates greater than the NMR line width, the sample rotation leads to those components perpendicular to the rotation axis being zero. Only the component parallel to the rotation axis yields an average orientation parallel to the axis of rotation and becomes zero when the latter is inclined at the magic angle. Otherwise, the main resonance line is accompanied by a series of spinning side bands occurring at integral multiples of the spinning speed (**Figure 2.14**).
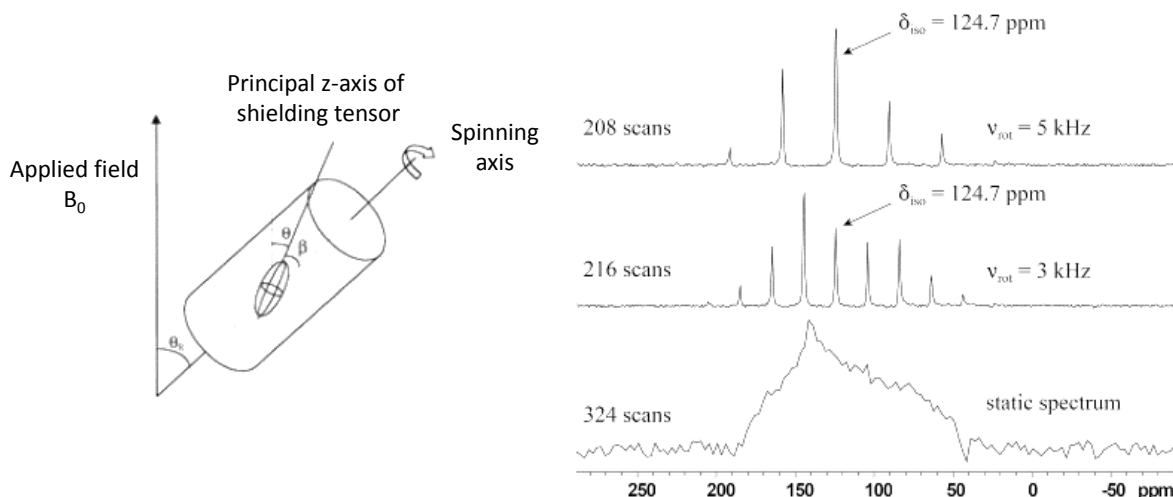
Figure 2.14 (a) Spinning the sample under the magic angle in ssNMR, (b) Sidebands at the multiples of the spinning frequencies appear in the spectrum and diminish with the increasing spinning rate. Reprinted with permission from [92].

In combination with MAS, pulse sequences are generally used to remove residual coupling and increase the resolution of the NMR spectra. Another technique often used to further enhance NMR sensitivity and resolution via line narrowing and one of the most important in ssNMR is the cross polarization (CP). This method allows transferring the magnetization or polarization from abundant nuclei like ^1H, ^{19}F and ^{31}P to dilute nuclei such as ^{13}C, ^{15}N or ^{29}Si to enable the selective detection of the dilute spin signal. In addition to providing surface selectivity, CP is also a well-known technique for enhancing the sensitivity of low gyromagnetic ratio nuclei having low spin-lattice relaxation rates. It is particularly useful to favor the detection of ^{29}Si in PSi where the majority of the protons resides on the surface.

2.2.9 OPTOPLASMONIC AND NANOMECHANICAL DETECTION OF GNPs

The vibration of microcantilever arrays is measured by the scanning laser beam deflection technique [93,94]. This consists of an automated two dimensional scanning of a laser

beam across the surface of the chip and the collection of the reflected beam on the surface of a two-dimensional position sensing linear detector (PSD) orthogonally oriented to the reflected beam (**Figure 2.15**). The laser beam sequentially scans all the cantilevers at their free end in the perpendicular direction to their longitudinal axes to follow their vibrations through the reflected beam position in the PSD. The microcantilever array is driven by a piezoelectric actuator located beneath the chip base.
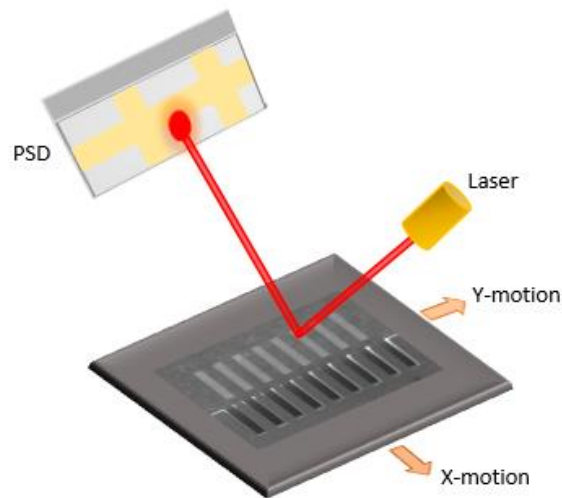
Figure 2.15 Schematic representation of the scanning laser beam deflection system.

For the optoplasmonic detection of the GNPs that tag the sandwich assay, we use dark-field microscopy in an optical microscope. The object is brilliantly illuminated against a dark background, which is accomplished using a special condenser composed of an opaque disc obstructing the path of light from the light source centrally, but allowing a peripheral ring of light (**Figure 2.16**). As a result, the images captured have a dark background and brighter particles, thus enhancing the contrast of the images.
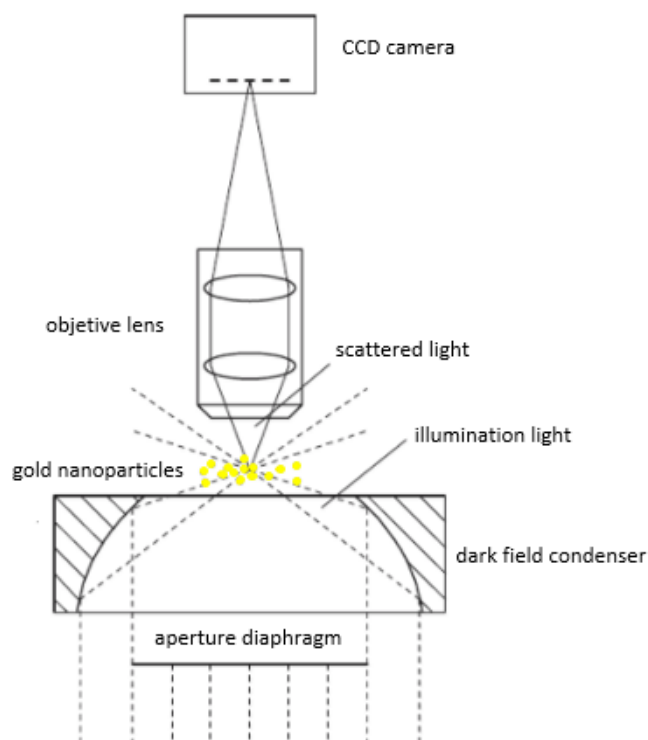
Figure 2.16 Schematic of dark-field microscope. Reprinted with permission from [94].

2.2.10 IMPEDANCE MEASUREMENTS

Impedance is the ability of a circuit element to resist the flow of electrical current and is defined as the ratio of an incremental change in voltage to the resulting change in current [40]. The changes in the impedance upon analyte binding are measured using a potentiostat which imposes a small sinusoidal voltage at a particular frequency (**Figure 2.17**). The resulting current is measured and the current-voltage ratio gives the impedance.
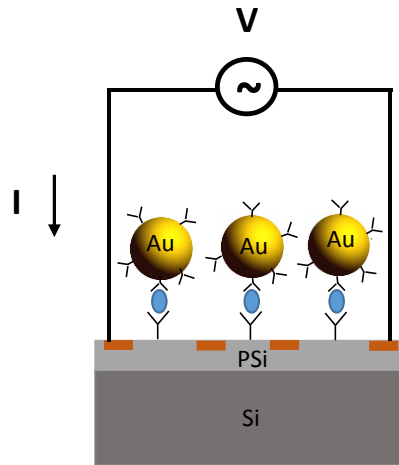
Figure 2.17 Schematic of the impedance measurement.

As a result of a frequency sweep in a determined range, a Nyquist diagram can be obtained. This diagram provides a direct view of the way in which the real component of the impedance varies with the imaginary component at each frequency, from higher to lower frequency. To fit the experimental data to a theoretical model, an equivalent circuit based on a combination of different components, such as resistors and capacitors, can be defined.

CHAPTER 3

FUNCTIONALIZED PSi

This chapter presents the process for the functionalization of PSi surfaces with different organosilanes and its characterization using complementary techniques (SEM, CA, FTIR, ssNMR and XPS) aiming at the demonstration of the efficiency of the visible light activation for the functionalization. The process is carried out onto both, planar and particle PSi structures taking account of the different potential applications and their adaptability to the different characterization techniques.

3.1 EXPERIMENTAL DETAILS

3.1.1 SYNTHESIS OF PSi

The back side of p-type boron-doped (100) oriented Si wafers were first coated with an aluminum layer to provide low resistance ohmic electrical contacts, and subsequently cut into 15 mm × 15 mm pieces, which were mounted into the sample holder. PSi was then formed by electrochemical etching of the silicon wafers in an aqueous electrolyte composed of a mixture of hydrofluoric acid (HF) (40%) and ethanol (98%). A volume ratio of 1:1 was used to form spongy-type PSi (PSi resistivity 0.05–0.1 Ω.cm). The current density was fixed at 80 mA/cm^2, and the anodization time at 20 s, leading to a 1 µm thick film.

PSi particles (PSips) were also formed using a current density of 80 mA/cm^2 for 15 min followed by a pulse of 5 s at 407 mA/cm^2. Free-standing PSi layers with a thickness of 72 µm were consequently obtained and then broken into particles directly in a vessel.

That allows obtaining a larger surface area and consequently sufficient sensitivity to detect the surface species of interest. The elaborated PSi particles were rinsed with ethanol and dried under ambient air.

3.1.2   PSi ACTIVATION AND FUNCTIONALIZATION

Three different chemical functionalizations of the PSi were performed using PFDS, GPTMS and APTS (Sigma Aldrich) (**Figure 3.1**). The silane-based solutions were prepared by dissolving the silane in solvent (0,2 % v/v) (EtOH for PFDS and APTS and in MeOH for GPTMS) and PSi was incubated in this solution for 30 min, 3 h and 10 min, respectively under visible light (150 W halogen lamp). Depending on the characterization method, we functionalized PSi in the form of particles or layer-on-Si wafer. The functionalization is followed by rinsing in the solvent used for the reaction and drying under N_2 flow. The whole process was carried out in a glove box filled with nitrogen.
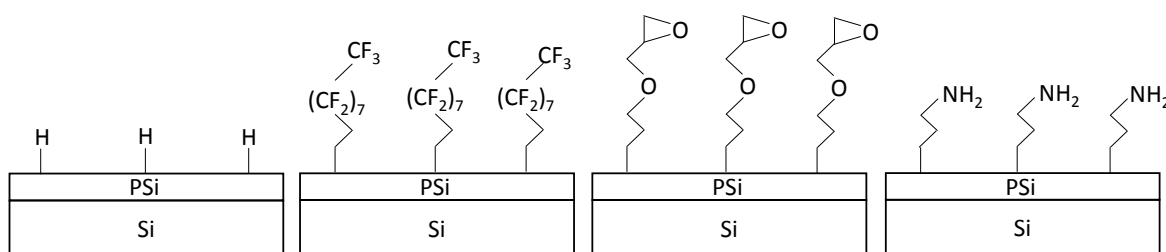

Figure 3.1 Schematic of the PSi surface chemistry for (from left to right): as-formed PSi, PFDS functionalized PSi, GPTMS functionalized PSi and APTS functionalized PSi.

3.1.3   CHARACTERIZATION

A pre-characterization of the pore structure of PSi was performed by using Field Emission SEM. Field emission SEM images were obtained in a Philips XL30S microscope operated at 10 keV.

The surface wettability of the PSi-on-Si samples was evaluated with a water contact angle goniometer (KSV CAM-101) used on the static sessile drop mode: a 5 μL drop of water was applied onto the sample surface and the contact angle formed with the surface was measured. Each measurement was repeated five times.

Additionally, their elemental composition was studied by XPS. The measurements were carried out with an SPECS GmbH photoelectron spectrometer with energy analyzer PHOIBOS 150 9MCD. XPS spectra were recorded using non-monochromatic Mg K_α excitation at pass energies of 75 eV for survey and 25 eV for high-resolution core-level spectra. The electron emission angle was 0° and the source-to-analyzer angle was 90°.

On the other hand, the characterization of the functionalized PSips was performed by FTIR using a Brucker Vector 22 (resolution 8 cm^{-1}, 4000-400 cm^{-1}, 32 scans at 10 kHz) in transmission configuration after preparation of KBr disks. NMR spectra were recorded with a Bruker AV-400-WB equipped with a 4 mm triple probe channel using ZrO rotors with KeI-F stopper at room temperature. The rotation speed was 10 kHz in all the cases. In the ^{13}C spectra, a cross-polarization (CP-MAS) pulse sequence was used between ^{1}H and ^{13}C nuclear spins with dipolar decoupling of ^{1}H at 80 kHz. The work frequencies were 400.13 MHz for ^{1}H and 100.61 MHz for ^{13}C. The spectral width was 35 KHz, the ^{1}H excitation pulse 2.75 μs, the contact time 3 ms and the relaxation time 4 s and 1k scans were accumulated. Adamantane (CH$_2$ 29.5 ppm) was used as secondary reference relative to TMS as primary reference. ^{19}F spectra were recorded with a double probe channel of 2.5 mm and rotors with Vespel stoppers. 2 μs pulses of 90º and a spectral width of 30 kHz were used. The recovery time was longer (120 s) than that used for the ^{13}C spectra acquired using CP because, contrary to ^{1}H nuclei, ^{19}F nuclei have large spin-lattice relaxation times [95]. The speed of rotation 20 kHz and the spectra were accumulated over night. Na$_2$SiF$_6$ (-152.46 ppm) is used as secondary reference relative to CFCl$_3$ as primary reference. Finally, in the ^{29}Si CP/MAS experiment, a ^{1}H excitation pulse of 3 μs was

used, corresponding to an angle of $\pi/2$. The spectral width was 40 kHz and the relaxation time 5 s. Caolin (-91.2 ppm) was used as secondary reference relative to TMS as primary reference. NMR analysis by ^{1}H → ^{29}Si CP/MAS is a surface selective technique favoring the detection of ^{29}Si at the surface. Indeed, the combination of cross polarization with magic angle spinning enhances NMR sensitivity and resolution via line narrowing [96]. On one hand, owing to its spin 1/2 and its high gyromagnetic ratio, ^{1}H provides high NMR sensitivity and can cross-polarize ^{29}Si at the surface.

3.2 RESULTS

3.2.1   PORE MORPHOLOGY

The SEM images shown in **Figure 3.2** highlight the pore morphology of the functionalized PSi samples in comparison with that of the original PSi. Wide fields are selected to identify the homogeneity of the surface at the scales where the pores start to be observable, while insets show a higher magnification view of the pore structure and distribution. The black holes represent the pores while the bright areas correspond to the Si pores walls. Some bright grey areas are also observed and correspond to clogged pores. We can note the similarity between the pristine PSi and the functionalized structures and the absence of any colloidal structure associated to the chemical modification of the surface with the silane SAMs.
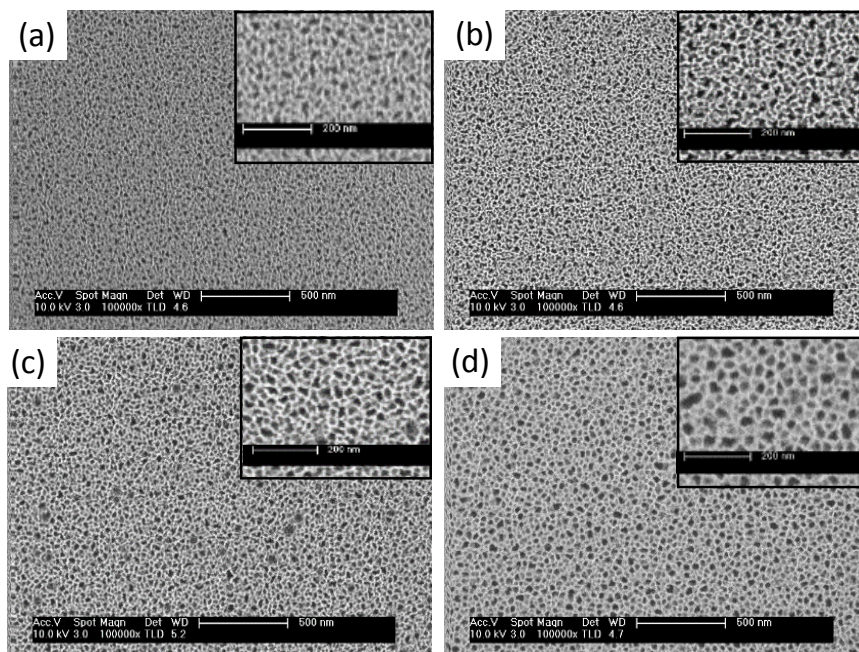
Figure 3.2 SEM image of (a) the surface of PSi, and PSi functionalized with (b) PFDS, (c) GPTMS and (d) APTS.

In the form of particles, PSi also maintains the porous nanostructure after the functionalization, as illustrated in **Figure 3.3**.
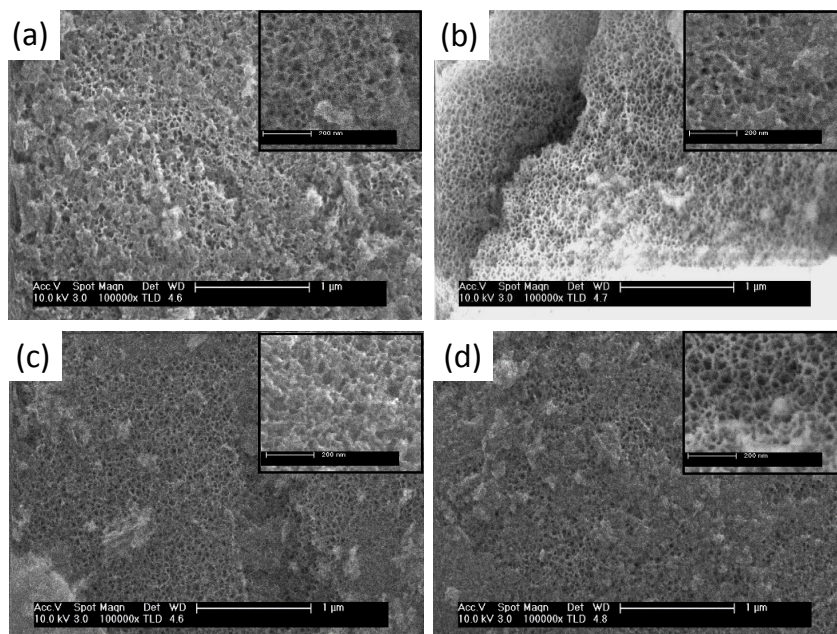

Figure 3.3 SEM image of (a) the surface of PSips, and PSips functionalized with (b) PFDS, (c) GPTMS and (d) APTS.

No significant change is observed between the PSips and the functionalized PSips. These results demonstrate that the modification takes place through a mild assembly of the organosilane. Indeed, the assembly is heterogeneous and does not consist of adsorbed structures issuing from a previous (in liquid) homogeneous organosilane nucleation. The process gives thus rise to a molecular assembly with no identifiable added nano-topographic structure.

3.2.2 SURFACE CHARACTERIZATION

The modification of the PSi samples allowed obtaining surfaces with different hydrophobic/hydrophilic properties. **Figure 3.4** showed the measured water contact angles after functionalization with the different organosilanes with and without visible light activation.
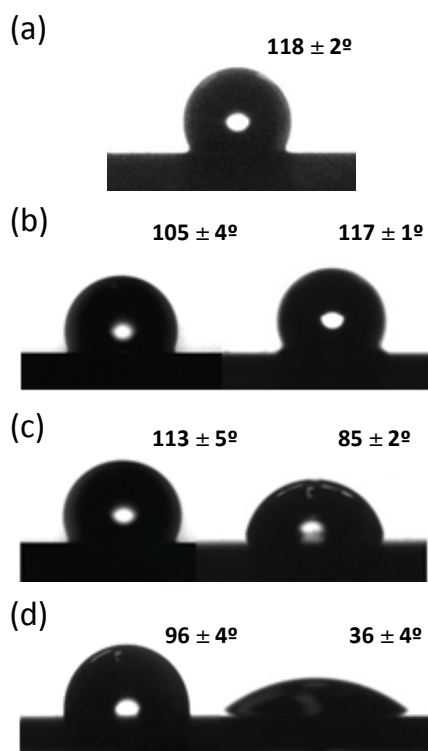

Figure 3.4 Static contact angle measurements of the (a) freshly-etched PSi surface, and for the functionalization of PSi with (b) PFDS, (c) GPTMS and (d) APTS with (right) and without (left) visible light activation.

After functionalization with PFDS and GPTMS with visible light activation, the surface is hydrophobic (117º) and only mild hydrophilic (85º), respectively. Meanwhile, the APTS-modified PSi surface shows a very hydrophilic behavior (36º). The values of the contact angles obtained are different from those that would be obtained on flat Si. Indeed, the pores play an important role in the roughness of the surface, which in turn influences the static contact angles [97,98]. The APTS-functionalized surface becomes more hydrophilic when the pores are formed (49º for the flat Si [99]) and can be described with the Wenzel model (assuming that the water penetrates into the pores) while the PFDS-functionalized surface becomes more hydrophobic (88º for the flat Si [100]) and can be described in this case with the Cassie-Baxter model. The functionalization of the PSi surface with GPTMS, however, leads to a higher contact angle than that obtained for the functionalized flat Si (48º) [100]. This is probably due to the less dense packing of GPTMS molecules on the surface. Therefore we have a polyfunctional surface which cannot be described with the two latter models but requires a hybrid model [101]. Without visible light activation, all the surfaces remain very hydrophobic, with WCA values close to those of the freshly-etched PSi. The very high contact angle of this latter sample (118º) is due to the SiH_x species covering the PSi surface [95]. The corresponding FTIR spectrum, in particular, reflects very well the presence of these reactive species (**Figure 3.5** (a)). We can clearly distinguish the scissoring modes at 624, 662 and 901 cm^{-1} and, on the other hand the stretching modes at 2085 and 2108 cm^{-1} [102]. After functionalization (**Figure 3.5** (b) to (d)), the peaks corresponding to SiH_x modes tend to disappear, suggesting that the surface has been transformed upon photo-assisted assembly. We can confirm the effective light activated oxidation of PSi through bands at 940-977 cm^{-1} (δ(-O_ySi-H_x)) and 2195-2249 cm^{-1} (ν(-O_ySi-H_x)). Additionally, we observe in all the visible light-induced silanized samples the presence of new peaks due to the aliphatic carbon chain at 575, 1318, 1382, 1472, 2849 and

2917 cm^{-1} corresponding to CH$_3$-C, δ_S (CH$_3$), -CH$_2$-, δ_{AS} (CH$_3$), ν_S (CH$_2$) and ν_{AS} (CH$_2$), respectively.

These peaks are however absent or very low in the spectra corresponding to the modified PSi without visible light, thus demonstrating the efficiency of the light activation. Evidence of oxidation and aliphatic presence are especially evident for APTS-modified PSi sample. Additionally, the peaks at 780, 1088, 1627 and 3435 cm^{-1} can be attributed to N-H$_2$, C-N, δ (N-H) and $\nu_{AS + S}$ (NH$_2$) respectively. However, in the case of the two latter modes, their identification is compromised due to overlapping with the broad water absorption bands caused by the moisture absorbed on the KBr disk [103]. In the spectra corresponding to samples with the other functionalization, the SiH$_x$ modes remain partially present, meaning that there is still some hydride species on the surface of the samples. However, in the case of visible light-induced GPTMS functionalized PSips, we can observe the characteristic IR absorption bands at 948 (asymmetrical ring stretching) and 800 cm^{-1}, that we do not see in the spectrum corresponding to the GPTMS functionalization without visible light activation. Additionally, the expected band corresponding to ring breathing at 1260-1240 cm^{-1} is not observed, certainly because of the overlapping with the strong Si-O-Si absorption band. The absence of the diol vibration bands at 4080 cm^{-1} proved that the epoxide ring did not open forming diols [104]. Finally, in the case of the sample functionalized with PFDS, the CF$_3$ group has a sharp characteristic band at the low wavenumber edge (858 cm^{-1}). The CF$_2$ group, owing to its four characteristic bands at 1133, 1149, 1208 and 1238 cm^{-1}, also appears to be an ideal group for tracing the functionalization [105]. Without visible light, however, the FTIR spectra do not present any of these characteristic peaks, proving that visible light activation is essential for the efficient attachment of the silane on the PSi surface.
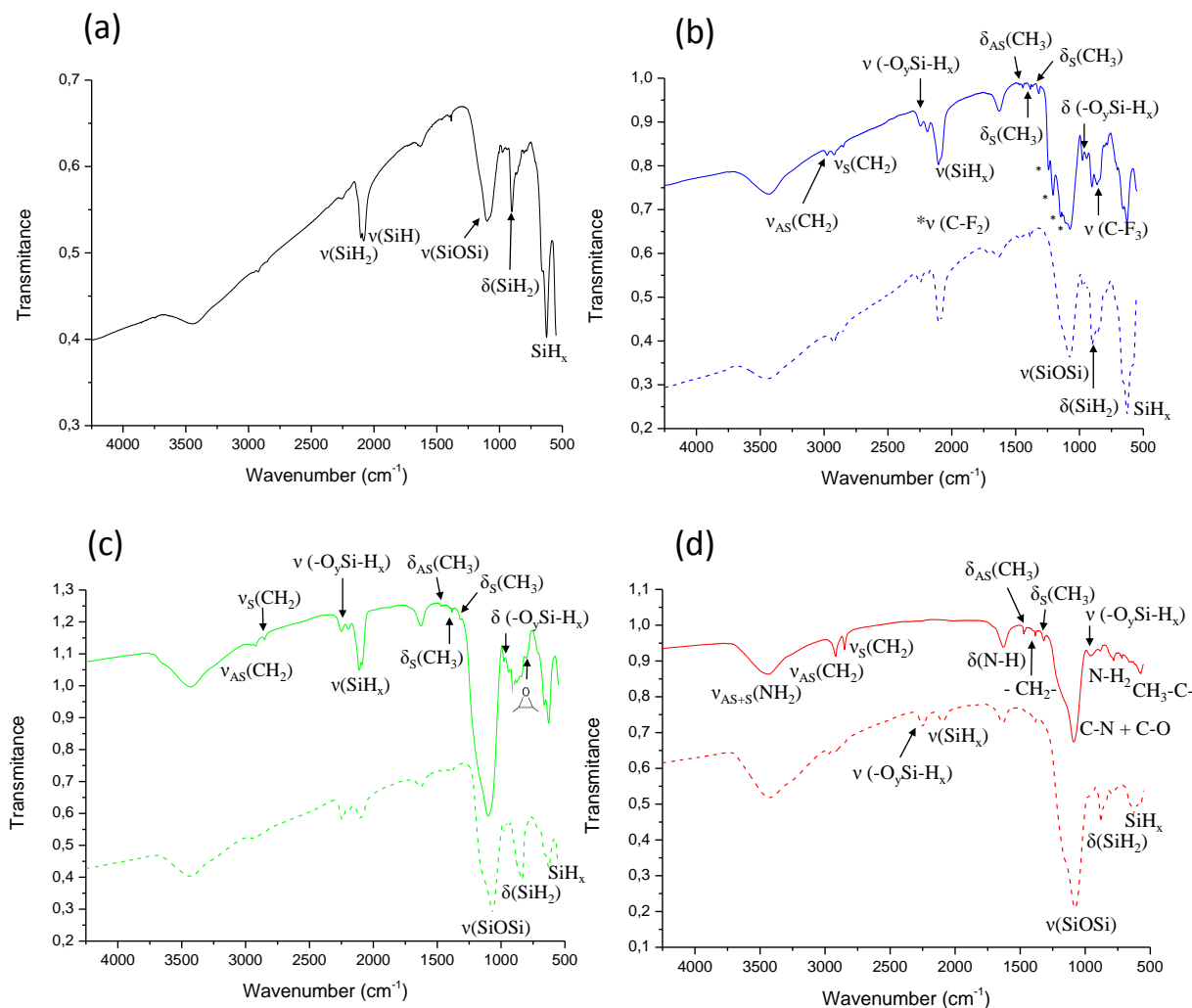
Figure 3.5 FTIR spectra of (a) PSi, and organosilane functionalized PSips with (solid curve) and without (dash curve) visible light activation. (b) PFDS-functionalized PSi, (c) GPTMS-funtionalized PSi and (e) APTS-functionalized PSi.

The overlapping of some characteristic bands in the FTIR spectra of PSips makes the univocal identification of molecular groups difficult. In order to overcome this issue, we used ssNMR spectroscopy and assigned the peaks on the basis of the correlation of the chemical shifts for other materials, in particular, functionalized silicates. Contrary to bulk Si, whose surface is inaccessible to NMR, PSips provide a sufficient number of surface nuclei to overcome NMR's inherently low surface sensitivity and achieve satisfactory signal-to-noise

ratio [106]. Such surface sensitive approach has already been used to characterize the organosilane adsorption on highly porous clay materials [107]. **Figure 3.6** shows the ^{29}Si NMR spectra of the PSips with different organosilanes compared with freshly formed PSips. In the spectra of the functionalized PSips, the chemical shift of the dominant signal is centered at −96 ppm, with a full width at half maximum of 20 ppm, which can be assigned to SiH or SiH$_2$ structural elements [108]. No signal corresponding to amorphous silicon (*a*-Si) (a very broad signal centered at -40 ppm) is seen. After functionalization, several peaks appear indicating the presence of different types of siloxane environments, which complement the signal of the underlying PSi. Indeed, the spectra exhibit peaks at -50, -63 and -67 ppm assigned to the Si atoms covalently bonded to organic groups R according to the three following categories:

- T^1 (SiO)Si(X)$_2$(R), with X=OEt, OMe and R= -CH$_2$CH$_2$(CF$_2$)$_7$CF$_3$, -CH$_2$CH$_2$CH$_2$OCH$_2$CH(O)CH$_2$ and -CH$_2$CH$_2$CH$_2$NH$_2$ for PFDS, GPTMS and APTS respectively.

- T^2 (SiO)$_2$Si(X)(R), with X=OEt, OMe and R= -CH$_2$CH$_2$(CF$_2$)$_7$CF$_3$, -CH$_2$CH$_2$CH$_2$OCH$_2$CH(O)CH$_2$ and -CH$_2$CH$_2$CH$_2$NH$_2$ for PFDS, GPTMS and APTS respectively.

- T^3 [(SiO)$_3$Si(R), R= -CH$_2$CH$_2$(CF$_2$)$_7$CF$_3$, -CH$_2$CH$_2$CH$_2$OCH$_2$CH(O)CH$_2$ and -CH$_2$CH$_2$CH$_2$NH$_2$ for PFDS, GPTMS and APTS respectively.

The presence of these condensation bonds, at different level depending on the silane considered, confirm in general the effectiveness in the activation for reaction of the three silanes with the PSi surface.
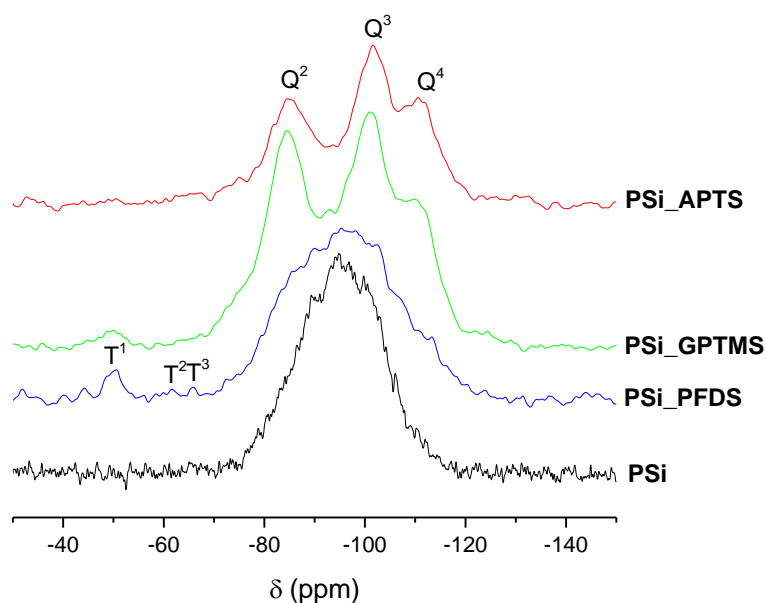
Figure 3.6 ^{29}Si NMR spectra of the organosilane functionalized PSips compared with the spectrum of freshly formed PSips.

As the electronic shielding of the central Si increases, the chemical shift becomes increasingly negative with each additional Si-O-Si linkage [109]. It is remarkable that the dominant intensity is observed at T1, which would indicate that the organosilanes are not fully condensed, especially in the case of PFDS (most intense T1 signal). This type of information on the reactivity at the surface is extremely relevant and cannot be extracted by using traditional spectroscopic techniques used for surface characterization of organosilanes such as X-ray photoelectron spectroscopy.

In addition, the peaks at -85, -101 and -109 ppm correspond to germinal hydroxyl silanol sites [$(O)_2Si(OH)_2$, Q^2], hydroxyl containing silicon sites [$(O)_3SiOH$, Q^3] and cross-linked Si [$(O)_4Si$, Q^4] respectively [96]. The high intensity of these peaks indicates that a significant part of the PSips surface is oxidized and hydrolyzed to form Q^n structures, further illustrating the effectiveness of visible light in the surface oxidation of PSips. In the case of PSips

functionalized with PFDS, these signals appear as shoulders of a main large peak at -95 ppm corresponding to the unreacted PSi. This means that the fluorosilane is effectively protecting the Si surface against hydration and hydroxylation.

Figure 3.7 presents the ^{13}C carbon spectra of the organosilane functionalized PSips. In the case of the GPTMS-PSips, the methylene carbons of the epoxide ring show resonances at 60.4 and 50.4 ppm, respectively, whereas the two oxymethylene chain carbon peaks appear at 72.8 ppm. The peak at 50.4 ppm also corresponds to the unreacted methoxy groups. Finally, the peak at 17.6 corresponds to the aliphatic chain [104].

In the spectra corresponding to APTS-PSips- and PFDS-PSips we observe peaks at 32 and 58 ppm due to the CH_3 and CH_2 carbons of unreacted ethoxy groups (OCH_2CH_3) [110]. Moreover, in the case of the APTS-PSips, the expected three characteristic signals of the aminosilane are present at 8.3 ppm (Si-$\underline{C}H_2$), 17 ppm ($\underline{C}H_2$-CH$_2$-NH$_2$) and 42.2 ppm ($\underline{C}H_2$-NH$_2$). The unfolding and the widening of the latter two signals as well as the shoulder of the peak corresponding to the CH_3 of the ethoxy groups at 32 ppm indicate the presence of a small portion of protonated amine. On the other hand, the signal at 21 ppm corresponds to the intermediate CH_2 of the aliphatic chain of amine [110-112].

In the spectrum corresponding to the PFDS-modified PSips, we observed small peaks at 16 ppm (Si-$\underline{C}H_2$-) and 24 ppm (Si-CH$_2$-$\underline{C}H_2$-) corresponding to the aliphatic chain. They are both shifted down-field because of the adjacent CF_2 groups. The small intensity of the signals confirms the data obtained in the ^{29}Si spectrum indicating that the condensation is not complete.
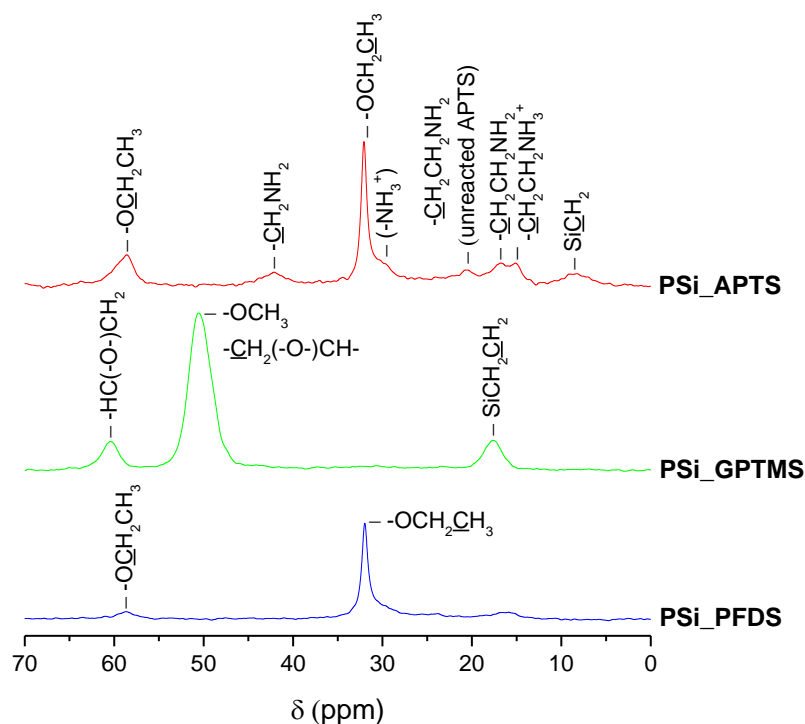
Figure 3.7 ^{13}C NMR spectra of the PSips functionalized with APTS, GPTMS and PFDS.

Since ^{19}F is one of the most useful NMR active nuclei (owing to 100% natural abundance, its relative high resonance frequency, and its spin quantum number of ½) [113] the ^{19}F NMR spectrum was obtained from the PFDS-PSips. Indeed, the ^{19}F NMR spectra of PSips and PFDS-PSips in **Figure 3.8** show no similarities. The spectrum corresponding to the PSips reference presents two peaks at -93 and -147 ppm corresponding to SiF$_3$H and SiF$_2$H species, respectively. In the spectrum of PFDS-PSips, we can clearly identify the peak corresponding to the CF$_3$ group at 83.8 ppm. The CF$_2$ groups give rise to peaks at 124.1 and 145 ppm [113].

In addition to the structural information provided by NMR, quantitative studies can be carried out owing to the direct proportionality between the signal intensity and the number of contributing nuclei. In the case of the functionalization with PFDS, we obtain a relation between the peaks corresponding to the CF$_2$ and CF$_3$ bonds in agreement with the molecular structure of the monolayer precursor (~7).
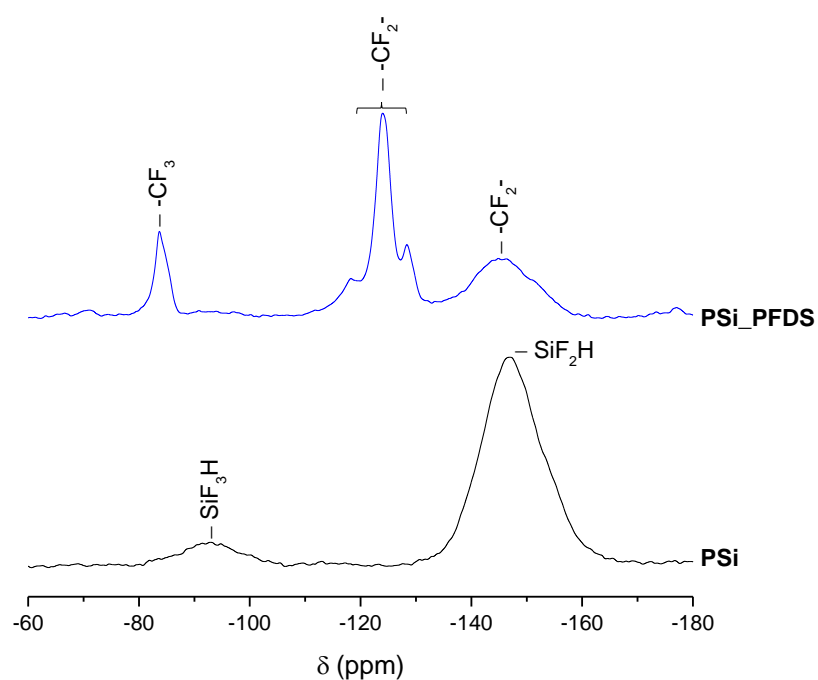
Figure 3.8 ^{19}F NMR spectra of PFDS PSips and fresh PSips.

However, in the case of the GPTMS and APTS-modified PSi, the use of cross-polarization for the acquisition of ^{13}C spectra makes any quantitative analysis impossible. Therefore, we performed XPS measurements. **Table 3.1** presents the elemental surface composition of the APTS- and GPTMS-modified PSi surfaces measured by XPS, evidencing the presence of C, O, Si, N and F species on the surfaces (F as a trace of PSi anodization process). In the former, the visible light activation promotes an organic stratum of 23.2 at. % C, which is enough to sustain a N composition of 3.2 at. %. The survey spectrum from a GPTMS layer functionalized during 3 h evidenced the presence of C (28.8 at %), O (19.6 at %), Si (51.2 at. %) and F species (0.5 at. %) on the surfaces (F as a trace of PSi anodization process).

Table 3.1 Elemental surface composition (± 0.5%) of the APTS and GPTMS surfaces after visible light activation as measured by XPS.

ELEMENT (%)	APTS	GPTMS
Carbon	23.2	28.8
Oxygen	42.3	19.6
Silicon	30.9	51.2
Nitrogen	3.2	-
Fluorine	0.4	0.5

A more detailed insight into chemical binding state and available surface species is provided by high-resolution C 1s, Si 2p and N 1s core level spectra. The C 1s spectrum of the APTS-modified PSi was resolved into three components at 285.1 eV, 286.0 eV and 287.1 eV related to the CH_2 groups of APTS (C1), C-N bonds and the carbon linked to free and protonated amino groups (CH_2NH_2) (C2) and C-O bonds (C3) [114]. Moreover, deconvoluted N 1s spectrum shows the occurrence of two nitrogenous species (**Figure 3.9**). The nitrogen component with the lowest binding energy, 402.2 eV (N1), shows the nitrogen contribution due to -NH- and the peak at 404.2 eV (N2) is assigned to the free and protonated amines. Therefore, the high-resolution XPS spectra of C 1s and N 1s of the APTS-modified PSi strongly suggests the presence of APTS on the surface of the PSi sample.
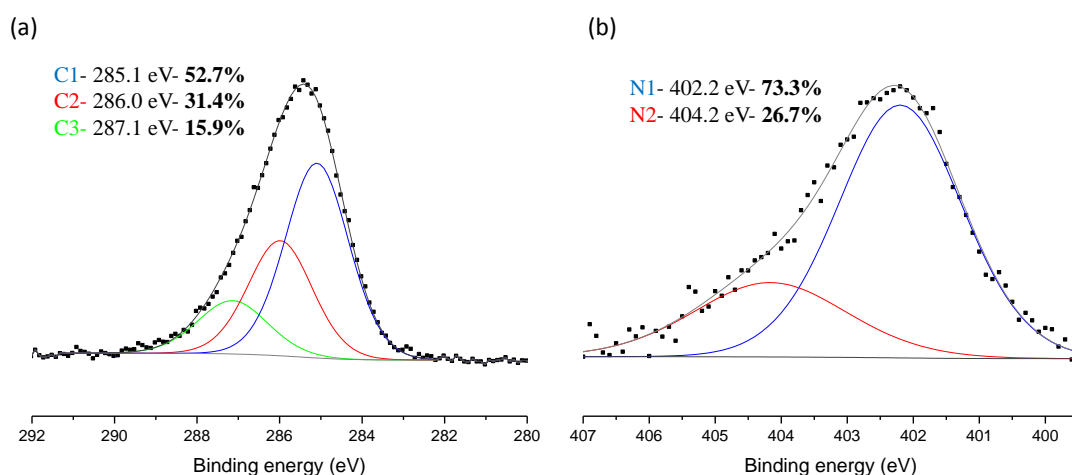
(a)

C1- 285.1 eV- **52.7%**
C2- 286.0 eV- **31.4%**
C3- 287.1 eV- **15.9%**

(b)

N1- 402.2 eV- **73.3%**
N2- 404.2 eV- **26.7%**

Figure 3.9 High resolution (a) C 1s and (b) N 1s XPS spectra of APTS-modified PSi.

Regarding the epoxy-modified PSi surface, **Figure 3.10** shows a deconvolution analysis of the corresponding C 1s and Si 2p spectra, which allows identifying the contributions of the different types of covalent bonds after 3 h of light activation. Regarding the C 1s spectrum (**Figure 3.10** (a)), in addition to the alkyl-related C-C/C-H component (C1) at 285.1 eV, a second component located at 286.6 eV is found that is assigned to C-O bonds of the epoxy and ether moieties (C2) of the GPTMS molecule [115,116], strongly suggesting the attachment of a GPTMS layer on the PSi surface. However, the measured peak area component ratio C1:C2 is very high (~ 4) compared with the ratio expected for a complete reaction [116]. It can be altered by the beam damage-induced contamination during the measurement [117], or can suggest a submonolayer regime for the GPTMS capping process. In the case of the Si 2p core level (**Figure 3.10** (b)), both elemental Si and Si oxide peaks were observed at 99.9 (Si1) and 103.0 eV (Si2), respectively. The Si oxide peak is due to oxidation of Si during activation with visible light by using residual moisture as reactant [118] and to the Si–O bonds from GPTMS [119]. By plotting the evolution of the Si2/Si1 peak area ratio along visible light activation time, a linear increase is observed, suggesting the visible light promotion of the PSi oxidation and GPTMS binding.

The same tendency is observed with the evolution of the C2/C1 peak area ratio with visible light activation time, thus demonstrating the attachment of the silane on the oxidized PSi surface.
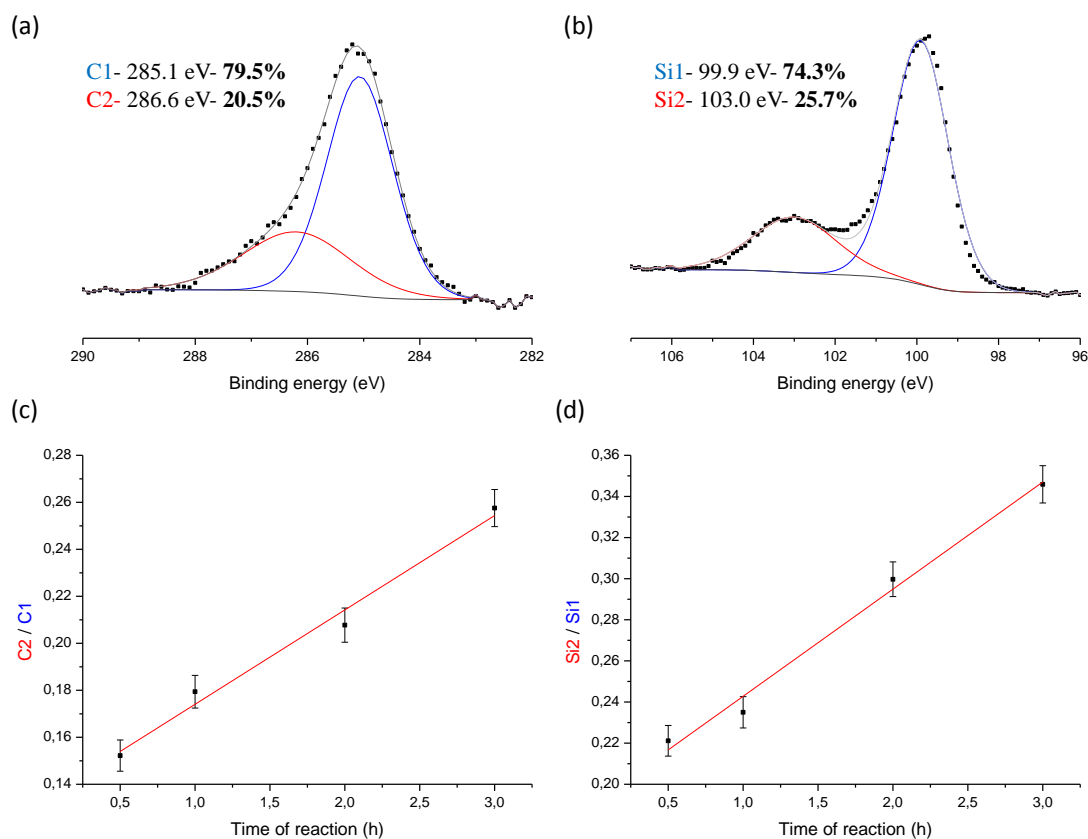
Figure 3.10 High resolution (a) C 1s and (b) Si XPS spectra of GPTMS-capped PSi after 3 h of light activation and (c) C2/C1 and (d) Si2/Si1 peaks ratio as a function of visible light activation time.

This result demonstrates that visible light catalyzes the oxidation of PSi. **Figure 3.11** presents a possible mechanism for the visible light activation of the PSi surface and further functionalization with the organosilanes. Contrary to ultra-violet (UV) light, visible light at room temperature does not provide photons with sufficient energy to promote the homolytic cleavage of the Si-H bonds. However, excitons (electron-hole pairs) are generated during the illumination of PSi at the H-Si surface due to photo-excitation [68]. This can facilitate the

nucleophilic attachment of trace water found in solvent and catalyze the further heterogeneous condensation reactions of the SAMs with the surface of the resulting oxidized PSi, avoiding previous thermal or chemical oxidation [69,70].

(a)

(b)

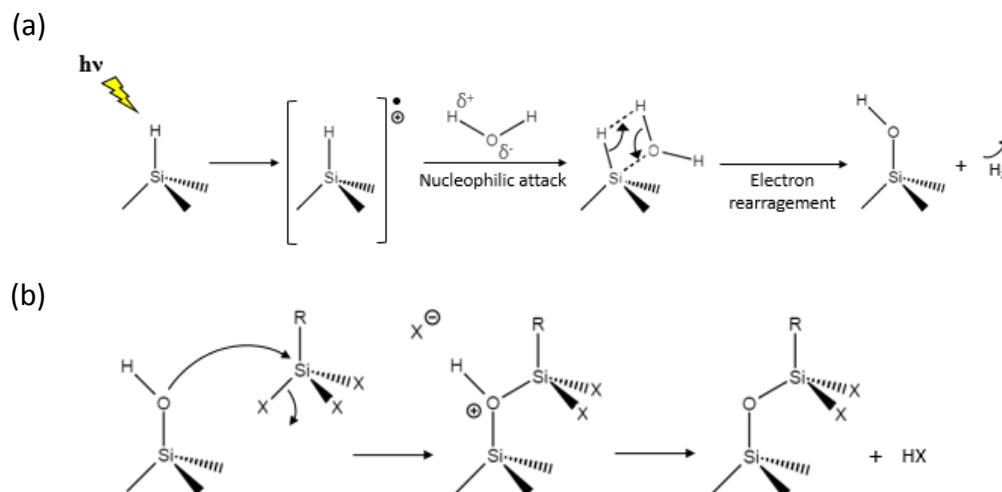**Figure 3.11** Proposed mechanism for the (a) visible light activation of PSi and (b) further attachment of SAMs on the oxidized PSi surface. X = OEt, OMe. R = -CH$_2$CH$_2$(CF$_2$)$_7$CF$_3$, -CH$_2$CH$_2$CH$_2$OCH$_2$CH(O)CH$_2$ and -CH$_2$CH$_2$CH$_2$NH$_2$ for PFDS, GPTMS and APTS respectively.

CHAPTER 4

WETTING OF FUNCTIONALIZED PSi

This chapter presents the wetSTEM study of the wetting dynamics of the organosilane modified PSi. This implies on the one hand a detailed pre-characterization of the system, performed through complementary microscopic techniques, and on the other hand, at the development of a technical protocol for wetting process control related to image processing.

4.1 EXPERIMENTAL DETAILS

4.1.1 PREPARATION OF PSi THIN LAYERS

Columnar PSi layers-on-Si wafers were fabricated by electrochemical etching of the silicon wafer in the aqueous electrolyte HF:EtOH (volume ratio 1:2). The current density and anodization time were fixed to 80 mA/cm^2 and 20 s. Columnar PSi thin layers were also fabricated. For that, we employed a current of 80 mA/cm^2 for 20 s followed by a pulse of 5 s at 407 mA/cm^2. That allowed us obtaining 2 µm thick free-standing PSi layers. They were removed from the electrolyte, washed with pure ethanol, and transferred to a copper TEM grid. The samples were then rinsed with ethanol and dried with N_2, which constituted the first group of target samples (fresh hydrolyzed PSi or H-PSi).

4.1.2 FUNCTIONALIZATION OF THE PSi LAYERS

The PSi layer-on-Si wafer samples and free-standing PSi layers were functionalized with APTS and PFDS (Sigma Aldrich), using the same protocol than that described in Chapter

3. The resulting target samples are labeled as APTS-PSi and PFDS-PSi, respectively. Aside from the functionalization, we also peroxidized the PSi thin layers using a mixture of H_2O_2 (30% wt in H_2O_2)/absolute EtOH (1:1) in order to obtain hydroxyl groups at the surface. The samples were immersed in the solution for 30 min and then rinsed in EtOH. This last group of target samples was labeled as Per-PSi. The whole process was carried out in a glove box filled with nitrogen.

4.1.3   CHARACTERIZATION OF THE PSi SURFACE

A pre-characterization of the pore structure of free standing PSi was performed by using Field Emission SEM, HIM and TEM. Field emission SEM images were obtained in a Philips XL30S microscope operated at 10 keV. High resolution imaging of the samples was performed with a Zeiss Orion NanoFab HIM at a landing ion energy of 30 keV. The nanostructure of PSi was observed by TEM in a JEOL 2100F located at Centro Nacional de Microscopía Electrónica and operated at 200 kV.

4.1.4   PERMEABILITY EXPERIMENTS

In order to study the water permeability of PSi and of the modified PSi samples, we dissolved phosphotungstic acid (PTA) in water (2% v/v) and placed a droplet on the surface of the PSi layer-on-Si wafer samples. Once the droplet has evaporated, we cut the sample in order to observe the cross-section by SEM.

The surface wettability of samples was also evaluated with a water contact angle goniometer (KSV CAM-101) used on the static sessile drop mode: a 3 μL drop of water was applied onto the sample surface and the contact angle formed with the surface was measured. Each measurement was repeated five times.

Focused ion beam (FIB) slicing and 3D imaging was performed using a dual-beam system FIB/SEM (FEI Helios 450S Dual BeamTM). The PSi samples, pre-coated with a 150 nm Pt protective layer, were sectioned parallel to the surface, removing slices one by one with the FIB working at an accelerating voltage of 30 kV and beam current of 18 pA. The image of each section was successively acquired by SEM (accelerating voltage: 5 kV; current: 100 pA) in high resolution mode. The process was run in fully automated mode, using the AutoSlice&ViewTM G3 software. The thus acquired 3D data cube was further processed, visualised and quantified in FEI VSG Avizo software.

4.1.5   WetSTEM EXPERIMENTS

Dynamic experiments involving condensation and evaporation of water on PSi were carried out with an ESEM-FEI QUANTA 250 used in transmission mode. The experimental set-up is composed of a TEM copper grid placed on a sample holder in a Peltier stage. Thin free-standing PSi samples are placed on the grid and so that the incident electron beam can pass through it. The transmitted signal is then collected by a backscattered electron (BSE) detector below the Peltier stage. The pressure was varied from the base pressure of $\approx 10^{-4}$ Pa up to >1000 Pa water vapor, supplied through an automated valve. In order to prevent evaporation from, and condensation on the sample droplet, an optimized pump down sequence is used (several cycles of water vapor filling at up to 1000 Pa, and pumping down to ≈ 100 Pa).

We used a beam voltage of 20 kV, with an electron beam spot of ≈ 13 nm (spot size 3). The dose and thus the beam damage was reduced by working at the minimal column aperture. The sample temperature was maintained at 5ºC (water vapor saturation pressure 866 Pa) by a Peltier element, and the relative humidity was increased/decreased by increasing/decreasing the chamber pressure. Thus, we allowed the water to condensate and evaporate. In order to avoid the beam damage, we kept low magnification at the beginning of the experiment, and we

zoomed to higher magnification only to acquire the images. Moreover, in order to consider and control the changes of chamber atmosphere with increasing humidity, and consequently the changes of image parameters such as contrast and brightness, we fixed a specific grey level to optimize the contrast for the complete vapor pressure range. To this end, we defined the µm thick copper grid as zero transmission (black), and the wide pores as maximum transmission (white), at high magnification at each level of RH. Any grey level is thus due to either Si or water. We kept the thus defined contrast setting when zooming, and when acquiring images. The results were correlated with water adsorption measurements of the different PSi samples (PSi layer-on-Si wafer samples) at room temperature performed using Belsorp-Aqua, co. Rubotherm/Bel. This equipment allows performing automatic vapor adsorption measurements using the volumetric gas adsorption method [49].

4.2 RESULTS

4.2.1 PROPERTIES OF THE COLUMNAR PSi

The SEM image in **Figure 4.1** (a) shows a general view of the columnar structure of the PSi obtained after electrochemical etching prior to delamination. The image shows the characteristic anisotropy of pores normal to the Si substrate. A higher magnification HIM image from the PSi/Si interface (**Figure 4.1** (b)) shows details of the pore wall structure, which contains dendritic features denoting a pore interconnection.
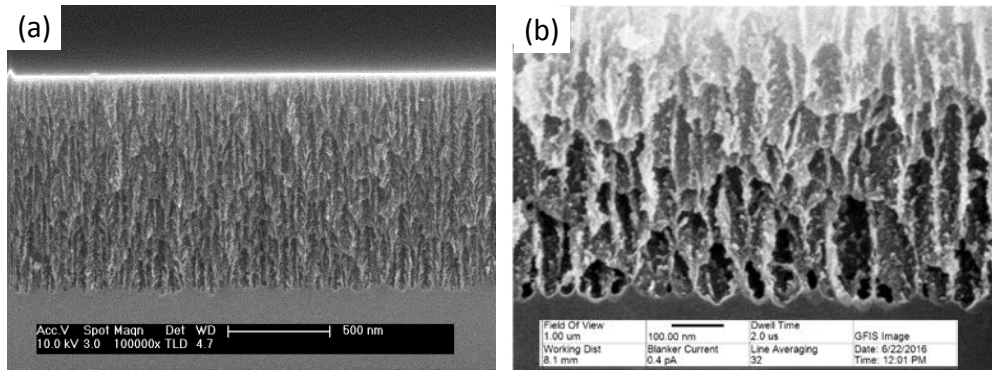
Figure 4.1 (a) Cross section SEM image of columnar PSi, (b) HIM magnification of the pores sectioned at the interface with Si.

The microstructure of the free-standing PSi was studied by TEM (**Figure 4.2** (a)). On one hand, the images highlight the verticality of the pores and on the other hand, the heterogeneity in size is also remarked. From the TEM images we were able to obtain a precise pore size distribution that we could fit to a Gaussian distribution establishing a cote of 38 nm to the mean pore diameter (**Figure 4.2** (b)). TEM was further used to investigate the local microstructure of the free standing PSi system. The squared selected area electron diffraction (SAED) pattern obtained from a beam converging on several pores (**Figure 4.2** (c)) indicates that the system maintains mainly its monocrystal structure with pores normal to the (100) planes. However, the widening and asymmetry (ellipsoidal shape) of the most intense diffraction peaks indicate deviations from the main monocrystalline structure and illustrate the presence of interface stress/nanostructuring in the pore walls. In fact, the higher magnification images from single pores (**Figure 4.2** (d)) allowed identifying different nanocrystalline structures by slightly tilting the sample until Si (100) planes were resolved (**Figure 4.2** (e)).
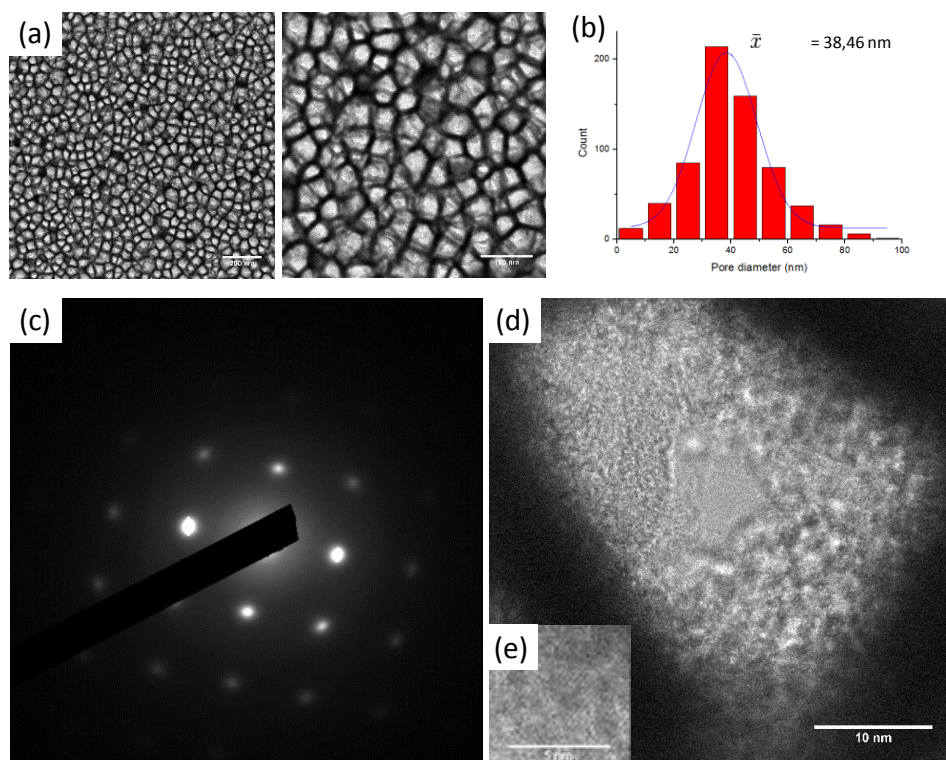
Figure 4.2 (a) TEM images of the general pore distribution of free-standing PSi, (b) Pore size distribution obtained from the TEM images fit to a Gaussian distribution, (c) SAED pattern of columnar PSi sample, (d) TEM image of a pore and (e) zoom in a Si nanocrystal.

The functionalization of the samples allowed obtaining surfaces with different hydrophobic/hydrophilic properties. **Figure 4.3** resumes the WCA and PTA infiltration results for the different PSi surfaces. The formation of PSi allows obtaining a more hydrophobic surface due to the presence of SiH_x species covering its surface [120]. Whereas PFDS-PSi presents approximately the same hydrophobic behavior as the H-PSi surface (contact angle of circa 120º), Per-PSi and APTS-PSi exhibited very hydrophilic surfaces (contact angles of 22 and 36º, respectively, **Figure 4.3** (a)). These results were complemented by studying the permeation of PTA solutions in water, which was reliably imaged by SEM (**Figure 4.3** (b)). PTA readily dissociates to anionic species; its chemistry is dominated by the outermost OH and O(-) groups, thus it is highly hydrophilic. The PTA staining used in TEM of biological samples

is indeed based on binding at cationic and hydrophilic surfaces, so we expected a high affinity to Per-PSi, and especially to APTS-PSi (the NH_2 groups form NH_3^+ in water). In fact, for H-PSi and PFDS-PSi, the water/PTA stays at the surface in the permeability experiment. Meanwhile, for the two hydrophilic samples, the whole thickness of the porous layer is filled up with PTA, indicating that their pores are permeable, even prior to the formation of a free standing structure.

(a)

118 ± 2º   117 ± 1º   36 ± 4º   22 ± 2º

(b)
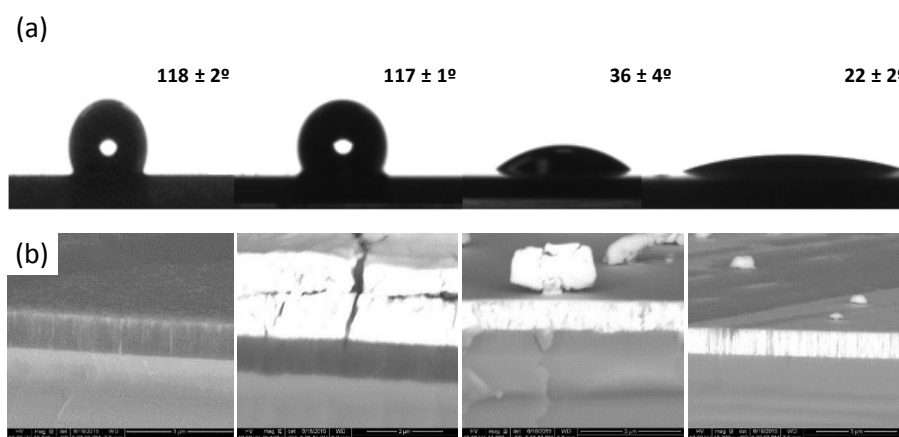
Figure 4.3 (a) Static contact angles of the PSi surfaces and (b) backscattered electron image of the cross-section of the PSi surfaces in presence of PTA. From left to right: as-formed PSi, PSi functionalized with PFDS, with APTS, and peroxidized PSi. From left to right: as-formed PSi, PFDS functionalized PSi, APTS functionalized PSi and peroxidized PSi.

Performing the same permeability experiment, we realized FIB tomography with the APTS-PSi sample (**Figure 4.4**). We note from the wide volume image that the water (PTA) reaches the bottom of the sample, which is in agreement with the previous SEM results. Furthermore, higher magnification tomography images from isolated surface pores made it possible to reconstruct the dendritic open pore structure of PSi (**Figure 4.4** (b)). In particular, a root like structure is observed with horizontally spreading pores at the surface converging later vertically at deeper levels. These results compare very well with the HIM data. Note that HIM

reveals the (internal) surface structure of the pores, while PTA staining/filling gives the 3D shape.
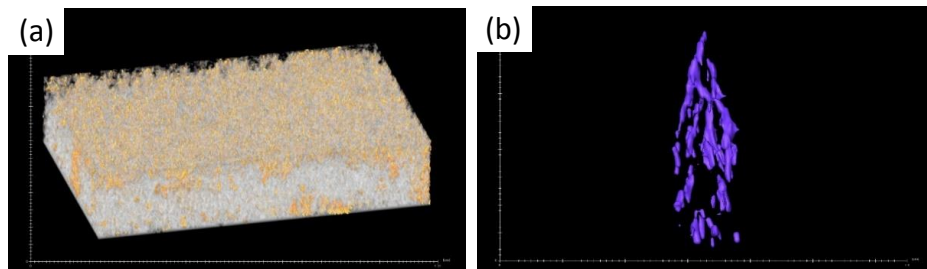
Figure 4.4 Three dimensional PTA enabled tomography images of (a) PSi functionalized with APTS and (b) a dendrite single pore structure magnification from the same sample.

The modification of the PSi surfaces by peroxidation and self-assembly of organosilanes therefore allows controlling their wetting.

4.2.2   CONDENSATION/EVAPORATION CYCLES BY wetSTEM

We carried out condensation-evaporation cycles in wetSTEM by increasing and decreasing the chamber pressure and acquiring images at each RH level. We were able to observe gradual water filling of the pores, as seen in **Figure 4.5**. Relevantly, the PSi structural integrity is not affected by the condensation and evaporation cycles, as we can see in the wetSTEM images of a region of the Per-PSi sample before and after wetting (**Figure 4.5** (a) to (e)). Capillary forces are in fact known to destroy nanoscale structures so that establishing this stability is key for establishing columnar PSi as a model surface [121]. Analogue images were collected for the different types of surface finishing and the electron transmission was analyzed according to pore diameter and vapor pressure.
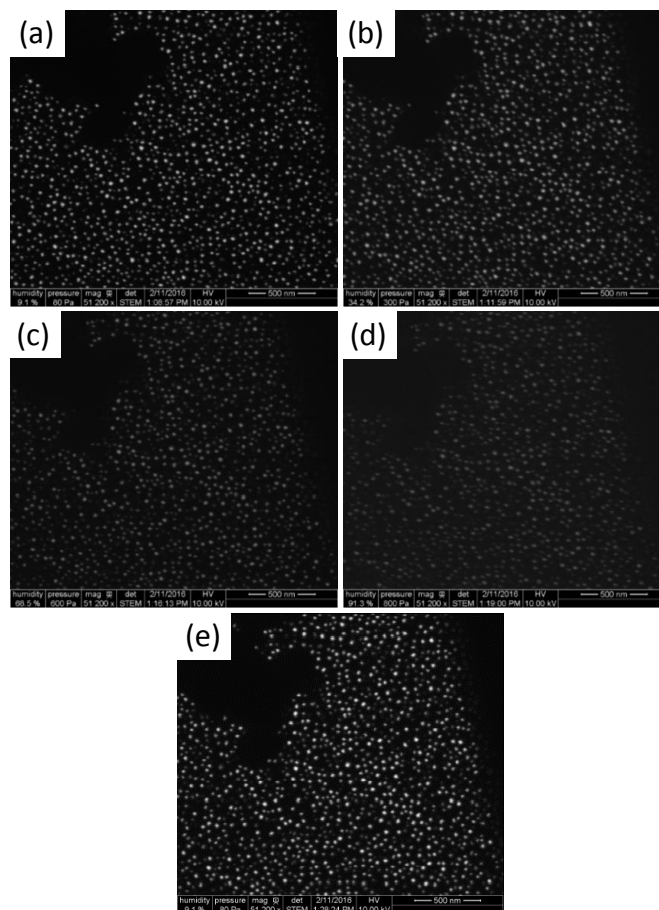
Figure 4.5 wetSTEM images from peroxidized free-standing PSi at increasing humidity: (a) 9.1 %, (b) 34.2%, (c) 68.5% and (d) 91.3% RH and (e) after wetting.

Figure 4.6 shows the electron transmission intensity profiles (gray value) through pores of 35 ± 2.5 nm of diameter, screened on a single pore basis, for the four types of PSi samples. Analogue plots were obtained for pores in the 20, 25 and 30 ± 2.5 nm ranges. The contrast (gray value) within dry pores during the condensation cycles is much higher in the case of APTS-PSi and Per-PSi (on a 256 gray scale level, from 45 to 160 and from 100 to 210, respectively) than in the case of the other two samples (from 50 to 105 for H-PSi and from 70 to 135 for the PFDS-PSi). This apparently leads to the occurrence of competing multilayer adsorption and capillary pore condensation mechanisms in the studied mesopores, whose balance point is determined by a value of the RH and depends on the surface chemistry. In fact, the sorption behavior depends

not only on the water-pore wall attraction, but also on the attractive interactions between the water molecules. At low RH, the pore walls are covered by an adsorbed water multilayer [122]. When the lateral interactions between adsorbed water molecules become stronger than the interactions between the PSi surface and water, capillary forces dominate, which takes place at relatively high RH. This last step occurs at lower RH in the case of the Per-PSi and APTS-PSi samples due to their more hydrophilic character.

We note that electron transmission strongly decreases with increasing RH, and relevantly also with decreasing pore diameter. This confirms that the smaller pores are filled faster than the bigger ones, as suggested by the Kelvin equation (**Eq. 4.1**), which provides a relationship between the pore diameter and the pore condensation pressure (P_c) and predicts that pore condensation shifts to a higher relative pressure and consequently higher RH with increasing pore diameter and temperature [122]:

$$\ln\frac{P_c}{P_0} = -\frac{2\sigma V_m \cos(\theta)}{RTr} \qquad \textbf{Eq. 4.1}$$

where σ and V_m are the liquid-vapor surface tension and the molar volume of the liquid, r is the pore radius, R is the universal gas constant, T the temperature, P_0 the vapor pressure of the bulk liquid phase of the water model at 298 K, and θ is the contact angle, which is assumed to be independent of r.
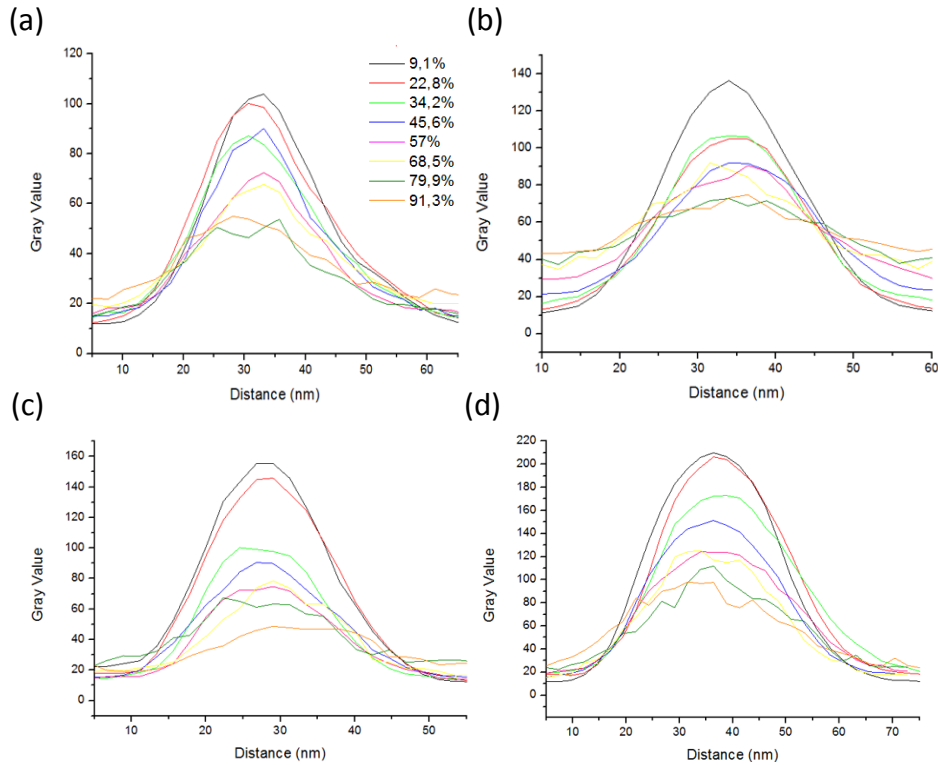
Figure 4.6 Pore (d=35nm) profile of (a) as-formed PSi, (b) PSi functionalized with PFDS and (c) functionalized with APTS and (d) peroxidized PSi.

From the pore profiles of the four samples we could obtain the normalized maximum gray value as a function of RH as shown in **Figure 4.7**. The gray scale is inverted in order to illustrate the increase of adsorption with water pressure as typically represented in gravimetric isotherms. We observe the formation of two groups as regards of the surface chemistry. On one hand, Per-PSi and APTS-PSi, whose pore surface is permeated easily, and on the other hand H-PSi and PFDS-PSi whose surface is resistant to water permeation. For a fixed vapor pressure, and taking into account the dynamics of the adsorption experiment, it can be stated that the gray value decreases much faster for the hydrophilic couple of PSi samples than for the hydrophobic couple, meaning that the pores are filled quicker.
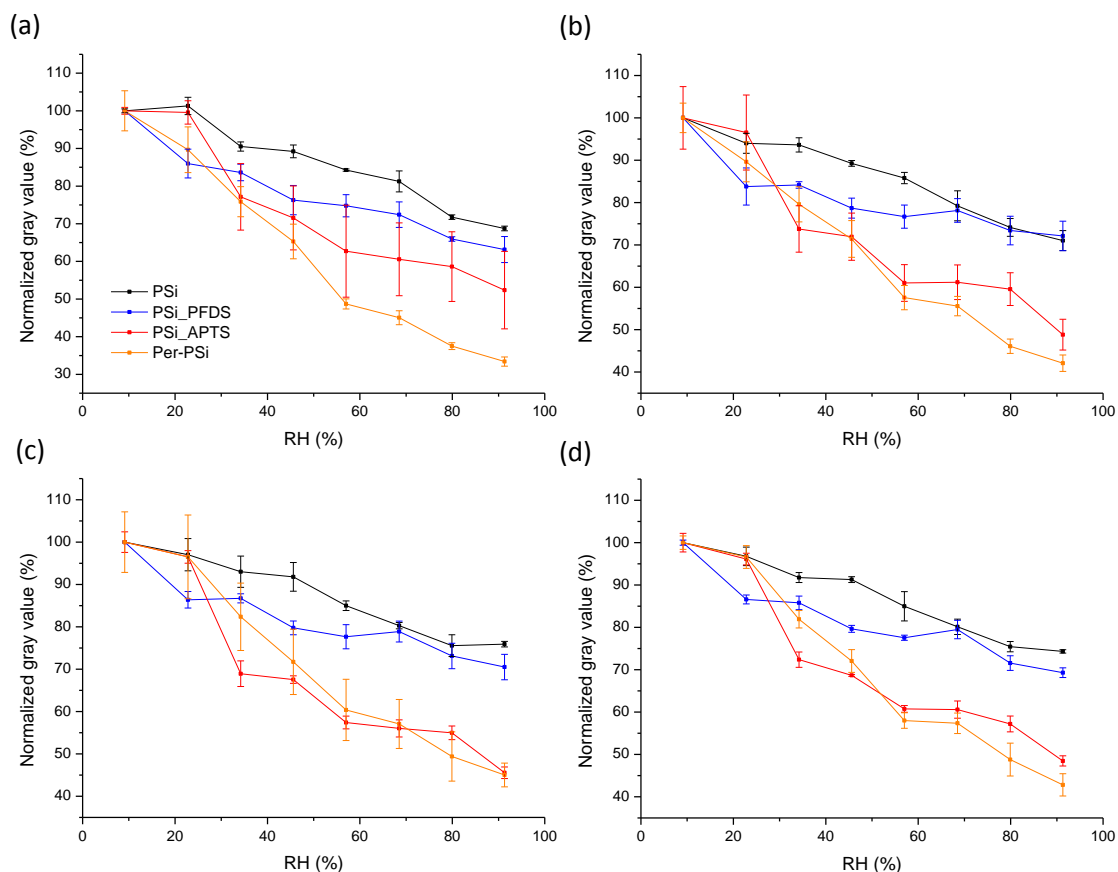
Figure 4.7 Normalized gray value as a function of RH (%) for pores of (a) 20 nm, (b) 25 nm, (c) 30 nm and (d) 35 nm of diameter and the different PSi surfaces.

This result confirms the observation obtained in the SEM images of the cross-section of the different PSi samples taken in presence of PTA (**Figure 4.3**). We can clearly see that in the case of the hydrophilic samples the water entered the pores in the whole thickness of the layer, contrary to the hydrophobic samples in which the water stayed at the surface. Therefore, depending of the hydrophilicity of the samples, a different filling mechanism should be expected. It is plausible that in hydrophobic samples, the water molecules form aggregates of several molecules instead of being uniformly distributed along the surface. Once a critical cluster size is reached, these aggregates coalesce to produce the condensed phase [123]. Therefore, the functionalization through perfluorosilanes such as PFDS provides hydrophobic properties [74] and may allow increasing the stability of the surface against the environment.

In hydrophilic pores, however, the water layer grows homogeneously. This suggests layer wise condensation of water on the pore walls, and the consequent faster filling of the pores [123].

4.2.3   CORRELATED WATER ADSORPTION MEASUREMENTS

Figure 4.8 shows the water adsorption and desorption isotherms of the PSi samples as function of RH measured with Belsorp-Aqua.
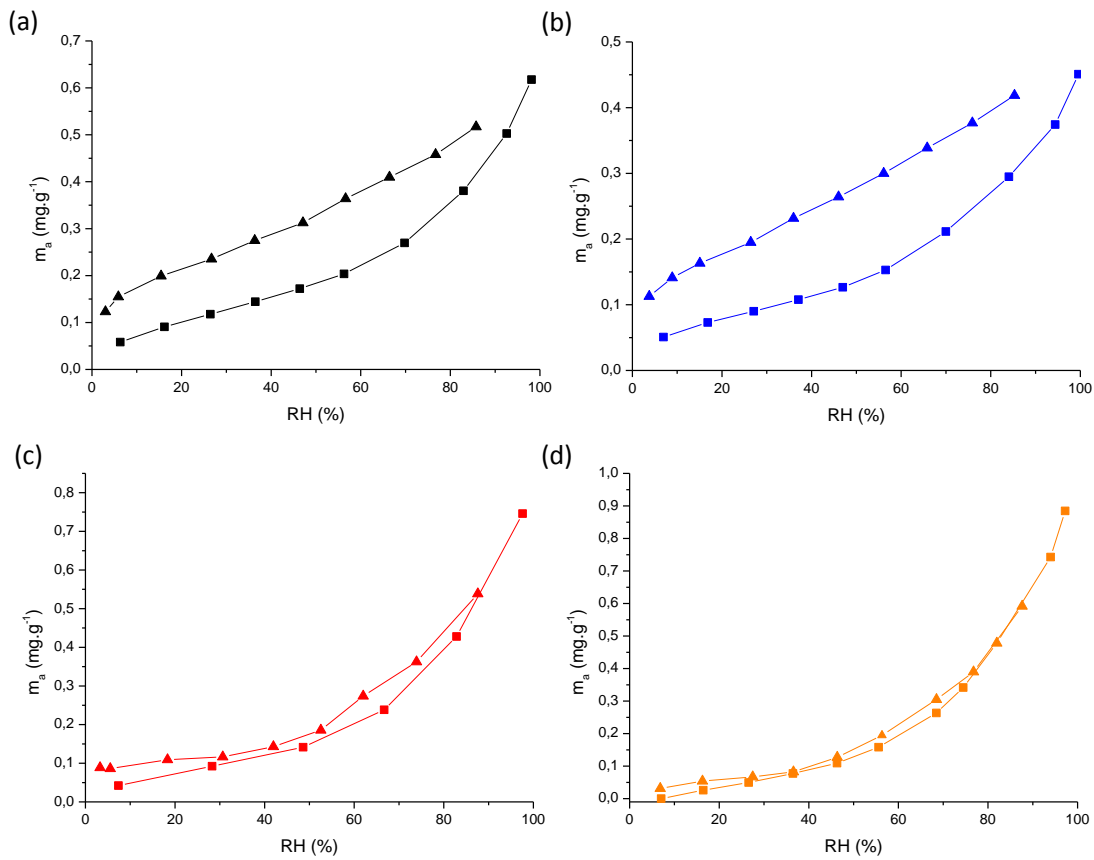

Figure 4.8 Water adsorption/desorption isotherms for (a) as-formed PSi, (b) PSi functionalized with PFDS and (c) functionalized with APTS and (d) peroxidized PSi. ■ Adsorption and ▲ desorption.

These isotherms allow yielding information about the wetting and the hydrophilic or hydrophobic properties of the samples. In the case of adsorption, the curves obtained are of type

III (classification IUPAC 1984) [124]. Upon the necessary change in ordinate scale, the results are in agreement with the wetSTEM measured adsorption, indicating a weak interaction of the water with the PSi surface yielding to condensation by capillarity. Indeed, according to the **Eq. 4.1**, pore condensation shifts to a higher relative pressure, and consequently to higher RH, with increasing contact angle. Besides, we observe the same tendency than that obtained with the wetSTEM experiments. Indeed, the amount of water adsorbed is very low for H-PSi and PFDS-PSi and is increased for Per-PSi and APTS-PSi. Although H-PSi and PFDS-PSi present almost the same contact angle (118º and 117º, respectively), they exhibit a different amount of adsorbed water. This can be due to the partial oxidation of H-PSi from the etching to the moment of analysis. Regarding the desorption curves, we also note a different behavior between the hydrophobic and the hydrophilic samples. The first ones present a two-step desorption isotherm indicating the existence of both equilibrium evaporation and pore blocking effects [125]. Indeed, from 90% to approximately 20% RH, desorption is associated to the evaporation of liquid from open pores. The observed final step down is however caused by the blocked mesopores remaining filled until they empty via cavitation. On the other hand, the more hydrophilic samples also present a two-step desorption curve following the path of the adsorption isotherm, as we can see in **Figure 4.8**. The water adsorption/desorption curves present a hysteresis, which is a consequence of the presence of pores with alternating wide and narrow parts. As the partial pressure of saturated water vapor is lower in the narrow pore necks, the evaporation is consequently slower than in the wider parts [126]. The observed hysteresis is larger in the case of the hydrophobic samples than in the case of the hydrophilic ones. This is probably due to the difference in contact angle between adsorption and desorption. Indeed, in the adsorption experiment, water molecules contact the pristine surface. However, in the desorption one, they draw back from a wet surface [127,128]. As the contact angle of the latter is smaller than that of the former in the case of the hydrophobic samples, large hysteresis is

observed, according to the Kelvin equation for desorption, which takes analogue form to **Eq. 4.1** but considers a desorption pressure P_d, instead of a condensation pressure P_c. Thus, the equilibrium desorption pressure P_d also depends on the pore hydrophilicity [127,128]. Moreover, we observe that the filling and emptying of the pore is not totally reversible. This effect is clearly more acute in hydrophobic samples, which are more susceptible to chemical reactions with water upon completion of condensation.

Consequently, this global gravimetric measurement of the sorption isotherms allows us confirming and obtaining more precise information about the wetting of the PSi samples and the mechanism of water adsorption and desorption. In particular, the difference in the hydrophobic/hydrophilic properties of the PSi surfaces, observed by the wetSTEM analysis and confirmed by the isotherms measured with Belsorp-Aqua, also plays an important role on the width of the hysteresis loop. This latter is enlarged by the hydrophobicity, as demonstrated by the Kelvin equation.

CHAPTER 5

APPLICATIONS

This chapter describes the formation of new dual sensing platforms based on PSi and GNPs. We transferred the formation of PSi and of biorecognition interfaces to nanomechanical and impedimetric platforms for the detection of PSA.

5.1 COMPOSITE PSi-Si NANOMECHANICAL BIOSENSOR

5.1.1   EXPERIMENTAL DETAILS

Formation of PSi on Si cantilevers

We used p-doped crystalline Si chips with 8 cantilevers per chip (Concentris). The nominal length, width and thickness of the cantilevers are 500, 100 and 1 μm, respectively. To form PSi layer on these crystalline Si cantilevers, we used the vapor phase stain etching method and we exposed the cantilevers to acid vapors issued from a mixture of HNO_3 and HF with a volume ratio 1:1. To start the process and initiate the formation of brown NO_x vapors, a piece of sacrificial Si was added to the solution. The chip, stuck on a Teflon lid, was then exposed to the vapors after 20 s for 30 s. Bigger pores were also generated by using a mixture of $HF:HNO_3$ with a volume ratio 2:1 with the same delay and exposure time.

Formation of a biorecognition interface

To demonstrate the significance of these composite PSi-Si cantilevers for biosensing, we performed a sandwich assay for the detection of PSA (**Figure 5.1**) [21].
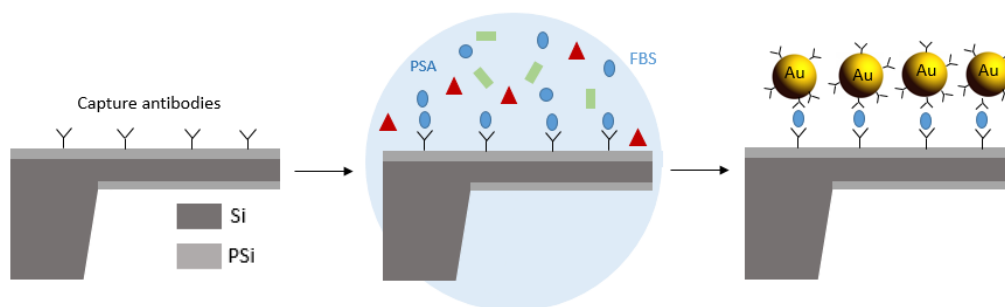

Figure 5.1 Schematic of the sandwich assay on the PSi-Si cantilevers. The cantilevers are first functionalized with capture antibodies against the sought protein biomarker. They are then immersed in the serum sample containing a complex array of proteins (green and red shapes) to allow the immunoreaction between the protein biomarker and the capture antibodies. Finally, the sandwich assay with the second antibody tethered to a 100nm diameter GNP takes place.

This experiment involves two biorecognition steps to enhance the selectivity and to amplify the sensor response. This first step includes a silanization with GPTMS, a molecule containing an epoxy group, which reacts with the SiOH groups on the surface of PSi (formed by the chemical oxidation) leading to a large surface density of epoxy groups. Then, the capture antibody (monoclonal mouse anti-prostate specific antigen 1H12 antibody) is immobilized on the top surface of the cantilevers and the free surface is blocked with polyethylene glycol (PEG) in order to avoid non-specific interactions. Then, an immunoreaction between PSA and the capture antibodies takes place by immersion of PSi-based devices in PSA:fetal bovine serum (FBS) 1x at a concentration of 1 μg/mL. The control is performed in FBS without PSA. The

serum contains a complex array of proteins, represented in **Figure 5.1** by the green and red shapes. Finally, a sandwich assay with the secondary antibody (anti-prostate specific antigen 5A6 antibody) tethered to 100 nm diameter GNPs takes place. The GNPs act as a mass and plasmonic label. We consider a sandwich bioassay with 100 nm GNPs to enhance the cantilever deformation, while at the same time creating an optoplasmonic label. In fact, in this size range the GNPs are small enough to induce plasmons, but are big enough to allow straightforward microscopic detection of light scattering (no contribution to background) [21].

Optoplasmonic and nanomechanical detection

The vibration of the microcantilever arrays was measured by the scanning laser beam deflection technique. We used a 3 mW red laser diode (Schafter-Kirchhoff, 635 nm) and linear voice-coil actuators for the laser scanning (Physik Instrumente GmbH& Co.). The laser spot size is 1 µm. The reflected beam is collected in a PSD designed by MecWins S.L., which provides total light collected on the PSD and the two-dimensional coordinates of the reflected laser spot on the PSD, independently of any light intensity fluctuations.

Dark field imaging was carried out with a Zeiss microscope (Axioskop 2 MAT) equipped with a high-definition color camera (Zeiss, AxioCam MRc 5). Measurements were performed in dark-field reflection configuration with an Epiplan Neofluar® 50X objective (Zeiss, N.A. 0.8). The red channel intensity of the dark field images was used to quantify the scattering intensity in a typical 8-bit scale (from 0 to 255). The images were processed with a home-made software developed in Matlab1. The program applies a mask based on size and color to the image for filtering-out the signal that arises from contamination of the surface. The scattering intensity is calculated by integrating the red channel intensity over the unmasked surface of the microcantilever. The scattering intensity signal is normalized to the scattering intensity obtained on a clean Si surface.

5.1.2   RESULTS

Device characterization

The PSi formed by vapor phase stain etching on the Si cantilevers is shown in **Figure 5.2**.
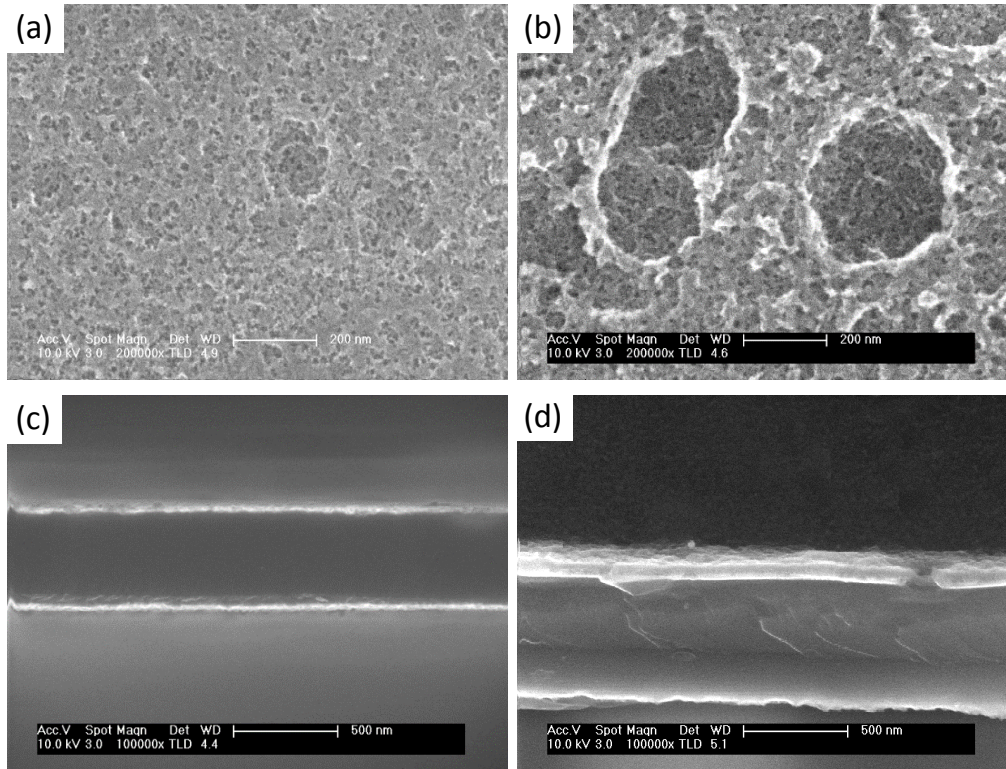
Figure 5.2 SEM images of the PSi layer on Si cantilevers. (a) HF:HNO$_3$ 1:1 and (b) HF:HNO$_3$ 2:1.

Its morphology is different from that obtained by electrochemical etching. We observe a dual macro and nano superposed structure. On one hand, the nanostructure is similar to that of the conventional anodically etched PSi and comes from the local reactions of vapor molecules with Si. The macrostructure, however, is due to the condensation of droplets. Indeed, as the temperature increases, the acid vapors form a fog leading to the appearance of small drops on the walls and particularly on the Si substrate. Using a HF:HNO$_3$ mixture with a volume ratio 1:1 (PSi1-Si cantilevers), the thickness of the cantilever is reduced from 1 µm to

approximately 550 nm and we obtain a PSi layer of 60 nm thick on each side. In contrast, increasing the proportion of HF in the acid mixture (HF:HNO$_3$ 2:1) (PSi2-Si cantilevers), a thicker PSi layer (about 140 nm) and bigger pores are obtained. The thickness of the cantilever is of about 640 nm. The dual macro and nano structure is in this case more pronounced. The final thickness of the cantilevers is however the same in both cases.

The formation of PSi on the Si cantilevers induces a change in the color of the cantilevers, as observed in the images of the dark-field microscope in **Figure 5.3** (b) and (c).
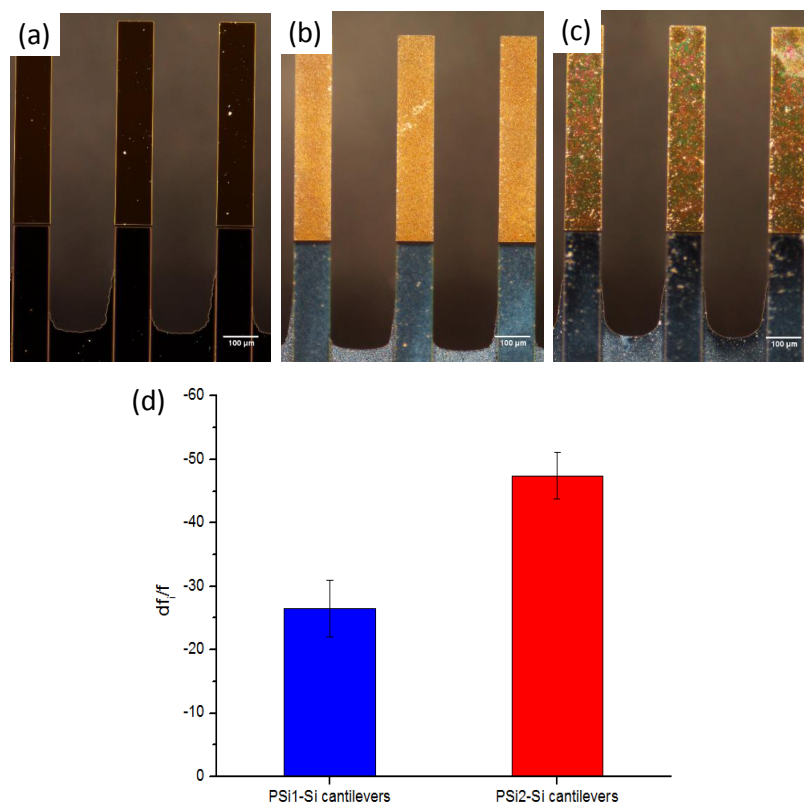
Figure 5.3 Optical images of the cantilevers (a) before and after the formation of pores: (b) PSi1-Si cantilevers (HF:HNO$_3$ 1:1) and (c) PSi2-Si cantilevers (HF:HNO$_3$ 2:1). (e) Mean value of the shift of the resonance frequency of the first mode of vibration of the PSi1-Si and PSi2-Si cantilevers.

This is due to the generated interferences which become more pronounced with increasing pore size and porous layer thickness. On the other hand, the formation of the PSi layer also leads to

a negative shift of the resonance frequency of the first mode of vibration of the cantilevers (**Figure 5.3** (d)), which is not only due to the increased roughness [129] but also to the decrease of the cantilevers thickness [130]. This shift is bigger in the case of the bigger pores but it is homogeneous within the two groups of porosity, which demonstrates the reproducibility of the vapor phase stain etching process.

Sandwich bioassay for the detection of PSA

We realized the bioassay with the different Si and PSi-Si chips and we analyzed the optical and nanomechanical responses for a concentration of PSA of 1 μg/mL. In order to discriminate biorecognition signals from non-specific interactions, a negative control experiment using serum without PSA was also performed. On one hand, we analized the cantilevers surface after their exposure to the GNPs by dark-field and electron microscopy. **Figure 5.4** shows dark-field microscope images of the cantilevers after the bioassay. The GNPs have a plasmon resonance at approximately 450 nm and, thus, appear as orange spots. We observe that the surface density of GNPs on the Si cantilevers is significantly higher in the case of the PSA-detection assay than in that of the control, which demonstrates the selectivity of the device. Moreover, particles can be clearly distinguished and their consequent enhanced light scattering can be quantified, as shown in **Figure 5.4** (e). Contrary to the PSA-detection assay, the scattering signal is negligible in the control experiment, demonstrating the specificity of the interaction between the anti-prostate specific antigen 5A6 antibody and the PSA. In the case of the porous cantilevers, only the GNPs on the surface of the PSi1-Si ones can be distinguished, the PSi2-Si cantilevers presenting too strong interference. Moreover, because of the heterogeneous background of the porous cantilevers, the quantification of the scattering intensity is not possible.
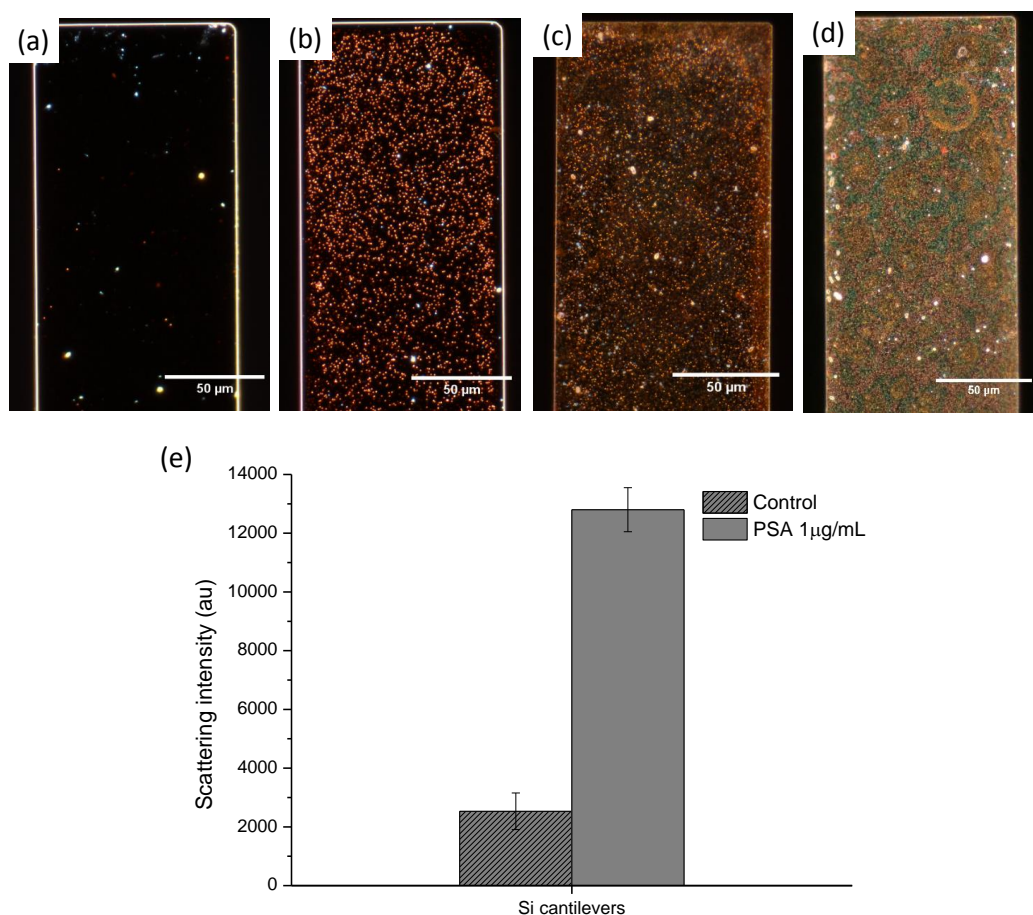
Figure 5.4 Dark-field microscope images of the cantilevers surface after the bioassay. (a) Si cantilever (control in FBS), (b) Si cantilever (PSA 1μg/mL), (c) PSi1-Si cantilever (PSA 1μg/mL) and (d) PSi2-Si cantilever (PSA 1μg/mL). (e) Quantification of the light scattering of the Si cantilevers surface for the control assay and for a concentration of PSA of 1μg/mL, normalized to clean Si.

Figure 5.5 presents SEM images of the Si and PSi-Si cantilevers surface after the bioassay. The GNPs surface density difference between the control (almost no GNP is detected) and the sample allows confirming the efficiency of the sandwich assay previously demonstrated with the dark-field microscope analysis. The higher atomic number of the GNPs (Z=79) with respect to that of the matrix elements lead to a very high contrast and allows distinguishing the particles

on all the porous cantilevers. While the density of GNPs on the Si and PSi1-Si cantilevers surface seems to be similar, that on the PSi2-Si cantilevers is significantly higher. This is probably due to the fact that the pores are big enough to allow the GNPs to enter them, which is not the case for the PSi1-Si cantilevers, as seen in the insets in **Figure 5.5**.
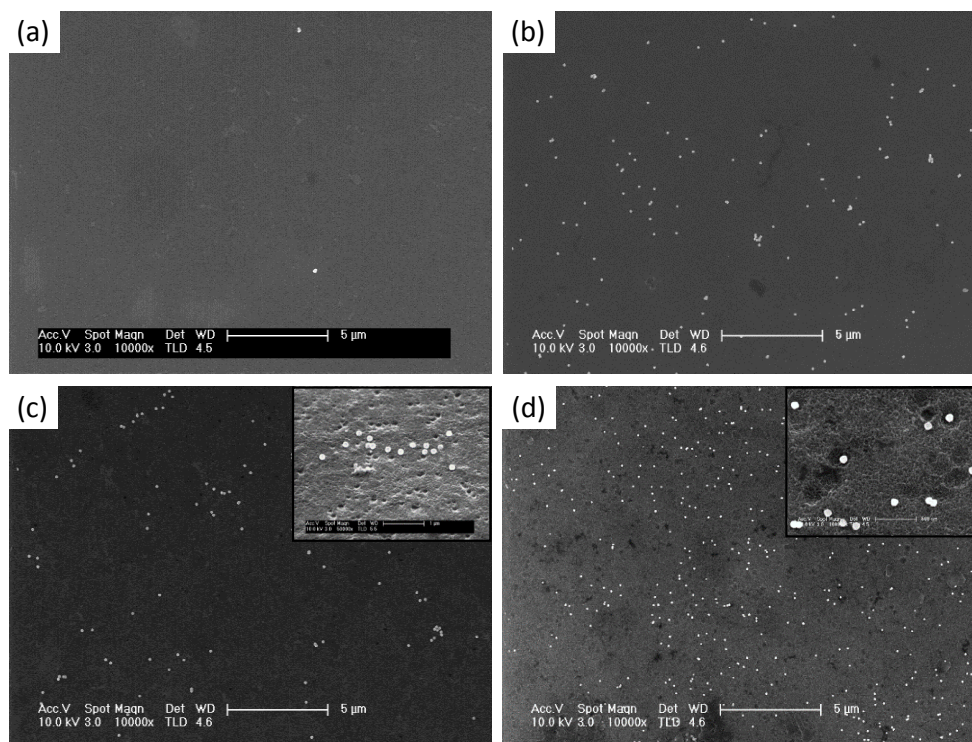
Figure 5.5 SEM images of the surface of a Si cantilever after the bioassay (a) for the control experiment and (b) for a concentration of PSA of 1 µg/mL; and of the surface of a (c) PSi1-Si cantilever and (d) PSi2-Si cantilever for a concentration of PSA of 1 µg/mL, with insets of higher magnification in order to identify the individual GNPs.

Figure 5.6 shows the quantification of the GNPs density per 100 µm² on the surface of the cantilevers using both dark-field and electron microscopy. While the GNPs density on both Si and PSi1-Si cantilevers is similar, that on the PSi2-Si cantilevers is more than three times higher. The results from dark-field and electron microscopy vary significantly. Indeed, GNPs

density obtained from the dark-field microscope images is smaller than that obtained from the SEM images. This is due to the fact that in the dark-field microscope the GNPs separated by a distance smaller than their diameter cannot be resolved. In the SEM images however, we can perfectly identify the dimers and other growing GNP aggregates.
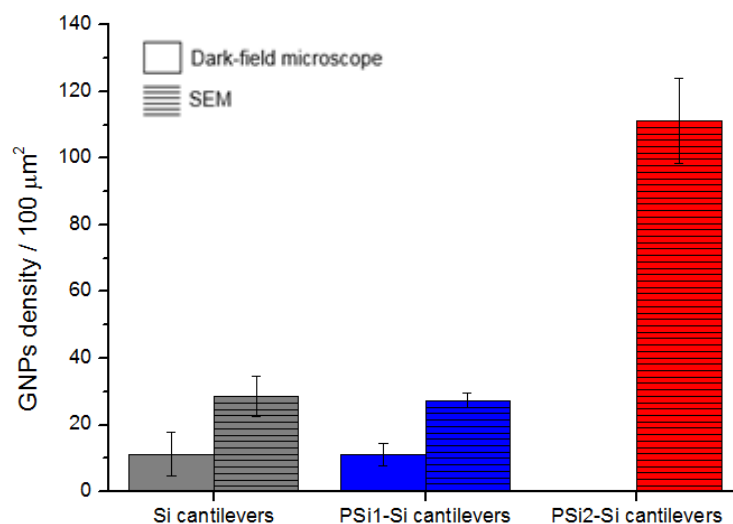
Figure 5.6 Density of GNPs on the surface of the cantilevers of Si and PSi-Si chips for a concentration of PSA of 1 µg/mL, calculated from dark-field and electron microscopy analysis.

On the other hand, we measured the resonance frequency of the fundamental vibration mode in air before and after the cantilevers exposure to the GNPs. **Figure 5.7** shows the change of the resonance frequency peak of the cantilever induced by the nanoparticle-recognition step for the PSA-detection experiment. After the negative control experiment, a shift of the resonance peak to lower frequencies (negative shift) is obtained for the three types of cantilevers and corresponds to a slight increase of the overall mass of the cantilevers due to the presence of the capture antibodies and polyethylene glycol on the silanized Si or PSi surface. This reduction of the resonance frequency increases with increased porous surface, and consequently with increased specific surface area. After the PSA-binding protocol, in the case of the Si cantilevers, we observe a bigger negative shift due to the mass loading of the GNPs. Indeed, the

nanoparticles carry a significant mass ($\sim$10 fg for each GNP) as a result of their size and density (19.300 kg.m^{-3}). In contrast, for the PSi2-Si cantilevers, there is almost no difference between the two assays (PSA-detection and control). The efficiency of the bioassay has been however demonstrated previously by SEM. That demonstrates that effects derived from the porous layer on the resonance frequency shift dominate over mass contributions due to the GNPs, and a considerable part of the expected sensitivity of the detection of PSA is consequently lost. For the PSi1-Si cantilevers, we observed a positive shift after the PSA binding. That cannot be consistent with a loss of mass since the GNPs add mass. However, the added mass of these latter can contribute to a change in the mechanical characteristics of the cantilevers [131] and in particular make the effect of the residual stress more significant. Indeed, the smaller thickness of the cantilevers combined with the high surface-to-volume ratio obtained after the formation of the porous layer on the cantilevers allows a higher modification of their surface stress with the GNPs binding [130]. The surface stress, in turn, affects directly the stiffness of the cantilevers [130]. We are consequently modifying the sensitivity of the sensor not owing to the increase of GNPs density but because of the change of its mechanical properties [132]. The observed uncertainty in the obtained results is a consequence of the heterogeneous effects of adsorbed species on the mass and stiffness sensitivity of microcantilever sensors. In fact, adsorbed mass sensing is magnified at the edge of the cantilever, while modification of the stiffness is more efficient closer to the clamp. This suggests that the observed beneficial effects of PSi formation should be restricted in future experiment to the cantilever edges, thus magnifying mass effects, and not significantly altering the stiffness.
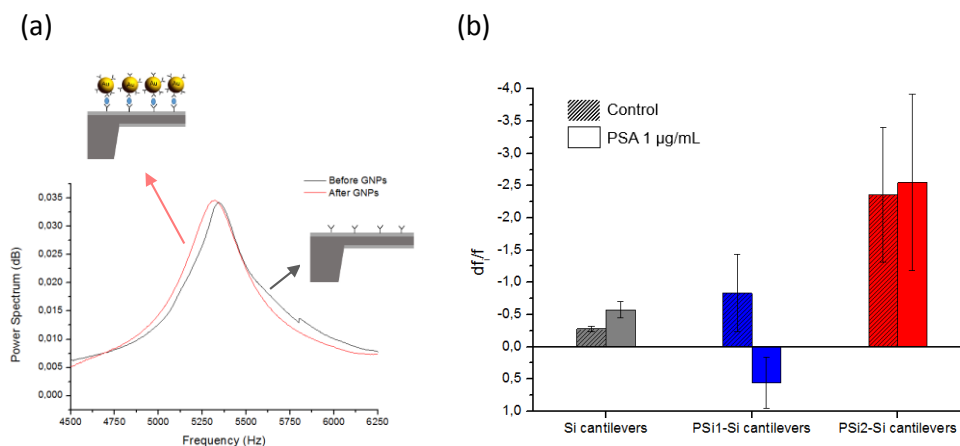
Figure 5.7 (a) Resonance frequency of the first mode of vibration of a Si cantilever before and after the PSA-recognition step. (b) Average shift of the resonance frequency of the first mode of vibration for the three types of cantilevers after the control in FBS and the PSA-detection experiments.

5.2 PSi-BASED IMPEDIMETRIC DEVICES

5.2.1 EXPERIMENTAL DETAILS

The whole process of preparation of the NiCr/PSi impedimetric interface and the protocols for its use as a GNP enhanced biosensor are illustrated in **Figure 5.8**.

Preparation of PSi samples

Spongy-type PSi was fabricated by electrochemical etching of the silicon wafer in an aqueous electrolyte composed of a mixture of HF and EtOH (volume ratio 1:1). The current density was fixed at $80 mA/cm^2$, and the anodization time at 20 s. The samples were then rinsed with ethanol and dried with N_2. After anodization, samples were submitted to chemical oxidation in solution of H_2O_2/EtOH (volume ratio 1:1) for 30 min, as a way of stabilizing the surface and reducing possible reactions with the ambient.

Formation of electrical contacts

In order to allow the impedance measurements, interdigitated Ni/Cr electrical contacts were created on the PSi layer. The first step involved the formation of slots by ion etching following a specific pattern by means of a Si mask (**Figure 5.8**). For that, we performed a 0.5 keV Ar ion bombardment by means of a Kaufman ion source operated at 10^{-3} mbar. A total charge of 0.6 C was applied to obtain slots of about 250 nm deep. A Ni/Cr (40/60 wt %) alloy was then sputtered by Ar^+ ions in a low-pressure supported discharge through the immobilized mask used for the created slots. Once the PSi sample was introduced in the vacuum chamber, argon was introduced to the chamber until a sputtering pressure of 1×10^{-2} mbar was reached. A current of 1 A and a voltage of 0.5 kV were then applied to strike a sputtering plasma and the shutter opened once a pre-sputter sequence of 5 min was finished. The deposition time was 5 min. Once the process was finished, the Si mask was removed giving rise to the resulting NiCr/PSi structure.

Formation of a biorecognition interface

We performed a sandwich assay for the detection of PSA as described in section 5.1.1. The immunoreaction between PSA and the capture antibodies is performed in this case by immersion of PSi-based devices in FBS 1x doped with PSA at concentrations ranging from 0.1 to 0.5 μg/mL.

Impedance measurements

Impedance measurements were performed with a SP-150 instruments (Bio-Logic Science Instruments) and measured between two points of the NiCr pattern that we contact by wire bonding. A voltage amplitude of 500 mV and a frequency range of 500 mHz-200 kHz at a base potential of 0 mV was applied. All measurements were carried out at room temperature.
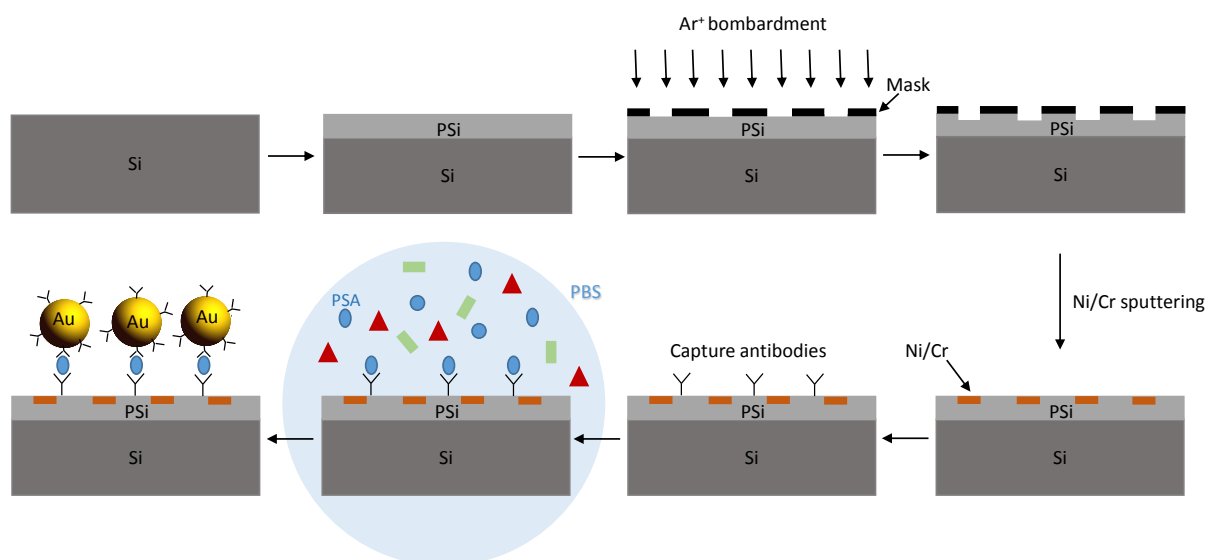
Figure 5.8 Schematic of the fabrication of the PSi-based biosensor and illustration of the detection bioassay.

5.2.2   RESULTS

Device characterization

The images shown in **Figure 5.9** highlight the structure of the different parts of the NiCr/PSi impedimetric device. Since PSi is in general a poor electrical transducer of very low conductivity, we formed interdigitated NiCr electrical contacts on its surface. The general surface view of the device is shown in **Figure 5.9** (a), where the interference colored PSi layer appears partially covered by the metallic interdigitated NiCr electrode. The good interfacial adherence at the NiCr/PSi and PSi/Si interfaces is outlined in the SEM image of **Figure 5.9** (b). The NiCr layer has a thickness of 270 nm and does not penetrate the pores. Columns of NiCr grow on a well-defined surface induced by the ion bombardment, giving rise to standard column width of 40 nm. We obtained a sponge-like PSi layer with interconnected pores (**Figure 5.9** (c)) that can be seen clearly in the higher magnification SEM image (inset). The homogeneity of the NiCr contact on the PSi surface is outlined in the SEM image of **Figure 5.9** (d). The internal structure of PSi and NiCr surfaces are magnified in the corresponding SEM images.

On the one hand, one can observe the crater like structure of the PSi surface (**Figure 5.9** (e)) with mean surface pore radius of 30 nm. On the other hand, the surface of the NiCr contact is granular with grain size in good agreement with the columnar width observed in the cross section images (**Figure 5.9** (f)).
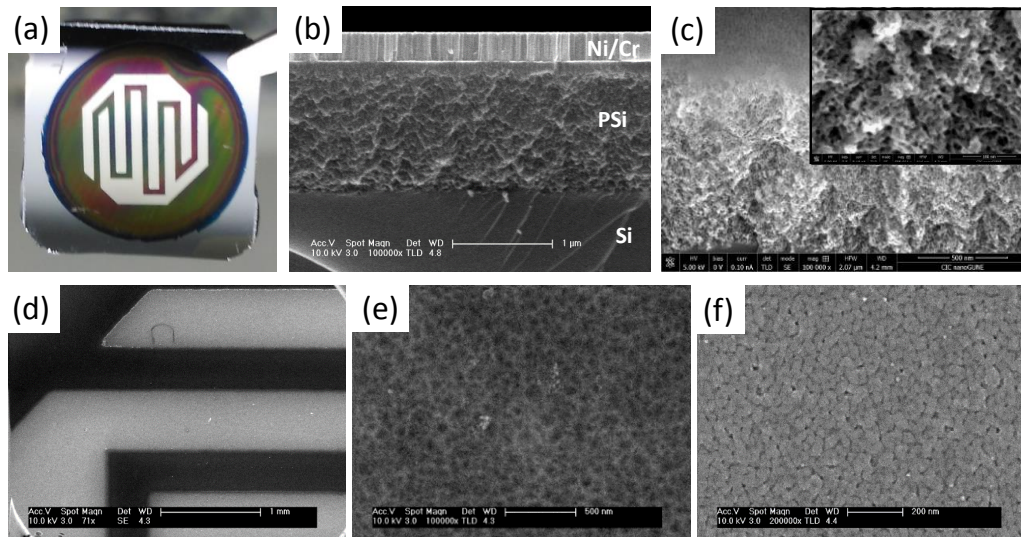
Figure 5.9 (a) General image of the NiCr/PSi impedimetric structure (PSi area has 1 cm diameter). (b) SEM cross-section image of the NiCr/PSi/Si stack, (c) Magnified SEM image of the PSi interface with inset to illustrate the spongy form PSi. (d) Surface view SEM image of the NiCr electrode on the PSi surface and corresponding SEM magnifications of the surface morphology (e) on the PSi layer, and (f) on the Ni/Cr layer.

We measured the impedance at the interface of the PSi-based device in air. For that, we applied an alternating signal of 500 mV of amplitude to the NiCr pattern, performed a frequency sweep in the range of 500 mHz-200 kHz and obtained the corresponding Nyquist diagram (**Figure 5.10**).
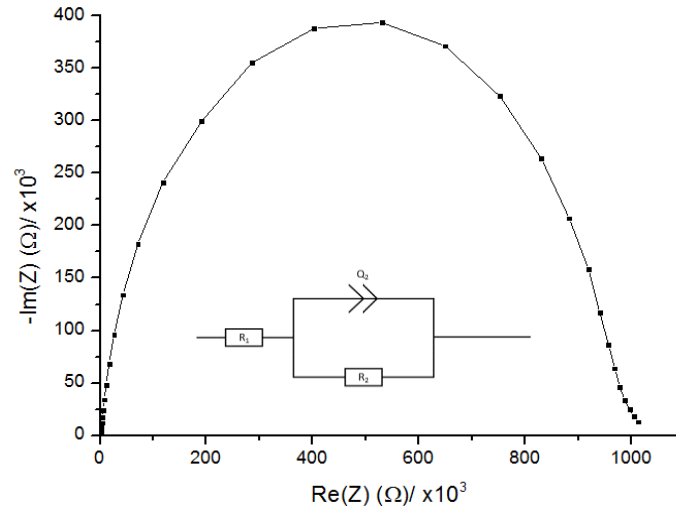
Figure 5.10 Nyquist representation of the frequency sweep (500 mHz-200 kHz) analysis

performed onto the NiCr/PSi device and its corresponding equivalent circuit (inset).

An equivalent circuit based on a combination of two resistors (R_1 and R_2) and a constant phase

element (CPE) (Q_2) (**Figure 5.10** inset) was used to fit the experimental data with the theoretical

model. The CPE is an equivalent circuit component that models the behaviour of a

double/multiple layer behaving as an imperfect capacitor. Physically, it represents a

heterogeneous capacitance very often due to the surface roughness of the sample, which can be

explained in our system in view of the porosity of PSi, and even the granular nature of the NiCr

device. Indeed, the difference between a capacitor C and a CPE Q is that the expression of the

impedance of a CPE contains an additional parameter α:

$$Z_Q(f) = \frac{1}{Q(j2\pi f)^\alpha} \qquad \textbf{Eq. 5.1}$$

where α is comprised between 0 and 1, and $Z_Q(f) = Z_C(f)$ for $\alpha = 1$, that is, an ideally planar

capacitor.

With this selection, the final equivalent circuit for the NiCr/PSi device was observed to behave

as:

$$Z(f) = R_1 + \frac{R_2}{R_2 Q_2 (j2\pi f)^{\alpha_2} + 1} \qquad \textbf{Eq. 5.2}$$

Sandwich bioassay for the detection of PSA

Changes in the interfacial impedance upon binding of PSA-GNPs conjugates in the

concentration range 0.1 µg/ml–0.5 µg/ml in FBS were then measured. **Figure 5.11** (a) shows

the Nyquist representation obtained for binding experiments performed with different

concentrations of PSA.
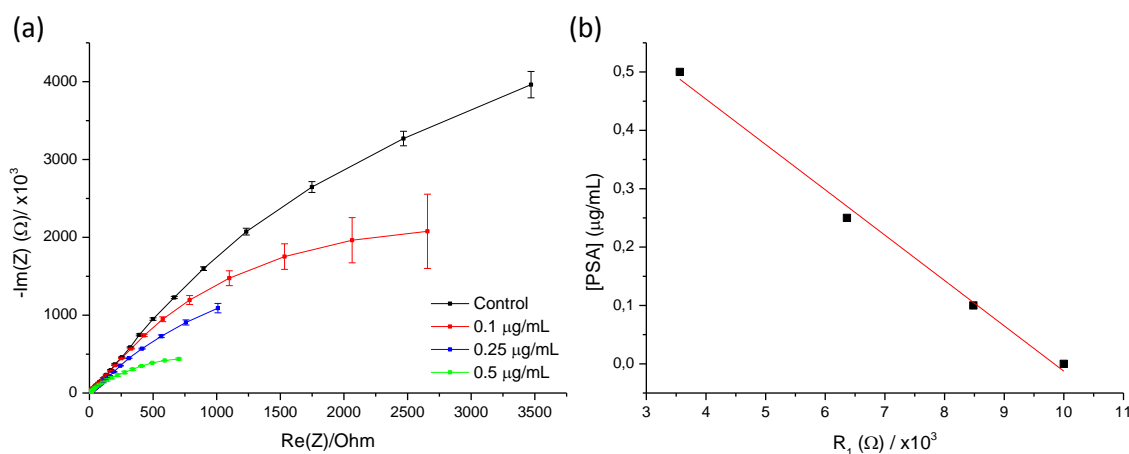
Figure 5.11 (a) Nyquist representation of the frequency sweep analysis performed on the

NiCr/PSi device after binding at concentrations of PSA and sandwiching with 100 nm GNPs.

(b) Concentration of PSA as a function of the equivalent series resistance R_1.

We observe that the immobilization of the protein biomarker resulted in decreased

impedance. The curves can be fitted with the theoretical model used in **Eq. 5.2** and the values

of the fitting parameters are resumed in **Table 5.1**.

Table 5.1 Parameters obtained after fitting of the experimental bioassay frequency sweep curves to the equivalent circuit of equation 2 and maximum value of the impedance (Z (500 mHz)).

	[PSA] (µg/mL)			
	0	**0.1**	**0.25**	**0.5**
R1 (Ω)	10000	8484	6364	3562
Q2 (F.s(α2-1)	2.23E-07	2.78E-07	7.99E-07	9.82E-07
α2	0.737	0.753	0.667	0.600
R2 (Ω)	1.63E+07	6.42E+06	5.88E+06	1.75E+06
Zmax (Ω)	5267.69	3372.41	1486.51	826.74

We can observe that the values of the R_1 resistors decrease with the concentration of PSA, while those of the CPE increase. The value of the surface impedance at a frequency of 500 mHz (maximum impedance) for each concentration shows a nonlinear decay with increasing diminution rate of the impedance for increasing concentrations. Meanwhile, the dependence of the concentration of PSA with respect to R_1 shows a linear decay dependence in the range 0-0.5 µg/mL (**Figure 5.11** (b)). A linear fit to the plot allows obtaining the following calibration line for the concentration of PSA by using the NiCr/PSi impedimetric device:

$$[PSA]= 0.76429 - 7.769.10^{-5} R_1 \text{ (µg/ml)}$$

To analyze the mechanism of transduction in more detail, it is worth underlining that the decrease in the value of the equivalent resistors with PSA concentration, implies that the surface is becoming more conductive. This can be intuitively attributed to the increased surface density of GNPs bound to the PSA molecules.

To confirm this issue, we analyzed the surfaces of the impedimetric devices after performing the sandwich assay by dark-field and electron microscopy. Gold nanoparticles gave rise to clear light scattering contrast on the surface of the PSi (**Figure 5.12**). We observe an increase of the GNPs surface density with the concentration of PSA.
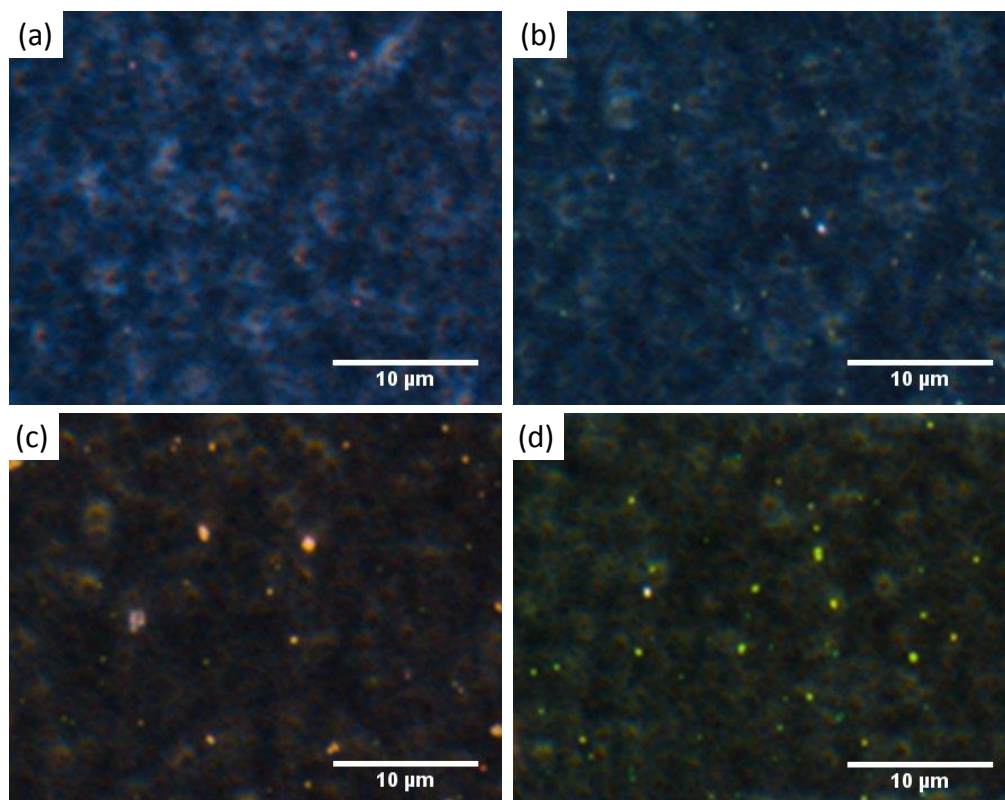
Figure 5.12 Dark field microscope images of the PSi surface after the sandwich assay: (a) control in FBS, and for a concentration of PSA of (b) 0.1 µg/mL, (c) 0.25 µg/mL and (d) 0.5 µg/mL.

To unequivocally identify the GNPs and differentiate from scattering on Si due to the PSi nanotopography, the surface was further analyzed by SEM (**Figure 5.13**).
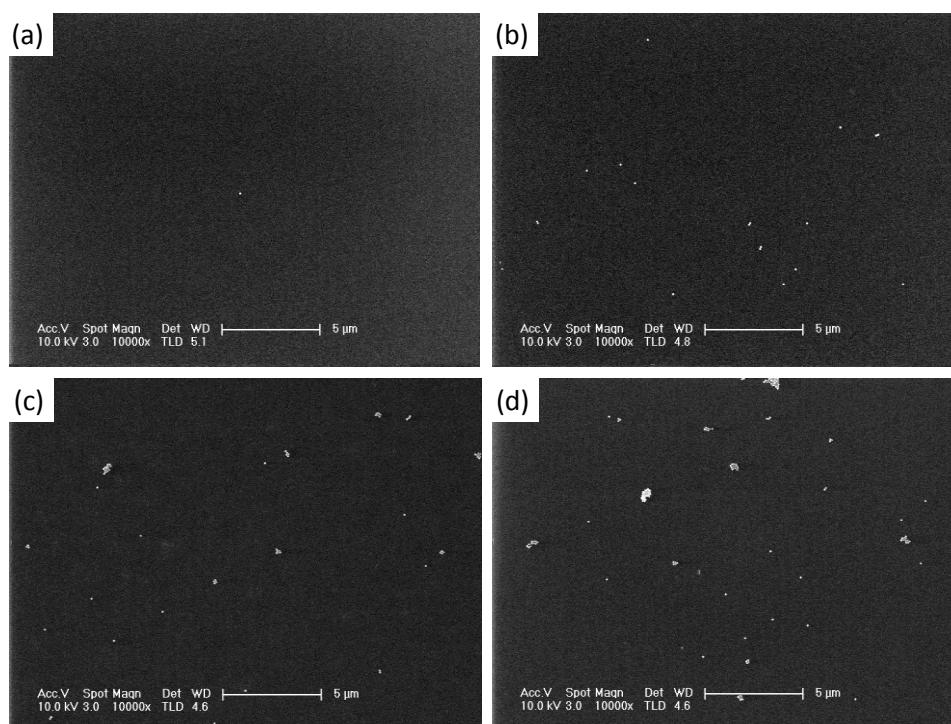
Figure 5.13 SEM images of the PSi surface after the sandwich assay: (a) control in FBS, and

for a concentration of PSA of (b) 0.1 μg/mL, (c) 0.25 μg/mL and (d) 0.5 μg/mL.

The microscopic analysis therefore confirms that the detection is accompanied by the

immobilization of GNPs, and consequently of PSA, on the PSi surface.

The counting of the GNPs on the PSi surface from the dark-field and scanning electron

microscope images for the different concentrations of PSA gave rise to the graph of **Figure 5.14**.
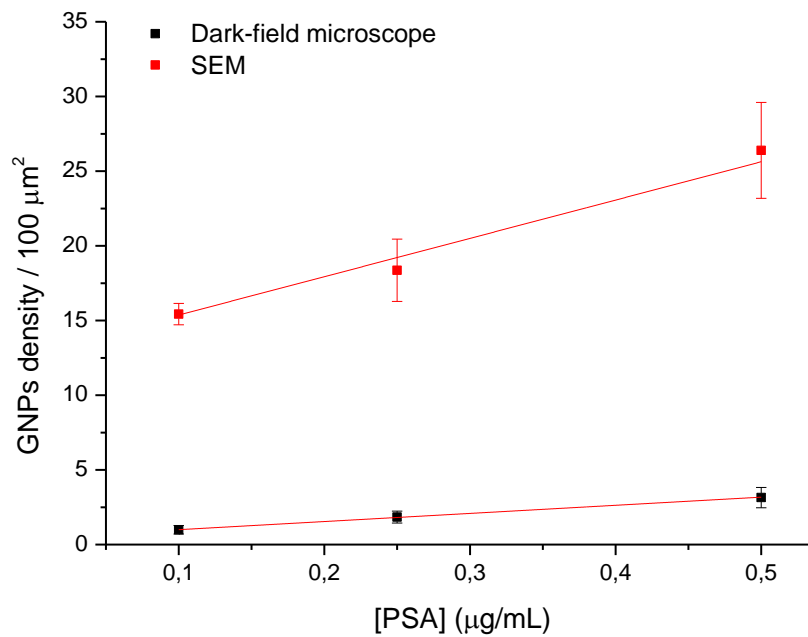
Figure 5.14 GNPs density on the PSi surface as a function of the PSA concentration in FBS as extracted from correlated estimations by dark-field and scanning electron microscopy.

As in the case of the PSi-Si nanomechanical sensors, GNPs density obtained from the dark-field microscope images is smaller than that obtained from the SEM images in which we can clearly identify the dimers and the GNPs aggregates. However, in this case, the difference is much higher than in the case studied in section 5.1.2 because we have a significant increase of GNPs aggregates, as observed in the SEM images in **Figure 5.13**.

The density of GNPs shows a linear dependence on the PSA concentration in the range used in this experiment. This result suggests in fact that there is an indirect relationship between the density of GNPs on the surface and the equivalent resistance R1 of the NiCr/PSi device upon binding with different concentrations of PSA. Additionally, this inverse relationship is clue in the habilitation of an internal control of the device making use of the dual optoplasmonic-electric transduction of the 100 nm GNPs. These results invite to further research on the use of GNP supported PSi impedimetric biosensor.

CHAPTER 6

CONCLUSIONS

6.1 ACHIEVEMENTS

6.1.1   FUNCTIONALIZED PSi

• A visible light activated process has been proposed for the synthesis of organosilane functionalized PSi using molecules containing different functional groups (perfluorodecyl, glycydoxypropyl and aminopropyl) at low concentrations of 0.2%.

• The efficiency of the visible light activated functionalization has been demonstrated using complementary analytical techniques. On one hand, ssNMR spectroscopy proved to be a powerful technique to obtain surface spectroscopic features regarding the organosilane assemblies and not only confirmed, but considerably complemented the observations made by the FTIR spectroscopy study.

• ^{13}C ssNMR provides more detailed information to characterize the interface species than FTIR, differentiating aliphatic chain carbons, within the same chain (i.e. as in perfluorodecyl group) and in comparison to the other silanes (i.e. the perfluorodecyl with respect to the aminopropyl). This is especially relevant since there is no surface spectroscopic technique with the chemical sensitivity to reveal these features.

• The combined use of ^{29}Si and ^{19}F ssNMR has revealed extremely useful in the determination of silane binding efficiency and its influence on the stability of PSi face to moisture. In this sense, even if PFDS shows the lowest degree of condensation with PSi

(dominant T1 in ^{29}Si spectra), it is also suggested that it provides the highest hydroxylation protection (reduced formation of Q^n structures).

- XPS provided a quantification study of the composition of the functionalized surfaces confirming the successful attachment of the organosilanes on the PSi surface. The concomitant relative increase of the C-O and Si-O components for increasing light activation time demonstrates that the surface oxidation feeds the condensation of the organosilanes, making viable a reaction normally requiring a previous thermal or chemical oxidation.

- The photoactivation of PSi and subsequent generation of hole/electron pairs allow promoting the nucleophilic attack of trace water and further reaction with the silane on the resulting oxidized surface.

- The process led to homogeneous surfaces with no traces of oligomerized silane structures, which suggests that organosilane coverage is below one monolayer and makes the process useful as model for the analysis of organosilane-PSi interfaces. Through the attachment of a set of organosilanes on PSi, it was possible to generate hybrid microstructures with a potential control of the hydrophilic/hydrophobic properties of the surface, as demonstrated by the WCA measurements.

6.1.2   WETTING OF FUNCTIONALIZED PSi

- The modification of the PSi surfaces by peroxidation and self-assembly of organosilanes allowed controlling their wetting. Using wetSTEM, we were able to observe, on a single pore basis, the differentiated water filling of the pores as a function of the RH for the PSi samples with different pore functionalization.

- The wetting dynamics of the different PSi-organosilane systems were obtained through analysis of the normalized STEM gray value. A statistical analysis allowed establishing adsorption differences depending on the pore size and surface chemistry. In particular, in

agreement with the Kelvin equation, the condensation of smaller pores is induced at smaller RH. Additionally, the capability of water adsorption is larger in the case of the hydrophilic samples than in the hydrophobic samples.

- The gravimetric measurement of the sorption isotherms gave us global water adsorption/desorption isotherms. This allowed us obtaining more precise information about the wetting of the PSi samples and the mechanism of water adsorption and desorption.

- We found that the amount of adsorbed water is larger in the case of the peroxidized and APTS-functionalized PSi than in that of the as-formed and PFDS-functionalized PSi, hence confirming the data obtained by the wetSTEM analysis. This difference in the hydrophobic/hydrophilic properties of the PSi surfaces also plays an important role on the width of the hysteresis loop. This latter is enlarged in the hydrophobic samples, following the model set by the Kelvin equation.

6.1.3   APPLICATIONS

PSi-based nanomechanical biosensors

- Composite PSi-Si microcantilever arrays were fabricated and characterized. Vapor phase stain etching demonstrated to be an efficient and reproducible way to form PSi on crystalline Si cantilevers. By varying the volume ratio of the $HF:HNO_3$ mixture, we were able to obtain two PSi layers with different thickness and pore size. In particular, these parameters increased with increased proportion of HF.

- PSA was immobilized at a concentration of 1 μg/ml on the surface of both Si and PSi-Si cantilevers and the sensitivity was analyzed in a sandwich bioassay enhanced by 100 nm GNPs. Although the GNPs density was found to be much higher on the PSi2-Si cantilevers surface by SEM analysis, owing to the large increase of specific surface area, the very high

porosity prevented their optoplasmonic detection and their differentiated nanomechanical response against non-activated cantilevers.

- In the case of the PSi1-Si cantilevers, both optoplasmonic and nanomechanical detection of GNPs were possible. In this case, the sensitivity was increased, not owing to the increase of GNPs density, but because of the change of the residual stress induced by their binding.

PSi-based impedimetric biosensors

- An impedimetric device based on PSi with a NiCr interdigitated electrode was fabricated and characterized. PSA was immobilized at different concentrations on its surface and the sensitivity analyzed in a sandwich bioassay enhanced by 100 nm GNPs. The increasing immobilization of the protein biomarker resulted in a decreasing impedance within the 0.1 to 0.5 μg/ml.

- The series resistance obtained from the equivalent circuit showed a linear dependence with the concentration of PSA and allowed obtaining a calibration line for the biosensor. PSi has a high initial impedance, which allows obtaining large impedance contrasts after the analyte binding and further exposure to the GNPs. Indeed, the GNPs allow increasing the sensitivity of the detection due to their contribution to the device conductivity.

- A dark field microscopic analysis outlined the possibility of performing a dual detection since the immobilization of 100 nm GNPs introduces visible hot-spots. Consequently, the concentration of PSA bound on the PSi surface could be correlated with the density of immobilized GNPs.

6.2 GENERAL CONCLUSIONS

- The controlled surface reactivity of PSi opens new opportunities to tune the material for specific applications.

- Surface modification with light activated organosilane assemblies bearing selected terminal groups allows engineering surfaces with different hydrophobic/hydrophilic properties.

- Perfluorinated hydrophobic organosilanes are effective in the protection of PSi based devices providing stability against high humidity condensation environments.

- Hydrophilic organosilane modifications allow a molecular selectivity and control of the biomolecular interactions, as demonstrated for epoxy groups by developing two different dual sensing platforms based on PSi and GNPs.

- PSi-Si cantilevers can provide, to some extent, both plasmonic and nanomechanical transduction for the sandwich bioassay labelled with GNPs for PSA detection. Indeed, the thickness-porosity of the PSi on Si cantilevers must be limited to avoid interferences between the mass and stiffness bending pathways whose predictability is compromised.

- The combination of porous microcantilevers with GNPs constitutes a real novelty in the field of biosensing, and allows increasing the sensitivity of the detection, though the homogeneous formation of the porous layer on the whole cantilever surface is not the most advisable approach.

- PSi-based impedimetric devices proved to be a possible candidate for the development of dual electric-optoplasmonic biosensors for PSA detection, with the added value of presence of an internal transduction control. Indeed, the developed platform exhibited a linear behavior in the concentration range of 0.1 µg/mL- 0.5 µg/mL.

- The GNPs-based assay exploits not only their surface plasmon absorption but also their ability to contribute to the impedimetric device conductivity.

- The use of both PSi and GNPs as dual transducing elements in a single platform (on Si planar substrates or Si microcantilevers) allows determining the presence of PSA with high statistical significance and consequently contributes to the selectivity of the device.

6.3 FUTURE PERSPECTIVES

• Since PSi, and in particular PSips, can potentially be used to allocate nanomaterials and biomolecules to provide additional functionalities, this study opens a path to the characterization of those materials hosted in the PSi matrix, which is especially attractive for biomolecular sensing applications and drug delivery. This is an attractive idea, whether for the purpose of identifying chemical and structural features, or for indirect evaluation of their stability (i.e. face to critical agents such as moisture).

• Regarding the PSi-based biosensing platforms, the several issues being faced at the first stage of the PSi-Si cantilevers investigations invite us to move forward to the development of alternative systems with increasingly controlled surface distribution. We envisage the formation of PSi only at the edge of the cantilever. That would be a way to increase the surface area at a critical spot for mass sensitivity, but not drastically altering the natural stiffness of the original cantilever, leading to more predictable sensing response.

• In view of the promising results obtained with the PSi-based impedimetric sensor, further attempts will be made to improve its limits of detection. Moreover, the same principle shall be applied for the detection of other biomarkers of interest.

• Finally, in this thesis, we developed an electron microscopy protocol to study the RH effects on functionalized PSi substrates. The next step would be to apply this know-how to the PSi-based biosensing platforms, in order to evaluate their stability and lifetim

ANNEX I

CONCLUSIONES

6.4 REALIZACIONES

6.4.1 FUNCIONALIZACION DE SILICIO POROSO

- Se ha propuesto un proceso activado por luz visible para la síntesis de Silicio Poroso (PSi) funcionalizado con organosilanos usando moléculas conteniendo diferentes grupos funcionales (perfluoro, glicidoxi y amino) a muy bajas concentraciones de 0,2 %.

- La eficiencia de la funcionalización activada por luz visible se ha demostrado usando técnicas analíticas complementarias. Por un lado, la espectroscopía de resonancia magnética nuclear en estado sólido (ssNMR) ha demostrado ser una potente técnica para la obtención de características espectroscópicas de superficie acerca de los ensamblados de organosilano y no solo confirma, sino que también complementa las observaciones hechas mediante espectrocopía infrarroja por transformada de Fourier (FTIR).

- El análisis del isótopo ^{13}C en ssNMR proporciona más información detallada para caracterizar las especies en la interfase que FTIR, diferenciando los carbonos de cadenas alifáticas, dentro de la misma cadena (como en el grupo perfluorodecil) y comparado con otros silanos (el perfluorodecil con respecto con el aminopropil). Esto es especialmente relevante puesto que no existe ninguna técnica espectroscópica de superficie con sensibilidad química que permita revelar estas características.

- El uso combinado de ^{29}Si y ^{19}F ssNMR ha revelado la eficaz adhesión del perfluorodecilsilano (PFDS) y su influencia en la estabilidad del PSi frente a la humedad. En ese sentido, aunque el PFDS muestra el menor grado de condensación con PSi (T1 dominente en los espectros de ^{29}Si), también sugiere que proporciona la mayor protección contra la hidroxilación (formación reducida de estructuras Q^n).

- La espectroscopía de fotoelectrones (XPS) proporciona un estudio cuantitativo de la composición de las superficies funcionalizadas confirmando la adhesión de los organosilanos en la superficie del PSi. El aumento relativo de los componentes C-O y Si-O con el tiempo de activación por luz demuestra que la oxidación superficial habilita la condensación de los organosilanos, haciendo posible una reacción que normalmente requiere oxidación termal o química previa.

- La fotoactivación del PSi y la consecuente generación de pares electrón/hueco permite promover el ataque nucleofílico del agua presente en el solvente y la reacción con el silano en la resultante superficie oxidada de PSi.

- El proceso da lugar a superficies homogéneas sin rastros de estructuras de silano oligomerizado, lo que sugiere que el recubrimiento de organosilano esté por debajo de una monocapa y hace el proceso útil como modelo para el análisis de interfases organosilano-PSi. A través del ensamblado de una gama de organosilanos sobre PSi, ha sido posible generar microestructuras híbridas con un control en las propiedades hidrofílicas/hidrofóbicas de la superficie, como demostrado por las medidas de ángulo de contacto.

6.4.2 MOJABILIDAD DEL PSi FUNCIONALIZADO

- La modificación de las superficies de PSi por peroxidación y autoasemblado de organosilanos ha permitido controlar su mojabilidad. Usando microscopía electrónica de barrido-transmisión ambiental (wetSTEM), hemos sido capaces de observar, en la base de poro

individual, el llenado diferencial de los poros con agua en función de la humedad relativa (RH) para las muestras de PSi con diferente funcionalización de poro.

• La dinámica de mojabilidad de los diferentes sistemas PSi-organosilano se ha obtenido a través del análisis de la normalización de los valores de la escala de grises en las imágenes de wetSTEM. Un análisis estadístico ha permitido establecer las diferencias de adsorción en función del tamaño de poro y de la química superficial. En particular, de acuerdo con la ecuación de Kelvin, cuantos más pequeños son los poros, menor es la RH necesaria para inducir condensación de agua en su interior. Además, la capacidad de adsorción de agua es mayor en el caso de las muestras hidrofílicas que en el de las muestras hidrofóbicas.

• La medida gravimétrica de las isotermas de adsorción/desorción han ha permitido visualizar el comportamiento global del agua en los poros dando lugar a información complementaria sobre la mojabilidad de las muestras de PSi y sobre el mecanismo de adsorción y desorción de agua.

• La cantidad de agua adsorbida es mayor en el caso del PSi peroxidado y funcionalizado con aminopropilsilano (APTS) que en el caso del PSi recién fabricado y funcionalizado con PFDS, lo que confirma los datos obtenidos en el análisis por wetSTEM. Esta diferencia en las propiedades hidrofóbicas/hidrofílicas de las superficies de PSi juega también un papel importante en la anchura de la curva de histéresis. Esta última se agranda en las muestras hidrofóbicas, siguiendo el modelo establecido por la ecuación de Kelvin.

6.4.3 APPLICACIONES

Sensores nanomecánicos basados en PSi

• Se han fabricado y caracterizado micropalancas compuestas de PSi y Si. El ataque en fase vapor ha demostrado ser una manera eficiente y reproducible de formar PSi en palancas de Si. Cambiando las proporciones de ácido en la mezcla HF:HNO₃, hemos sido capaces de

obtener capas de PSi con diferentes espesores y tamaños de poro. En particular, estos parámetros aumentan con la proporción de HF.

• El antígeno específico de próstata (PSA) ha sido inmovilizado a una concentración de 1 μg/ml en la superficie de las palancas de Si así como en las de PSi-Si y la sensibilidad se ha analizado en un ensayo biológico en sándwich realzado con nanopartículas de oro (GNPs) de 100 nm de diámetro. Aunque la densidad de las GNPs es mucho más alta en la superficie de las palancas de PSi más porosas, gracias al incremento del área de superficie específica, la muy alta porosidad impide su detección optoplasmónica y su respuesta nanomecánica relativa a las palancas no biológicamente activadas.

• En el caso de las palancas de PSi menos porosas, ha sido posible la detección tanto optoplasmónica como nanomecánica de GNPs. En este caso, se ha observado un aumento de la sensibilidad, pero no gracias al aumento de la densidad de GNPs inmobilizadas, sino debido al cambio de estrés residual inducido por su adhesión.

Biosensores impedimétricos basados en PSi

• Se ha fabricado y caracterizado un dispositivo impedimétrico basado en PSi con un electrodo de NiCr interdigital. Se ha inmovilizado PSA a diferentes concentraciones en su superficie y la sensibilidad se ha sido analizado en un ensayo biológico en sándwich realzado con GNPs de 100 nm de diámetro. La adhesión creciente del biomarcador en el rango 0.1 hasta 0.5 μg/ml ha dado lugar a una disminución de la impedancia.

• La resistencia en serie obtenida a partir del circuito equivalente muestra una dependencia lineal con la concentración de PSA y ha permitido obtener una línea de calibración para el biosensor. El PSi tiene una alta impedancia inicial, lo que permite obtener grandes contrastes de impedancia después de la adhesión del analito y de la exposición a las GNPs. En

efecto, las GNPs permiten incrementar la sensibilidad de la detección gracias a su contribución a la conductividad del dispositivo.

• Un análisis basado en el microscopio de campo oscuro ha destacado la posibilidad depermite realizar una doble detección puesto que la inmovilización de GNPs de 100 nm de diámetro introduce puntos dispersivos visibles. Por lo tanto, la concentración de PSA ligada en la superficie de PSi está relacionada con la densidad de GNPs inmovilizadas.

6.5 CONCLUSIONES GENERALES

• La reactividad superficial controlada del PSi abre nuevas oportunidades para adaptar el material para aplicaciones específicas.

• La modificación superficial activada por luz con organosilanos conteniendo grupos terminales determinados permite manejar superficies con diferentes propiedades hidrofóbicas/hidrofílicas.

• Los organosilanos hidrofóbicos perfluorados son efectivos en la protección de dispositivos basados en PSi, proporcionando estabilidad contra entornos de alta humedad.

• Las modificaciones con organosilanos hidrofílicos permiten una selectividad molecular y un control de las interacciones biomoleculares, como se ha demostrado para los grupos epóxidos, desarrollando dos diferentes plataformas sensoras de doble detección basadas en PSi y GNPs.

• Las palancas de PSi-Si pueden proporcionar, hasta cierto punto, una transducción tanto plasmónica como nanomecánica en el ensayo biológico realizado con las GNPs para la detección de PSA. En efecto, el espesor y la porosidad del PSi en las palancas de Si inducen interferencias entre la deflexión causada por la masa y la causada por la rigidez, comprometiendo una predicción a priori de la respuesta del sensor.

- La combinación de las palancas porosas con las GNPs constituye una novedad en el campo del biosensado, y permite aumentar la sensibilidad de la detección, aunque la formación homogénea de la capa porosa en la superficie entera de la palanca no sea el enfoque más conveniente.

- Los dispositivos impedimétricos basados en PSi son posibles candidatos para el desarrollo de biosensores de detección eléctrica y optoplasmónica para la detección de PSA, con el valor añadido de la presencia de un control interno de transducción. En efecto, la plataforma desarrollada ha mostrado un comportamiento lineal en el rango de concentraciones de 0.1 µg/mL a 0.5 µg/mL.

- El ensayo basado en las GNPs explota no solo su plasmón de superficie sino también su capacidad para contribuir a la conductividad del dispositivo impedimétrico.

- El uso del PSi y de las GNPs como elementos de doble transducción en una sola plataforma (en sustratos de Si planos o en palancas de Si) permite determinar la presencia de PSA con significante estadística y en consecuencia contribuye a la selectividad del dispositivo.

REFERENCES

[1] S. Dhanekar, S. Jain, Porous silicon biosensors: current status, Biosensors and Bioelectronics. 41 (2013) 54-64.

[2] J. Ali, J. Najeeb, M.A. Ali, M.F. Aslam, A. Raza, Biosensors: their fundamentals, designs, types and most recent impactful applications: a review, Journal of Biosensors & Bioelectronics. 8 (2017) 1-9.

[3] B. Bohunicky, S.A. Mousa, Biosensors: the new wave in cancer diagnosis, Nanotechnology, Science and Applications. 4 (2011) 1-10.

[4] V.S.P.K. Sankara Aditya Jayanthi, A. Bikas Das, U. Saxena, Recent advances in biosensor development for the detection of cancer biomarkers, Biosensors and Bioelectronics. 91 (2017) 15-23.

[5] N. Lynn Henry, D.F. Hayes, Cancer biomarkers, Molecular Oncology. 6 (2012) 140-146.

[6] M.A. Najeeb, S. Jasmine, M. Chavali, Recent advancements in nano-based biosensor for early detection of prostate cancer, International Journal of recent trends in electrical & electronics engineering. 3 (2014) 112-120.

[7] M.A. Najeeb, S. Pillai, M. Chavali, Nano-based PSA biosensors: an early detection technique of prostate cancer, Journal of Biomimetics, Biomaterials and Biomedical Engineering. 20 (2014) 87-98.

[8] N. Triroj, P. Jaroenapibal, H. Shi, J.I. Yeh, R. Beresford, Microfluidic chip-based nanoelectrode array as miniaturized biochemical sensing platform for prostate-specific antigen detection, Biosensors and Bioelectronics. 26 (2011) 2927-2933.

[9] D.A. Healy, C.J. Hayes, P. Leonard, L. McKenna, R. O'Kennedy, Biosensor developments: application to prostate-specific antigen detection, Trends in Biotechnology. 25 (2007) 125-131.

[10] Y. Ding, H. Lu, G. Shi, J. Liu, G. Shen, R. Yu, Cell-based immobilization strategy for sensitive piezoelectric immunoassay of total prostate specific antigen, Biosensors and Bioelectronics. 24 (2008) 228-232.

[11] R. Gupta, S. Swaminathan, Modeling and simulation of piezoelectric based micro cantilever systems for prostate specific antigen, International Symposium on Next-Generation Electronics (ISNE). (2015).

[12] M. Holzinger, A. Le Goff, S. Cosnier, Nanomaterials for biosensing applications: a review, Frontiers in Chemistry. 2 (2014) 1-10.

[13] J. Lei, H. Ju, Signal amplification using nanomaterials for biosensing, Chemical sensors and biosensors. 14 (2013) 17-42.[14] H. Hutter, D. Maysinger, Gold-nanoparticle-based biosensors for detection of enzyme activity, Trends in Pharmacological Sciences. 34 (2013) 497-507.

[15] M. Mathelié-Guinlet, I. Gammoudi, L. Beven, F. Moroté, M. Delville, C. Grauby-Heywang, T. Cohen-Bouhacina, Silica nanoparticles assisted electrochemical biosensor for the detection and degradation of *Escherichia Coli* bacteria, Procedia Engineering. 168 (2016) 1048-1051.

[16] L.T.N. Truong, T.T. Nguyen, A.L.T. Luu, Y. Ukita, Y. Takamura, Sensitive labelles impedance immunosensor using gold nanoparticles-modified of scree-printed carbon ink electrode for ACT-prostate specific antigen detection, 16th International Conference on Miniaturized Systems for Chemistry and Life Sciences. (2012) 1912-1914.

[17] J. Zhu, J. Li, A. Wang, Y. Chen, J. Zhao, Fluorescence quenching of alpha-fetoprotein by gold nanoparticles: effect of dielectric shell on non-radioactive decay, Nanoscale Research Letters. 5 (2010) 1496-1501.

[18] R.A. Reynolds, C.A. Mirkin, R.L. Letsinger, Homogeneous nanoparticle-based quantitative colorimetric detection of oligonucleotides, Journal of American Chemical Society. 122 (2000) 3795-3796.

[19] W. Xu, X. Xue, T. Li, H. Zeng, X. Liu, Ultrasensitive and selective colorimetric DNA detection by nicking endonuclease assited nanoparticle amplification, Angewandte Chemie International Edition. 48 (2009) 6849-6852.

[20] N. Li, X. Su, Y. Lu, Nanomaterial-based biosensors using dual transducing elements for solution phase detection, Analyst. 140 (2015) 2916-2943.

[21] P.M. Kosaka, V. Pini, J.J. Ruz, R.A. da Silva, M.U. González, D. Ramos, M. Calleja, J. Tamayo, Detection of cancer biomarkers in serum using a hybrid mechanical and optoplasmonic nanosensor, Nature Nanotechnology. 9 (2014) 1047.

[22] S. Kachel, S. DuVall, W. Schabel, Effect of absorbed water on active biosensor layers, 16th International Coating Science and Technology Symposium. (2012).

[23] F. Puppo, A. Dave, M. Doucey, D. Sacchetto, C. Baj-Rossi, Y. Leblebici, G. De Micheli, S. Carrara, Memristive biosensors under varying humidity conditions, IEEE Transactions on Nanobioscience. 13 (2014) 19.

[24] A. Uhlir, Electrolytic shaping of germanium and silicon, Bells Labs Technical Journal. 35 (1956) 333-347.

[25] L.T. Canham, Silicon quantum wire array fabrication by electrochemical and chemical dissolution of wafers, Applied Physics Letters. 57 (1990) 1046.

[26] M.J. Sailor, Porous Silicon in Practice: Preparation, Characterization and Applications, Wiley-VCH Verlag GmbH & Co. ed., Wiley, 2012.

[27] R.K. Soni, G.R. Bassam, S.C. Abbi, Laser-controlled photoluminescence characteristics of silicon nanocrystallites produced by laser-induced etching, Applied Surface Science. 214 (2003) 151-160.

[28] M. Saadoun, N. Mliki, H. Kaabi, K. Daoudi, B. Bessais, H. Ezzaouia, R. Bennaceur, Vapour-etching-based porous silicon: a new approach, Thin Solid Films. 405 (2002) 29-34.

[29] S. Stolyarova, S. Weiss, M. Levy, Y. Nemirovsky, New type of dual macro and nano fractal structure of reaction induced vapor phase stain etched porous silicon, Physica Status Solidi C - Current Topics in Solid State Physics, Vol 4 No 6. 4 (2007) 2054-2058.

[30] H. Föll, M. Christophersen, J. Carstensen, G. Hasse, Formation and application of porous silicon, Materials Science and Engineering R. 280 (2002) 1-49.

[31] H. Kao, C. Liao, T. Hung, Y. Pan, A.S.T. Chiang, Direct synthesis and solid-state NMR characterization of cubic mesoporous silica SBA-1 functionalized with phenyl groups, Chem. Mater. 20 (2008) 2412-2422.

[32] L.A. DeLouise, B.L. Miller, Quantatitive assessment of enzyme immobilization capacity in porous silicon, Analytical Chemistry. 76 (2004) 6915-6920.

[33] M. Calleja, P.M. Kosaka, A. San Paulo, J. Tamayo, Challenges for nanomechanical sensors in biological detection, Nanoscale. 4 (2012) 4925-4938.

[34] J. Tamayo, P.M. Kosaka, J.J. Ruz, A. San Paulo, M. Calleja, Biosensors based on nanomechanical systems, Chemical Society Reviews. 42 (2013) 1287-1311.

[35] S. Stolyarova, S. Cherian, R. Raiteri, J. Zeravik, P. Skladal, Y. Nemirovsky, Composite porous silicon-crystalline silicon cantilevers for enhanced biosensing, Sensors and Actuators B-Chemical. 131 (2008) 509-515.

[36] H. Gharaei, A. Nikfarjam, J. Mohamadnejad, F. Saniei, Simulation of a nobel porous Si based cantilever beam CA 15-3 protein sensor, First RSI/ISM International Conference on Robotics and Mechatronics. (2013) 82.

[37] S. Meltzman, A. Shemesh, S. Stolyarova, Y. Nemirovsky, Y. Eichen, Microcantilevers as Gas-Phase Sensing Platforms: Simplification and Optimization of the Production of Polymer Coated Porous-Silicon-Over-Silicon Microcantilevers, Journal of Polymer Science Part B-Polymer Physics. 52 (2014) 141-146.

[38] S. Stolyarova, A. Shemesh, O. Aharon, O. Cohen, L. Gal, Y. Eichen, Y. Nemirovsky, Vertically integrated MEMS SOI composite porous silicon-crystalline silicon cantilever-array sensors: concept for continuous sensing of explosives and warfare agents, Advanced Materials and Technologies for Micro/Nano-Devices, Sensors and Actuators. (2010) 261-274.

[39] R. Radhakrishnan, I.I. Suni, C.S. Bever, B.D. Hammock, Impedance biosensors: applications to sustainability and remaining technical challenges, ACS Sustainable Chemistry & Engineering. 2 (2014) 1649-1655.

[40] J.S. Daniels, N. Pourmand, Label-free impedance biosensors: opportunites and challenges, Electroanalysis. 19 (2007) 1239-1257.

[41] K. Kant, C. Priest, J.G. Shapter, D. Losic, The influence of nanopore dimensions on the electrochemical properties of nanopore arrays studied by impedance spectroscopy, Sensors. 14 (2014) 21316-21328.

[42] R. Ohno, H. Ohnuki, H. Wang, T. Yokoyama, H. Endo, D. Tsuya, M. Izumi, Electrochemical impedance spectroscopy biosensor with interdigitated electrode for detection of human immunoglobulin A, Biosensors and Bioelectronics. 40 (2013) 422-426.

[43] L. Yang, Y. Li, C.L. Griffis, M.G. Johnson, Interdigitated microelectrode (IME) impedance sensor for the detection of viable *salmonella typhimurium*, Biosensors and Bioelectronics. 19 (2004) 1139-1147.

[44] R. Wang, J. Lum, Z. Callaway, J. Lin, W. Bottje, Y. Li, A label-free impedance immunosensor using scree-printed interdigitated electrodes and magnetic nanobeads for the detection of *E. Coli* O157:H7, Biosensors. 5 (2015) 791-803.

[45] N. Naveas, J. Hernandez-Montelongo, R. Pulido, V. Torres-Costa, R. Villanueva-Guerrero, J.P. García Ruiz, M. Manso-Silván, Fabrication and characterization of a chemically oxidized-nanostructured porous silicon based biosensor implementing orienting protein A, Colloids and Surfaces B: Biointerfaces. 115 (2014) 310-316.

[46] G. Recio-Sánchez, V. Torres-Costa, M. Manso, D. Gallach, J. López-Garcia, R.J. Martín-Palma, Toward the development of electrical biosensors based on nanostructured porous silicon, Materials. 3 (2010) 755-763.

[47] A. Verdaguer, G.M. Sacha, H. Bluhm, M. Salmeron, Molecular structure of water at interfaces: wetting at the nanometer scale, Chemical Reviews. 106 (2006) 1478.

[48] J.J. Mares, J. Kristofik, E. Hulicius, Influence of Humidity on Transport in Porous Silicon, Thin Solid Films. 255 (1995) 272-275.

[49] A. Kovacs, D. Meister, U. Mescheder, Investigation of humidity adsorption in porous silicon layers, Physical Status Solidi A. 206 (2009) 1343-1347.

[50] Z.M. Rittersma, A. Splinter, A. Bödecker, W. Benecke, A novel surface-micromachined capacitive porous silicon humidity sensor, Sensors and Actuators B. 68 (2000) 210-217.

[51] E. Xifré Pérez, L.F. Marsal, J. Ferré-Borrull, T. Trifonov, J. Pallarès, Infuence of the humidity conditions on the reflectivity spectrum of a porous silicon microcavity, Physica E. 38 (2007) 172-175.

[52] J. Oswald, J.J. Mares, J. Kristofik, R. Sedlacik, Dependence of PS photoluminescence on relative humidity, Thin Solid Films. 276 (1996) 268-271.

[53] N.P. Mandal, S. Dey, S.C. Agarwal, Influence of surface treatments on nanocrystalline silicon, Thin Solid Films. 451 (2004) 375-378.

[54] H.A. Santos, Porous Silicon for Biomedical Applications, First Ed. ed., Elsevier, 2014.

[55] D. Gallach, G. Recio Sánchez, A. Muñoz Noval, M. Manso Silván, G. Ceccone, R.J. Martín Palma, V. Torres Costa, J.M. Martínez Duart, Functionality of porous silicon particles: surface modification for biomedical applications, Materials Science and Engineering B. 169 (2010) 123-127.

[56] B. Xia, S. Xiao, D. Guo, J. Wang, J. Chao, H. Liu, J. Pei, Y. Chen, Y. Tang, J. Liu, Biofunctionalisation of porous silicon (PS) surface by using homobifunctional cross-linkers, Journal of Materials Chemistry. 16 (2006) 570-578.

[57] F. Tighilt, S. Belhousse, S. Sam, K. Hamdani, K. Lasmi, J.N. Chazalviel, N. Gabouze, Grafting of functionalized polymer on porous silicon surface using Grignard reagent, Applied Surface Science. 421 (2017) 82-88.

[58] P. Dwivedi, S. Das, S. Dhanekar, Polymer functionalized nanostructured porous silicon for selective water vapor sensing at room temperature, Superlattices and Microstructures. 104 (2017) 547-552.

[59] J. Dong, A. Wang, K.Y. Simon Ng, G. Mao, Self-assembly of octadecyltrichlorosilane monolayers on silicon-based substrates by chemical vapor deposition, Thin Solid Films. 515 (2006) 2116-2122.

[60] B. Bhushan, Self-assembled monolayers for controllling hydrophobicity and/or friction and wear, Modern Tribology Handbook. (2000) 885-928.

[61] Z. Xu, K. Song, S. Yuan, C. Liu, Microscopic wetting of self-assembled monolayers with different surfaces: a combined molecular dynamics and quantum mechanics study, Langmuir. 27 (2011) 8611-8620.

[62] M. Szöri, D.J. Tobias, M. Roeselová, Microscopic wetting of mixed self-assembled monolayers: a molecular dynamics study, The Journal of Physical Chemistry B. 113 (2009) 4161.

[63] E. Li, Z. Du, S. Yuan, Properties of a water layer on hydrophilic and hydrophobic SAMs surfaces: a molecular dynamic study, Science China Chemistry. 56 (2013) 773.

[64] O. Bisi, S. Ossicini, L. Pavesi, Porous silicon: a quantum sponge structure for silicon based optoelectronics, Surface Science Reports. 38 (2000) 1-126.

[65] V. Lehmann, U. Gosele, Porous silicon formation - A quantum wire effect, Applied Physics Letters. 58 (1991) 856-858.

[66] P.C. Searson, J.M. Macaulay, The fabrication of porous silicon structures, Nanotechnology. 3 (1992) 188.

[67] Q.Y. Sun, L. de Smet, B. van Lagen, M. Giesbers, P.C. Thüne, J. van Engelenburg, F. de Wolf, H. Zuilhof, E. Sudhölter, Covalently attached monolayers on crystalline hydrogen-terminated silicon: extremely mild attachment by visible light, Journal of American Chemical Society. 127 (2005) 2514-2523.

[68] H. Sano, H. Maeda, S. Matsuoka, K.H. Lee, K. Murase, H. Sugimura, Self-assembled monolayers directly attached to silicon substrates formed from 1- hexadecene by thermal, ultraviolet, and visible light activation methods, Japanese Journal of Applied Physics. 47 (2008) 5659-5664.

[69] N. Naveas, V. Torres Costa, D. Gallach, J. Hernandez-Montelongo, R.J. Martín Palma, J.P. Garcia-Ruiz, M. Manso-Silván, Chemical stabilzation of porous silicon for enhanced biofunctionalization with immunoglobulin, Sci. Technol. Adv. Mater. 13 (2012) 045009.

[70] K. Fukami, H. Tanaka, M.L. Chourou, T. Sakka, Y.H. Ogata, Filling of mesoporous silicon with copper by electrodeposition from an aqueous solution, Electrochimica Acta. 54 (2009) 2197-2202.

[71] C. Tedjo, Controlling protein-surface interactions in chromatography using mixed self-assembled monolayers, (2011).

[72] J. Kim, Probing organic self-assembled monolayers (SAMs) on silicon by FTIR with single reflectance ATR, PIKE technologies.

[73] C. Mateo, R. Torres, G. Fernández-Lorente, C. Ortiz, M. Fuentes, A. Hidalgo, F. López-Gallego, O. Abian, J.M. Palomo, L. Betancor, B.C.C. Pessela, J.M. Guisan, R. Fernández-Lafuente, Epoxy-amino groups: a new tool for improved immobilization of proteins by the epoxy method, Biomacromolecules. 4 (2003) 772-777.

[74] N.J. Shirtcliffe, P. Roach, Superhydrophobicity for antifouling microfluidic surfaces, Methods Mol. Biol. 949 (2013) 269-281.

[75] G.H. Michler, Electron Microscopy of Polymers, Springer-Verlag Berlin Heidelberg, 2008.

[76] M. Manso Silván, M. Langlet, J.M. Martínez Duart, P. Herrero, Preparation of interfaces for TEM cross-section observation, Nuclear Instruments and Methods in Physics, B. 257 (2007) 623-626.

[77] W. Zhou, Z.L. Wang, Scanning Microscopy for Nanotechnology, Springer, 2007.

[78] A.M. Donald, The use of environmental scanning electron microscopy for imaging wet and insulating materials, Nature Materials. 2 (2003) 511-516.

[79] D.J. Stokes, Investigating Biological Ultrastructure using Environmental Scanning Electron Microscopy (ESEM), Microscopy and Analysis. (2012).

[80] S. J. Pennycook, A. R. Lupini, M. Varela, A. Y. Borisevich, Y. Peng, M. P. Oxley, K. van Benthem, M. F. Chisholm, Scanning Transmission Electron Microscopy for Nanostructure Characterization, (2007) 152-191.

[81] A. Bogner, P.H. Jouneau, G. Thollet, D. Basset, C. Gauthier, A history of scanning electron microscopy developments: Towards "wet-STEM" imaging, Micron. 38 (2007) 390-401.

[82] A. Bogner, G. Thollet, D. Basset, P.H. Jouneau, C. Gauthier, WetSTEM: A new development in environmental SEM for imaging nano-objects included in a liquid phase, Ultramicroscopy. 104 (2005) 290-301.

[83] M.S. Joens, C. Huynh, J.M. Kasuboski, D. Ferranti, Y.J. Sigal, F. Zeitvogel, M. Obst, C.J. Burkhardt, K.P. Curran, S.H. Chalasani, L.A. Stern, B. Boetze, J.A.J. Fitzpatrick, Helium ion microscopy (HIM) for the imaging of biological samples at subnanometer resolution, Scientific Reports. 3 (2013).

References

[84] Y. Yuan, T.R. Lee, Surface Science Techniques, Springer, 2013.

[85] T. Young, III. An assay on the cohesion of fluids, Philosophical Transactions of the Royal Society. 95 (1805) 65-87.

[86] R.N. Wenzel, Resistance of solid surfaces to wetting by water, Industrial & Engineering Chemistry. 28 (1936) 988-994.

[87] A.B.D. Cassie, S. Baxter, Wettability of porous surfaces, Transactions of the Faraday Society. 40 (1944) 546.

[88] S. Hofmann, Auger- and X-Ray Photoelectron Spectroscopy in Materials Science, Springer, 2012.

[89] D.R. Vij, Handbook of Applied Solid-State Spectroscopy, Springer Science & Business Media, 2007.

[90] B. Stuart, Infrared Spectroscopy: Fundamentals and Applications, Wiley, 2004.

[91] R.H. Kraus, M. Espy, P. Magnelind, P. Volegov, Ultra-Low Field Nuclear Magnetic Resonance: A New MRI Regime, Oxford University Press, 2014.

[92] M. Rangus, NMR spectroscopy in solids: A comparison to NMR spectroscopy in liquids, in: F. Conti, W.E. Blumberg, J. de Gier and F. Pocchiari (Eds.), Physical Methods on Biological Membranes and their Model Systems, Springer, 2007.

[93] M. Hu, C. Novo, A. Funston, H. Wang, H. Staleva, S. Zou, P. Mulvaney, Y. Xia, G.V. Hartland, Dark-field microscopy studies of single metal nanoparticles: understanding the factors that influence the linewidth of the localized surface plasmon resonance, Journal of Materials Chemistry. 17 (2008) 1949-1960.

[94] N. Wei, J. You, K. Friehs, E. Flaschel, T. Wilhelm Nattkemper, In situ dark field microscopy for on-line monitoring of yeast cultures, Biotechnology Letters. 29 (2007) 373-378.

[95] R.A. Caylor, Towards the characterization of silicon surface: solid state nuclear magnetic resonance studies, Ph. D. thesis (Colorado State University). (2011).

[96] W.K. Chang, M.Y. Liao, K.K. Gleason, Characterization of porous silicon by solid-state nuclear magnetic resonance, J. Phys, Chem. 100 (1996) 19653-19658.

[97] S. Tosatti, R. Michel, M. Textor, N.D. Spencer, Self-assembled monolayers of dodecyl and hydroxy-dodecyl phosphateson both smooth and rough titanium and titanium oxide surfaces, Langmuir. 18 (2002) 3537-3548.

[98] A. Muñoz-Noval, M. Hernando Pérez, V. Torres Costa, R.J. Martín Palma, P.J. de Pablo, M. Manso Silván, High surface water interaction in superhydrophobic nanostructured silicon surfaces: convergence between nanoscopic and microscopic scale phenomena, Langmuir. 28 (2012) 1909-1913.

[99] X. Zeng, G. Xu, Y. Gao, Y. An, Surface wettability of (3-Aminopropyl)triethoxysilane self-assembled monolayers, The Journal of Physical Chemistry B. 115 (2011) 450.

[100] D. Moreno Cerrada, C. Rodriguez, F. Moreno Madrid, P.J. de Pablo Gómez, M. Manso Silvan, Characterization of silanized surfaces and P22 virus adsorption, Submitted.

[101] T. Yen, C. Soong, Hybrid Cassie-Wenzel model for droplets on surfaces with nanoscale roughness, Physical Review E. 93 (2016) 022805.

[102] T. Tsuboi, T. Sakka, Y.H. Ogata, Structural study of porous silicon and its oxidized states by solid-state high-resolution ^{29}Si NMR spectroscopy, Physical Review B. 58 (1998) 13863-13869.

[103] C.K. Huang, P.F. Kerr, Infrared study of the carbonate minerals, The American Mineralogist. 45 (1960) 311-324.

[104] P. Innocenzi, G. Brusatin, M. Guglielmi, R. and Bertani, New synthetic route to (3-glycidoxypropyl)trimethoxysilane-based hybrid organic-inorganic materials, Chem. Mater. 11 (1999) 1672-1679.

[105] B. Simoncic, B. Tomsic, B. Orel, I. Jerman, Sol-gel technology for chemical modification of textiles, in: D. Jocic (Ed.), Surface Modification Systems for Creating Stimuli Responsiveness of Textiles, Enschede, 2010, pp. 17-34.

[106] R.A. Faulkner, J.A. DiVerdi, Y. Yang, T. Kobayashi, G.E. Maciel, The surface of nanoparticle silicon as studied by solid-state NMR, Materials. 6 (2013) 18-46.

[107] A.M. Shanmugharaj, K.Y. Rhee, S.H. Ryu, Influence of dispersing medium on grafting of aminopropyltriethoxysilane in swelling clay materials, Journal of Colloidal and Interface Science. 298 (2006) 854-859.

[108] T. Pietrab, A. Bifone, V.-. Koch, A.P. Alivisatos, A. Pines, ^{29}Si high resolution solid-state nuclear magnetic resonance spectroscopy of porous silicon, Journal of non-crystalline solids. 202 (1996) 68-76.

[109] S.G. Vasil'ev, V.I. Volkov, E.A. Tatarinova, A.M. Muzafarov, A Solid-State NMR investigation of MQ silicone copolymers, Appl. Magn. Reson. 44 (2013) 1015-1025.

[110] R.S. Ribeiro, R.A.S. San Gil, E.L.S. Lima, Application of ^{13}C and ^{29}Si MAS NMR to the surface characterization of a barbituric derivative anchored on silica, Ann. Magn. Reson. 3 (2004) 116-118.

[111] S. Radi, N. Basbas, S. Tighadouini, M. Bacquet, S. Degoutin, F. Cazier, New Amine-Modified Silicas: Synthesis, Characterization and Its Use in the Cu(II)-Removal from Aqueous Solutions, Progress in Nanotechnology and Nanomaterials. 2 (2013) 108-116.

[112] H. Lu, Synthesis and characterization of amino-functionalized silica nanoparticles, Colloid Journal. 75 (2013) 311-318.

[113] S. Ando, R.K. Harris, U. Scheler, Fluorine-19 NMR of Solids Containing Both Fluorine and Hydrogen, Encyclopedia of Nuclear Magnetic Resonance. 9 (2002) 531-550.

[114] S. Dauphas, S. Ababou-Girard, A. Girard, F. Le Bihan, T. Mohammed-Brahim, V. Vié, A. Corlu, C. Guguen-Guillouzo, O. Lavastre, F. Geneste, Stepwise functionalization of SiNx surfaces for covalent immobilization of antibodies, Thin Solid Films. 517 (2009) 6016-6022.

[115] C. Funk, P.M. Dietrich, T. Gross, H. Min, W. Unger, W. Weigel, Epoxy-functionalized surfaces for microarray applications: surface chemical analysis and fluorescence labeling of surface species, Surface and interface analysis. 44 (2012) 890-894.

[116] C. Nietzold, P.M. Dietrich, S. Ivanov-Pankov, A. Lippitz, T. Gross, W. Weigel, W. Unger, Functional group quantification on epoxy surfaces by chemical derivatization (CD)-XPS, Surface and Interface analysis. 46 (2014) 668-672.

[117] E. Frydman, H. Cohen, R. Maoz, J. Sagiv, Monolayer damage in XPS measurements as evaluated by independant methods, Langmuir. 13 (1997) 5089-5106.

[118] Y.H. Ogata, K. Kobayashi, M. Motoyama, Electrochemical metal deposition on silicon, Current Opinion in Solid State & Materials Science. 10 (2006) 163-172.

[119] A. Wong, U.J. Krull, Surface characterization of 3-glycidyloxypropyltrimethoxysilane films on silicon-based substrates, Analytical and Bioanalytical Chemistry. 383 (2005) 187-200.

References

[120] A. Munoz-Noval, M. Hernando Perez, V. Torres Costa, R.J. Martin Palma, P.J. de Pablo, M. Manso Silvan, High Surface Water Interaction in Superhydrophobic Nanostructured Silicon Surfaces: Convergence between Nanoscopic and Macroscopic Scale Phenomena, Langmuir. 28 (2012) 1909-1913.

[121] R.W. Cohn, Freestanding metallic and polymeric nanostructures: direct self-assembly, in: S.E. Lyshevski (Ed.), Dekker Encyclopedia of Nanoscience and Nanotechnology, Third ed., Taylor & Francis, 2014.

[122] M. Thommes, Physical adsorption characterization of nanoporous materials, Chemie Ingenieur Technik. 82 (2010) 1059.

[123] E. de la Llave, V. Molinero, D.A. Scherlis, Role of confinement and surface affinity on filling mechanisms and sorption hysteresis of water in nanopores, The Journal of Physical Chemistry. 116 (2012) 1833.

[124] Z.A. ALOthman, A review: fundamental aspects of silicate mesoporous materials, Materials. 5 (2012) 2874.

[125] M. Thommes, B. Smarsly, M. Groenewolt, P.I. Ravikovitch, A.V. Neimark, Adsorption hysteresis of nitrogen and argon in pore networks and characterization of novel micro- and mesoporous silicas, Langmuir. 22 (2006) 756.

[126] Z. Pavlik, J. Zumar, I. Medved, R. Cerny, Water vapor adsorption in porous building materials: experimental measurement and theoretical analysis, Transport in Porous Media. 91 (2012) 939.

[127] M. Factorovich, E. Gonzalez Solveyra, V. Molinero, D.A. Scherlis, Sorption isotherms of water in nanopores: relationship between hydrophobicity, adsorption pressure, and hysteresis, The Journal of Physical Chemistry. 118 (2014) 16290.

[128] P.A. Monson, Contact angles, pore condensation, and hysteresis: insights from a simple molecular model, Langmuir. 24 (2008) 12295.

[129] H. Duan, Y. Xue, X. Yi, Vibration of cantilevers with rough surfaces, Acta Mechanica Solida Sinica. 22 (2009) 550-554.

[130] R.B. Karabalin, L.G. Villanueva, M.H. Matheny, J.E. Sader, M.L. Roukes, Stress-induced variations in the stiffness of micro- and nanocantilever beams, Physical Review Letters. 108 (2012) 236101.

[131] D. Saya, L. Nicu, M. Guirardel, Y. Tauran, C. Bergaud, Mechanical effect of gold nanoparticles labeling used for biochemical sensing applications: a multimode analysis by means of SiNx micromechanical cantilever and bridge mass detectors, Review of Scientific Instruments. 75 (2004) 3010.

[132] M.X. Shi, B. Liu, Z.Q. Zhang, Z.W. Zhang, H.J. Gao, Direct influence of residual stress on the bending stiffness of cantilever beams, Proceedings of the Royal Society A. 468 (2012) 2595-2613.